Focused ultrasound-guided delivery of microRNA-126 to endothelial cells in *in vitro* and *ex vivo* models

Stephanie He

A Thesis

In the Department of

Biology

Presented in Partial Fulfillment of the Requirements

For the Degree of

Doctor of Philosophy (Biology)

At Concordia University

Montreal, Quebec, Canada

November 2024

CONCORDIA UNIVERSITY

SCHOOLOF GRADUATE STUDIES

This is to certify that the thesis

By: Stephanie He
Entitled: Focused ultrasound-guided delivery of microRNA-126 to endothelial cells in *in vitro* and *ex vivo* models

and submitted in partial fulfillment of the requirements for the degree of

DOCTOR OF PHILOSOPHY (Biology)

complies with the regulations of the University and meets the accepted standards with respect to originality and quality.

Signed by the final examining committee:

_____ Chair
Dr. Saurabh Maiti

_____ External Examiner
Dr. François Yu

_____ Examiner
Dr. Elena Kuzmin

_____ Examiner
Dr. Jung Oh

_____ Examiner
Dr. Alisa Piekny

_____ Thesis Supervisor
Dr. Brandon Helfield

Approved by _____
Dr. Robert Weladji, Graduate Program Director

November 18th, 2024 _____
Dr. Pascale Sicotte, Dean
Faculty of Arts and Science

Abstract

Focused ultrasound-guided delivery of microRNA-126 to endothelial cells in *in vitro* and *ex vivo* models

Stephanie He, Ph.D.

Concordia University, 2024

The prevalence of cardiovascular diseases, such as ischemia, underscores the need for innovative therapeutic strategies. Recent advances in the field of focused ultrasound offer a non-surgical, targeted, and promising technology to treat various life-threatening diseases, including brain disorders, inoperable cancers and some vascular diseases. This approach harnesses the therapeutic potential of ultrasound-stimulated microbubbles for the modulation of cellular and vascular permeability to guide the delivery of therapeutics. More recently, gene therapy has shown great potential as a less invasive approach in contrast to surgical interventions. In the context of cardiovascular diseases, microRNA-126 is a key target for therapeutic interventions, as it is abundant in endothelial cells that line blood vessels, and plays a pivotal role in promoting angiogenesis. This thesis explores the use of ultrasound-stimulated microbubbles as a non-viral and targeted approach for microRNA-126 delivery to endothelial cells in both *in vitro* and *ex vivo* models. First, I designed and characterized a cationic microbubble formulation that can carry a microRNA-126 payload on its surface. I then developed an ultrasound regimen to safely deliver microRNA-126 to endothelial cell suspensions and demonstrated its effect on blood vessel formation *in vitro*. My results indicate the increase of microRNA-126 in endothelial cells result in the modulation of key downstream proteins, notably PIK3R2 and SPRED1, and improves angiogenesis. Building on these findings, I then developed a more complex vascular model to study ultrasound-guided microRNA-126 delivery by isolating rat mesenteric arteries. This model

allowed me to replicate a more physiologically relevant vascular environment *ex vivo*. By incorporating factors such as intralumenal pressure and fluid flow, this study investigated the effect of focused ultrasound on the vasoconstriction and vasodilation of an artery. My findings revealed a positive relationship between ultrasound-mediated cell permeabilization and increased flow velocity, as well as an inverse relationship between the levels of microRNA-126 delivered with increased flow velocity. These results suggest that understanding hemodynamic conditions in specific anatomic regions could enhance the effectiveness of gene delivery. Overall, this thesis highlights the potential to deliver microRNA-126 using focused ultrasound and microbubbles while minimizing cellular and vascular viability, with anticipation for its application in gene therapy for cardiovascular diseases.

Acknowledgements

First and foremost, this thesis would not have been possible without the support, generosity and patience from my supervisor, Dr. Brandon Helfield. It has been the utmost privilege to experience graduate school under your supervision, from weekly donut meetings to annual conference presentations, you have created such a pleasant lab environment that sparked my curiosity and drive towards focused ultrasound research. Thank you for the opportunity to learn from you, for believing in me since day one, and for making sure I was happy.

Thank you to my committee members, Dr. Alisa Piekny and Dr. Jung Oh for their guidance and insightful discussions during these past five years. I am also thankful for Dr. Andreas Bergdahl for taking interest in my project and providing advice on the *ex vivo* chapter. Thank you to Dr. John Capobianco for allowing me to use the Zetasizer.

I also would like to thank everyone who helped with my experiments, notably Seth Truran from Living Systems Instrumentation for setting up and troubleshooting the pressure myograph, and Nhat Pham for not only helping me with my Western Blots, but for impromptu corridor discussions throughout the years. Thank you to my co-authors Davindra Singh and Hossein Yusefi for their time and contributions towards my projects, as well as the members of the Helfield lab for the helpful discussions, especially Elahe Memari, Kyle Hazel and Zoe Katz.

Finally, I am thankful for the major scholarships that supported me throughout my PhD: Concordia University, Hydro-Québec, and the Fonds de Recherche du Québec (FRQS).

Dedication

I dedicate this thesis to my fiancé, Max. You have been the most patient and supportive person through every decision I made, and you aspired me to aim for goals beyond what I thought I could achieve. Special mention to our tiny poofs, Luna and Leo, for choosing to sleep next to me through every single late night during my university years instead of their warm beds. Thank you for making me a better person and I can't wait to finally enjoy life with you.

It has been a great pleasure to work alongside and befriend members from the Helfield lab. From showing up at the lab at the oddest times at night (Davindra "Big Vinny" Singh), to creating unforgettable memories at conference Airbnbs (Hossein Yusefi, Kyle "John Pork" Hazel and Ana Baez), I am grateful to have shared these years with you.

To the person who inspired me to fast-track to a PhD, thank you Dr. Dilan Jaunky for showing me it was possible to achieve as much as you did, both professionally and personally. Also, thank you Brandon Janky for your friendship since our undergrad days and for showing me that email from Dr. Helfield 5 years ago.

I want to thank my friends (and neighbours), Claudia and Richard, for the weekly gaming nights and gluttonous dinners that kept me grounded throughout my degree. You are like family to me, and I am so happy we met during frosh.

Finally, thank you to my parents, for the unimaginable sacrifices they had to make to give me a chance at this life. Big thanks to my bröther, Keven, for all the conversations, advice and laughs.

Contribution of Authors

Chapter 1: General introduction

Part of this chapter (1.2 and 1.3) consists of a review article written with Davindra Singh and Dr. Brandon Helfield.

Chapter 2: Stable Cavitation-Mediated Delivery of miR-126 to Endothelial Cells

Dr. Brandon Helfield supervised the project, edited the manuscript, and provided Figure 2.5. I conducted the ultrasound experiments with help from Davindra Singh and Hossein Yusefi for the sample handling part described in chapter 2.4.5. I performed all of the experiments, the formal analysis, wrote and edited the manuscript.

Chapter 3: Flow Velocity Modulates Vascular Delivery of microRNA-126 Using Focused Ultrasound and Microbubbles

Dr. Brandon Helfield supervised the project, edited the manuscript, wrote the MATLAB code for the propidium iodide-positive cell counting and vessel diameter analysis in Figures 3.2 and 3.3, as well as provided the background-subtracted micrograph in Figure 3.2 C-D. Davindra Singh helped with the animal work by managing the ordering, coordinating surgeries and provided assistance with organ isolation. I conducted all of the experiments, performed the formal analysis, wrote and edited the manuscript.

Table of Contents

List of Figures

List of Tables

List of Abbreviations and Symbols

×g	Relative centrifugal force
19G	19 gauge
3' UTR	3' untranslated regions
A1-13	Annexin protein 1-13
Ach	Acetycholine
Akt	Ak strain transforming
ALG-2	Apoptosis-linked gene-2
ALIX	ALG-2 interacting protein X
Ang-2	Angiopoitin-2
ANOVA	Analysis of variance
Arp2/3	Actin related protein 2/3 complex
ASM	Acid sphingomyelinase
Bad	Bcl-2 associated death promoter
BAPTA-AM	1,2-bis(o-aminophenoxy)ethane-N,N,N',N'-tetraacetic acid acetoxymethyl ester
BBB	Blood brain barrier
Bcl-2	B-cell lymphoma
BCRP	Breast cancer resistance protein
BIN1	Bridging integrator-1
BSA	Bovine serum albumin
C_3F_8	Octafluoropropane
C_4F_{10}	Perfluorobutane
Ca^{2+}	Calcium ions
Cav3	Caveolin-3
Cdc42	Cell division cycle 42
cDNA	Clonal DNA
CVD	Cardiovascular disease
DC	Duty cycle
DEPC	Diethylpyrocarbonate
diH2O	Deionized water
DLL4	Delta-like 4 ligand
DMSO	dimethylsulfoxide
DNA	Deoxyribonucleic Acid
DSPC	1,2-distearoyl-sn-glycero-3-phosphocholine
DSTAP	1,2-stearoyl-3-trimethylammonium-propane
EB1	Microtubule-associated protein 1
E-cadherin	Epithelial cadherin
ECL	Enhanced chemiluminescence
EDTA	Ethylenediaminetetraacetic acid

E_{ext}	External E-field
E-field	Electric field
EGF	Endothelial growth factor
EGFL7	EGF-like domain 7
EGM-2	Endothelial cell growth medium-2
EHD1/2	Eps15 (epidermal growth factor receptor pathway substrate) homology domain
eNOS	Endothelial nitric oxide synthase
ERK	Extracellular Signal-Regulated Kinase
ERK	Extracellular signal-regulated kinase
ESCRT I-III	Endosomal sorting complex required for transportation I-III
f	Focal point (transducer, chapter 2)
f#	F number; ratio of focal depth to aperture size
F-actin	Filamentous actin
FDA	Food and Drug Administration
FFT	Fast Fourier transform
FGF	Fibroblast growth factor
f_s	Factor reflecting the shape of the cell
fs	Femtoseconds
GAPDH	Glyceraldehyde-3-phosphate dehydrogenase
GSK3β	Glycogen synthase kinase 3β
GTPases	Guanosine triphosphate hydrolase
HIF-1α	Hypoxia-inducible factor-1α
HRP	Horse radish peroxidase
hsa-miR-126-3p	Human miR-126 derived from 3' arm of miRNA precursor
HUVEC	Human umbilical vein endothelial cells
Hz	Hertz
INF2	Inverted formin-2
IRE	Irreversible electroporation
kDa	Kilo Daltons
kHz	Kilo Hertz
kPa	Kilo Pascals
kVcm-1	Kilo volts per cm
L-NAME	N-nitro-L-arginine methyl ester
MEK	Mitogen-activated protein kinase kinsase
MG53	Mitsugumin 53
MHz	Mega Hertz
MI	Mechanical index
miR	MicroRNA
miR-126	MicroRNA-126

MLC	Myosin regulatory light chain
mmHg	Millimeter of mercury
MMP	Metalloproteinases
MRgFUS	Magnetic resonance-guided focused ultrasound
mRNA	Messenger RNA
mTOR	Mechanistic target of rapamycin
MTT	3-(4,5-dimethylthazolk-2-yl)-2,5-diphenyl tetrazolium bromide
n.s.	Non-significant
η_0	Cytosolic viscosity
NO	Nitric oxide
N-WASP	Neuronal Wiskott-Aldrich Syndrome protein
OCD	Obsessive-compulsive disorder
p21	Cyclin-dependent kinase inhibitor 1 or CDK-interacting protein 1
P720	Intralumenal peristaltic pump
PAGE	Polyacrylamide gel electrophoresis
PBS	Phosphate buffered saline
PCD	Passive cavitation detection
PCR	polymerase chain reaction
PDGF	Platelet-derived growth factor
PDGFR	Platelet-derived growth factor receptor
PEG40S	Polyoxyethylene (40) stearate
P-gp	P-glycoprotein
Phe	Phenylephrine
PI	Propidium iodide
PIK3R2	Phosphoinositide-3-Kinase Regulatory Subunit 2
PNP	Peak negative pressure
pre-miRNA	Precursor-microRNA
PRI	Pulse repetition interval
Pri-miRNA	Primary-microRNA
PS-200-P	Servo pump
PS-200-S	Pressure Servo Controller
PVDF	Polyvinylidene fluoride
$\tilde{Q}$	Initial cell volume
R	Effective cell radius
RAS	Rat sarcoma
Ras	Rat sarcoma virus
R_c	Radius of cell membrane
RE	Reversible electroporation
RF	Radio frequency
RhoA	Ras homolog family member A

RIPA	Radio-immunoprecipitation assay
RISC	RNA-induced silencing complex
RNA	Ribonucleic Acid
RNase	Ribonuclease
ROK	Rho-associated kinase
r_p	Pore radius
rtPA	Recombinant tissue plasminogen activator
RT-qPCR	Reverse transcriptase quantitative PCR
S100A11	S100 calcium binding protein A11
SDS-PAGE	Sodium dodecyl-sulfate PAGE
SEM	Standard error of the mean
SF_6	Sulfur hexafluoride
siRNA	Short interfering RNA
SNARE	Soluble N-ethylmaleimide sensitive factor attachment protein receptor
SNR	Signal-to-noise ratio
SPRED1	Sprouty Related EVH1 Domain Containing 1
SYT7	Synaptotagmin 7
TBE	Tris-borate EDTA
TBS	Tris buffered saline
TBST	TBS with Tween20
TGF-β	Transforming growth factor-beta
TSC2	Tuberous sclerosis complex-2
U6	Housekeeping small nuclear RNA
UTMD	Ultrasound-targeted microbubble destruction
VCAM-1	Vascular cell adhesion molecule 1
VEGF	Vascular endothelial growth factor
VEGFR-2	VEGF receptor 2
VHL	von Hippel-Lindau
ZO-1	Zonula occludens-1
$\alpha_V\beta_3$	$\alpha_V\beta_3$ integrin, or CD61
ΔP	Pressure difference across the membrane
$\Delta\Psi_m$	Transmembrane potential

Chapter 1: General introduction

Review article published as: He, S., Singh, D., & Helfield, B. (2022). An Overview of Cell Membrane Perforation and Resealing Mechanisms for Localized Drug Delivery. *Pharmaceutics*, *14*(4), 886. https://doi.org/10.3390/pharmaceutics14040886

1.1 Foreword

The central theme of this thesis revolves around the methodology of gene delivery through focused ultrasound. This chapter begins with an overview of a few possible gene delivery methods, such as ultrasound-induced cell membrane permeabilization, summarized from my review article. I then discuss the applications of these methods for the purpose of treating cardiovascular diseases such as ischemia, as well as the role of my microRNA of interest, microRNA-126. Next, I describe how the principle behind focused ultrasound and ultrasound contrast agents can guide gene delivery. I subsequently review the current clinical applications of focused ultrasound before providing the rationale behind my work presented in Chapters 2 and 3, where I delivered microRNA-126 to endothelial cells in both *in vitro* and *ex vivo* models.

1.2 Overview of cell physical plasma membrane permeation techniques

Drug delivery techniques have revolutionized the field of precision medicine, helping to convert promising therapeutics into successful therapies[1]. The overall concept is to locally deliver high concentrations of therapeutics, either actively or passively, to the disease site and minimize off-target deposition. In so doing, the major limitations of systemic drug administration can be curtailed, including low solubility, poor biodistribution, unfavorable pharmacokinetics, and lack of selectivity[2]. Indeed, the major classes of therapeutic compounds, including small molecules, proteins and peptides, monoclonal antibodies, nucleic acids, and live cells, have all been

incorporated into drug delivery systems and made significant contributions towards the treatment of disease[3]. Despite this exciting progress, there remain significant challenges in designing drug delivery tools, most notably in maintaining therapeutic stability, target specificity, and penetration of biological barriers (*e.g.*, cell membranes)[4].

The current techniques for intracellular delivery can be broadly characterized into two sub-types: carrier-mediated delivery and membrane-permeating delivery[2–5]. Carrier mediated approaches rely on biochemical constructs, including drug-loaded nanoparticles, viral vectors, and extracellular vesicles, to overcome some of the limitations of naked drug delivery[4]. Systems based on nanoparticle or microparticle constructs have allowed the deposition of otherwise low-solubility drugs, enabled the trafficking of small molecules to their site of action, and increased drug retention in tumour sites[6]. Environmental modifications, including the addition of cell-penetrating peptides, can aid in plasma membrane penetration and endosomal escape[3].

Membrane-permeating strategies are physical methods that use an external force to puncture the cell membrane and allow direct access to the intracellular space, thereby bypassing the need to overcome the plasma membrane barrier and escape from early endosomes. However, unlike carrier-based methods, the target cells must respond in a timely manner to repair the temporary damage sustained to the plasma membrane[7–9]. Individual eukaryotic cells can quickly repair their plasma membranes after injury through a sequential, highly localized process that restores internal homeostasis and prevents cell death[8–10]. The physical perforation methods currently used for drug delivery use external forces of different origins, including electric fields, ultrasound, and light, and thus are expected to result in characteristically different pore dynamics, including the spatiotemporal coordination of the key components involved in wound repair.

While aspects of cellular membrane pore repair mechanisms have been previously reviewed, the current manuscript aims to link the physical methods of membrane perforation with membrane repair biomechanics and to identify techniques that may be implemented for the development of improved drug delivery systems.

1.3 Drug delivery systems

1.3.1 Microinjections

Perhaps the most direct and established technique for membrane permeabilization is microinjection using a fine-tipped micropipette, typically characterized by an outer diameter on the order of 200–1000 nm. Used to create a single membrane pore on a single cell for therapeutic delivery, this approach requires a precision translational stage and a micro-injector performed under a high-gain objective microscope[11]. Since its original application over forty years ago, microinjection has been a reliable technique for delivering nucleic acid to the cell cytoplasm or directly into the nucleus, which bypasses cytoplasmic degradation. Microinjection is an extremely efficient method for a variety of payloads, irrespective of particle size and charge, including peptides, proteins, and oligonucleotides, and the exact number of DNA molecules can be precisely controlled. It is, however, a low throughput technique that is best suited for specialty applications. Indeed, it is currently widely used to generate transgenic animals[12] through microinjection of a transgenic construct into the pronucleus of a fertilized egg (oocyte or zygote), including mice, pigs, goats, and cattle[13,14], and it is also used in forms of *in vitro* fertilization[15].

1.3.2 Sonoporation

One of the more recent techniques to increase plasma membrane permeability uses ultrasound energy. Biomedical ultrasound is widely employed as an imaging modality for anatomical assessment, as well as to provide information on blood flow characteristics. As an

acoustic wave is transmitted into the body, reflections are generated at tissue interfaces and recorded to generate an image[16]. Ultrasound contrast agent, which consists of a solution of encapsulated bubbles typically between 1 and 8 μm in size, gives rise to strong scattered echoes from the vasculature in which they are confined—much stronger than red blood cells[17]. Contrast-enhanced ultrasound imaging is currently employed clinically in cardiology and radiology applications to improve the delineation of vessel lumen and to enable the visualization of the microcirculation[18]. Microbubbles vibrate within an ultrasound field, expanding and contracting about their resting size, and exhibit a rich variety of dynamic behaviours that are functions of the transmit conditions (acoustic frequency, peak-negative pressure, pulse duration, and duty cycle), the intrinsic bubble properties (size, shell characteristics, and constituents), and the local boundary conditions (vessel constraints)[19]. These behaviours range from stable and spherically symmetric vibrations to shape distortions, bubble fragmentation, and violent bubble collapse. It has been shown through numerical simulations and careful experimental investigations that microbubble oscillations create complex local fluid dynamic patterns; when situated adjacent to vessels, they can create local shear stresses that may ultimately modulate vasoactivity[20], vascular permeability[21], and local cell membrane perforation[22]. Indeed, a microbubble acts as a force actuator, focusing ultrasonic energy on the millimeter scale (typical wavelengths $0.75 \leq \lambda \leq 3$ mm) to micro-manipulate neighboring plasma membranes[23] or generate an individual sub-micron- to micron-sized membrane perforation[24,25]—a process termed sonoporation. Under the assumption that blood is a Newtonian fluid, the shear stress *t* due to a vibrating microbubble of size R_0 can be estimated as

$$\tau \approx 2\,(\mu\rho)^{1/2}(\pi f)^{3/2}(\varepsilon R_0) \qquad (1.1)$$

where μ is the fluid viscosity, ρ is the fluid density, f is the transit frequency, and ε is the maximum radial excursion of the bubble.

Among other design factors, recent work has demonstrated that microbubble proximity to the target cell is a key parameter in sonoporation efficiency, requiring distances on the order of a microbubble diameter or less between them[26]. Efforts to minimize microbubble–cell distances are currently being investigated, including the coupling of targeting ligands within the bubble encapsulation to promote site-specific microbubble accumulation (*e.g.*, $\alpha_V\beta_3$[27]), and novel ultrasound pulse sequences to initiate microbubble translation towards neighboring cells using acoustic radiation force. Investigations employing static techniques post-treatment, including scanning electron microscopy and atomic force microscopy, reveal sonoporation-induced pore diameters ranging from 10 to 1200 nm in diameter[28–31] and, depending on the acoustic conditions, broadly consistent with microscopy studies that infer these spatial scales from intracellular fluorescence tracer uptake dynamics interpreted via diffusion models[32]. Real-time microscopy approaches that directly observe and quantify membrane perforation during sonoporation events[24,33] have shown that these pores exhibit rapid opening timescales (<1 min) and longer resealing timescales (>1–10 min) and can resemble transmembrane apertures. Given the fundamental nature of sonoporation, that is, the generation of very-high-magnitude shear stress (~>kPa) acting on very short timescales (~s), the spatial–temporal characteristics of microbubble-assisted membrane perforation and their relationship to different cell types are not well understood.

Since the discovery of the potential for microbubble-mediated therapeutic delivery in the 1990s[34], there have been many investigations into sonoporation efficiency within the fields of cardiovascular disease[35], brain disorders[36], cancer[37], and immunotherapy[38] that highlight the successful delivery of therapeutic macromolecules, plasmid DNA, mRNA, oligonucleotides, and

associated viral vectors. Perhaps the simplest approach towards microbubble-mediated drug delivery is via a co-injection, whereby local therapeutic macromolecules migrate to the extravascular or intracellular space through sonoporation-derived perforations due to passive diffusion. Current pre-clinical and clinical trials using MR-guided microbubble-mediated blood–brain barrier disruption employ this technique for localized drug delivery[39]. Through advances in microbubble synthesis techniques, other platforms are being developed that incorporate therapeutic payloads into the bubble itself, including drug loading within the encapsulation material and strategies that attach payloads to the surface of the microbubble shell (e.g., electrostatic interactions[40] or nanoparticle linkage[41]). For gene delivery applications, these constructs have shown an increased resistance to nucleic acid degradation within blood serum[42] and thus exhibit a significantly longer half-life than otherwise unshielded gene approaches. Given that microbubbles are currently clinically approved for ultrasound contrast imaging, sonoporation- and ultrasound-microbubble-assisted therapies present an inherently image-guided *in vivo* approach to targeted drug delivery. These therapies fit many requirements of an ideal gene delivery platform, such as minimal procedural invasiveness, limited off-target deposition due to tight acoustic focussing and biochemical ligands, ease of repeated treatments, and a good safety profile in preclinical studies. Additionally, current advances in device development have introduced techniques for passively detecting and quantifying regions of microbubble-treatment in real-time for the purposes of treatment monitoring and quality control[43].

1.3.3 Electroporation

Electroporation is a technique whereby cellular membranes exhibit increased permeability to macromolecules when exposed to an external electric field. While the mechanisms are not yet fully elucidated, it is generally accepted that nanopores are generated within the plasma membrane

upon exposure to high-magnitude electric fields of a given duration. Under physiological conditions, a cell maintains a potential difference across its plasma membrane of approximately -50 to -80 mV, in which its intracellular contents maintain a slightly negative charge compared to the extracellular environment[44]. Under an applied external E-field E_{ext}, the induced transmembrane potential $\Delta\Psi_m$ across a cell membrane of effective radius R_c is generally given by[45]:

$$\Delta\Psi_m = f_s E_{ext} R_c \cos\theta \tag{1.2}$$

where θ is the polar angle between the normal vector of the electric field and the site on the membrane at which $\Delta\Psi_m$ is evaluated and f_s is a dimensionless term related to the electrical properties of the cytosol, plasma membrane, and the extracellular compartment, typically taken as f_s 1.5 for most mechanistic studies[46]. To achieve enhanced cell membrane permeability, a transmembrane potential threshold on the order of $\Delta\Psi_m \approx 1$ V is required, slightly dependent on cell type[46,47]. The generation and characterization of these nanopores are dependent on the pulse parameters, including pulse height, width, and duration. Electroporation typically generates many pores within the plasma membrane with theoretical estimates of pore density on the order of 10^9 pores/cm^2 [48], the majority of which are < 1 nm in radius[49]. The kinetics of the transmembrane transport that is achieved with this approach can be approximated in five stages: (i) pore initiation (~0.1–1 μs); (ii) expansion (~ms), lasting as long as the pulse remains above the threshold value; (iii) stabilization (~ms), a stable decrease in permeability while the pulse is turned off; (iv) resealing (seconds to hours), the return to baseline permeability; and (v) the gradual cessation of residual memory effects (hours), which refers to the observation that cells, even after full membrane resealing, still exhibit alterations in their physiological processes before returning to their equilibrium state[50].

Similar to other types of physical permeation strategies, electroporation can be divided into two distinct types: reversible electroporation (RE), in which the nanopores are transient and the plasma membrane integrity is restored, or irreversible electroporation (IRE), in which the perforations do not reseal, resulting in cell death. Indeed, electroporation has been used successfully to introduce a variety of molecules into cells[51,52], including ions, drugs, RNA, micro-RNA, and DNA. While many studies have investigated the optimal parameters, a starting point for conditions that achieve cell permeation with high cell viability (*i.e.*, RE) is applying eight square waves of 100 μs in duration at a frequency of 1 Hz and an amplitude of 1.2 $kVcm^{-1}$—with the recognition that other factors, including cell size (Equation (1.1)), temperature, and the desired therapeutic agent, may play a role in these applied parameters[47]. *Ex vivo* applications typically involve blood cells treated outside the body and then reintroduced to provide therapeutic benefits. Electroporation has been employed on stem cells[53] to introduce chimeric-antigen receptor genes in T cells[54] and to modify red blood cells[55]. For *in vivo* applications of this technique, naked injection of the therapeutic into the target tissue is required prior to the application of the external E-field. The E-field is generated via electrodes placed in direct contact with the tissue, and therefore target regions are limited to those that both the therapeutic and the electrodes can access safely. This being said, *in vivo* electroporation has been demonstrated in the liver, bladder, brain, muscle, and skin[56,57].

It is important to note that recent works have investigated IRE as a primary, desired endpoint[44]. As a non-thermal tissue ablation modality capable of treating clinically sized volumes of tissue, under certain conditions, this approach allows for the preservation of collagenous and other protein/ lipid-based structures, including the vasculature[58]. This relative advantage over other ablative approaches, as well as its relatively short treatment time requirement, has motived

investigations into many soft-tissue cancer types[59,60], including pancreas, prostate, liver, lung, and brain—resulting in more than 50 clinical trials since its inception over a decade ago[44].

1.3.4 Photoporation

Photoporation, otherwise referred to as optoporation, is a technique in which highly focused light is the source of membrane perforation. In this technique, a laser beam is typically focused on a spot with a size on the order of 0.5–1 μm by a high numerical aperture microscope objective lens to the plasma membrane of a cultured monolayer. Photoporation has been demonstrated using continuous-wave light exposure, as well as pulsed laser modes, including pulse durations in the millisecond, nanosecond, and femtosecond timescales[61]. Modifying the operating mode of the laser and its physical characteristics, such as wavelength and energy density, alter the physical and chemical mechanisms for induced cell membrane perforation[62]. Continuous-wave operation likely relies on heat deposition to induce membrane perforation and is often performed in the presence of an absorbing dye in the culture media. Although it causes perforation on a single cell level with high resulting cell viability, the pores generated by continuous-wave approaches are not as efficient as other modes[61].

Pulse laser sources with very high irradiances (e.g., 10^{10} - 10^{12} Wcm^{-1}) locally generate large E-fields (10^{6} - 10^{7} Vcm^{-1}) compared to the average intramolecular Coulomb fields, resulting in the breakdown of target molecules in the focal region[63]. With slightly longer pulses in the nanosecond range, this can be accompanied by heating, bubble formation, and thermoelastic stress[64] that can expand the spatial scale of perforation to tens of microns[65]. Pore sizes generated by this technique range from ~10 to 1000 nm, depending on the parameters of the laser source[66]. Currently, the most widely adopted approach to optoporation is the use of femtosecond lasers (~<200 fs pulse durations), typically at 800 nm[61]. Since the original demonstration over thirty years

ago to deliver DNA into rat kidney cells[67], a wide array of membrane-impermeable substances have been delivered in this way with high cell viability, including dyes, nanoparticles, DNA, and mRNA[68,69]. Additionally, photoporation can be achieved in combination with gold nanoparticles to increase the likelihood of perforation for a given set of input conditions[70], presumably due to the local amplification of the E-field[62]. Optoporation provides a means to robustly perforate cell membranes; however, it is mostly restricted to *in vitro* applications due to the low penetration depth *in vivo* and the requirement for complex optical setups. Table 1.1 below summarizes these techniques.

Table 1.1: A summary of the salient features of the main physical methods used to generate plasma membrane perforations.

Method	Pore features	Relative advantages	Relative disadvantages
Microinjection	Single pore of similar size to the fine-tipped glass micropipette (~200-1000nm).	• Extremely efficient (~100%) • Precise control over payload concentration	• Very low throughput • Highly technical • Not applicable for *in vivo* drug delivery
Sonoporation	Pore radii ranging from submicron to 10μm. Single pore per bubble with the possibility of multiple pores per cell.	• *In vivo* translatability • Drug/ gene loaded constructs for added spatial targeting • Image-guided • Non-invasive	• Highly dependent on ultrasound transmit and physical acoustic parameters
Electroporation	Pore radii generally <1nm with up to 10^9 pores per cm^2.	• Very good efficiency • Efficient for *ex vivo* applications	• Semi-invasive procedure • Limited *in vivo* applications • Requires therapeutic co-injection
Photoporation	Pore radii ranging from 10-2000nm	• Very good efficiency, depending on the laser mode of operation	• Low throughput • Limited *in vivo* applications • Requires therapeutic co-injection

1.4 Cardiovascular diseases and ischemia

1.4.1 Current treatment regimes

Cardiovascular diseases (CVD) represent a broad category of disorders affecting the heart and blood vessels, and remain to be the leading contributor to global mortality[71]. Within the context of CVD, ischemia is characterized by a state of reduced blood flow and poses significant threats to the affected tissues or organs[72,73]. The insufficient perfusion of oxygenated blood triggers a cascade of harmful cellular events, potentially leading to tissue damage, dysfunction, and infarction or necrosis in severe cases[74]. The impact of ischemia varies depending on the affected organ. In the heart, it can manifest as an angina, myocardial infarction or heart failure, while in the brain, it can result in stroke and cognitive impairment[75,76]. Ischemia in the limbs can lead to peripheral artery disease or critical limb ischemia, which sometimes requires amputation[77]. In the intestines, it can manifest as mesenteric ischemia, which can cause bowel damage[78]. As for atherosclerosis, the buildup of plaques in the arteries from chronic inflammatory disease, is another major contributor to ischemia and other CVD. The narrowing of blood vessels (stenosis) due to atherosclerotic plaques significantly reduces blood flow[79]. Typically, healthy vessels allow for smooth, laminar flow, but the plaque buildup in atherosclerotic vessels causes turbulent flow, which reduces perfusion and increases the risk of clot formation (thrombosis)[80].

Some treatment strategies for ischemia and atherosclerosis may include percutaneous coronary intervention, involving the placement of stents to restore blood flow, sometimes combined with a drug which releases antiproliferative drugs to prevent stenosis called drug eluting stents[81]. Thrombolytic agents, such as recombinant tissue plasminogen activator (rtPA) are also commonly administered to dissolve clots[82]. In more severe cases, bypass surgery or endovascular therapy may be required to restore blood flow and prevent further complications, such as sepsis. Despite these advancements, ischemia and atherosclerosis still poses significant challenges, and

ongoing research continues to explore novel therapeutic techniques, such as gene therapy[83] and anti-inflammatory agents[84] aimed at addressing these conditions while minimizing adverse effects.

1.4.2 Brief summary of angiogenesis

The process of angiogenesis, or blood vessel growth, begins with under-perfused or ischemic tissues undergoing hypoxia, or the lack of oxygen. Under hypoxic conditions, hypoxia-inducible factor 1 (HIF-1α) accumulates in hypoxic cells[85]. HIF-1α plays a crucial role in regulating genes involved in angiogenesis, including the vascular endothelial growth factor (VEGF). Among the many growth factors secreted by hypoxic cells (*e.g.* Angiopoitin-2, Ang-2; fibroblast growth factor, FGF; endothelial growth factor, EGF; transforming growth factor-beta, TGF-β), VEGR is the main regulator of angiogenesis because of its involvement in many pathways[86]. Under pro-angiogenic contexts, the VEGF-A isoform binds to its respective receptor VEGFR2 on endothelial cells, triggering a series of cellular processes, as summarized in Figure 1.1.

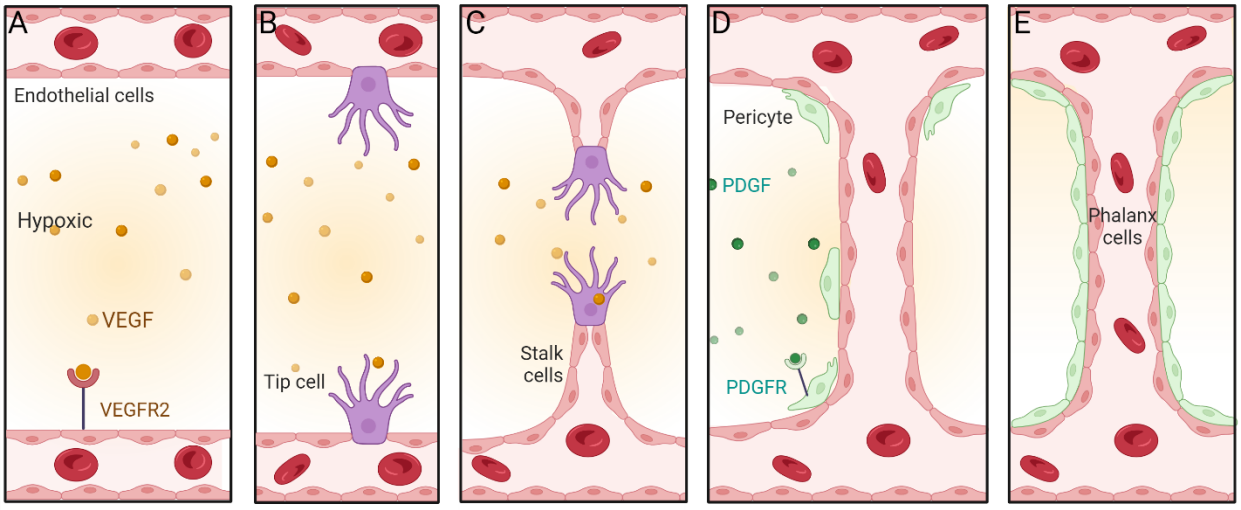

Figure 1.1: Simplified process of angiogenesis. (A) Tissues in a hypoxic environment (orange gradient) secrete proangiogenic factors, such as VEGF binding to VEGFR2 on endothelial cells. (B) Tip cell selection. (C) New vessel elongation. (D) Tip cell fusion, lumen formation and pericyte recruitment through PDGF and PDGFR binding. (E) Vessel maturation and tissue perfusion. Figure modified from a BioRender.com Template from Noeline Subramaniam[87].

During angiogenesis, the endothelial cell receiving the highest concentration of VEGF will differentiate into a leading tip cell (Figure 1.1B), which will adopt a cellular morphology consisting of filopodia extensions, VEGFR1 and VEGFR2[88]. These structures aid in the migration of endothelial cells and guiding new vessel formation towards the gradient of VEGF. The VEGF-A isoform also binds to VEGFR1, although its weak kinase activity does not trigger any signaling pathways, but instead sequesters VEGF-A, lowering its bioavailability to the neighbouring endothelial cells[89]. The activation of VEGFR2 on the tip cell upregulates the transmembrane ligand Delta-like 4 (Dll4) which binds to the Notch receptors on neighbouring endothelial cells[88]. Notch desensitizes these endothelial cells to VEGF, pushing their differentiation towards stalk cells instead of tip cells, which will be forming the tube of the sprouting vessel. Stalk cells are more abundant in VEGFR1 than VEGFR2, which limits excessive tip cell differentiation[90]. These processes ensure that the formation of vessels is orchestrated in a controlled and viable manner.

As the tip cell migrates, it secretes matrix metalloproteinases (MMP) to remodel the extracellular matrix and loosen intercellular junctions[91]. This encourages pericyte detachment to allow newly sprouting vessel to elongate[88] (Figure 1.1C). Once the tip cells of newly sprouted vessels meet, they anastomose and form a lumen[92] (Figure 1.1D).

The binding of VEGF-A to VEGFR2 on endothelial cells promotes the secretion of the pro-angiogenic factor platelet-derived growth factor (PDGF)[93]. TGF-β guide pericyte differentiation, and PDGF will then bind to its receptor PDGFR on pericytes and further initiate pericyte recruitment proliferation to provide structural support to the endothelial cells[90]. The perfusion of the newly formed vessels decreases the secretion of pro-angiogenic signals and increase pro-quiescence signals, allowing the stalk cells to become phalanx cells[90] (Figure 1.1E). This allows blood perfusion to the capillaries and sets the tissues to normoxic conditions, as

opposed to hypoxic, where HIF-1α is degraded by the tumor suppressor von Hippel-Lindau (VHL) in the presence of oxygen[90,94].

Given the central role of the VEGF pathway in angiogenesis, targeting specific steps within this pathway represents an effective strategy for regulating vessel growth. For instance, microRNA-126 (miR-126) has been shown to influence angiogenesis by targeting downstream components of the VEGF pathway, which will be described below.

1.4.3 Role of miR-126 in angiogenesis pathway

The binding of VEGF to VEGFR2 on endothelial cells triggers a signaling cascade to initiate angiogenesis, as summarized in Figure 1.2. MiR-126 exerts its pro-angiogenic effects in endothelial cells by targeting multiple key regulators of vascular growth and remodeling, as well as being the most highly expressed miR in endothelial cells[95]. Two of its primary targets are Sprouty-related EVH1 domain-containing protein 1 (SPRED1) and phosphoinositide-3-kinase regulatory subunit 2 (PIK3R2), which are negative regulators of the VEGF[96]. By downregulating SPRED1, miR-126 allows the RAS/ MEK/ ERK pathway to proceed unimpeded. The activation of ERK promotes cell survival by phosphorylating and inactivating pro-apoptotic proteins like Bad and by increasing the expression of anti-apoptotic protein Bcl-2[97]. This leads to the activation of ELK1, which promotes the expression of genes involved in cell proliferation[98]. The end product from ERK activation promotes cell motility[99]. PIK3R2 also negatively regulates the PI3K/ Akt signaling pathway, and miR-126 negates those effects. Akt contributes to cell survival, cell proliferation and growth by inhibiting GSK3β and mTOR inhibitor TSC2, both involved in metabolism, survival and migration[100]. Akt also stimulates the production of nitric oxide (NO), through endothelial NO synthase (eNOS)[101], a vasodilator that supports reperfusion.

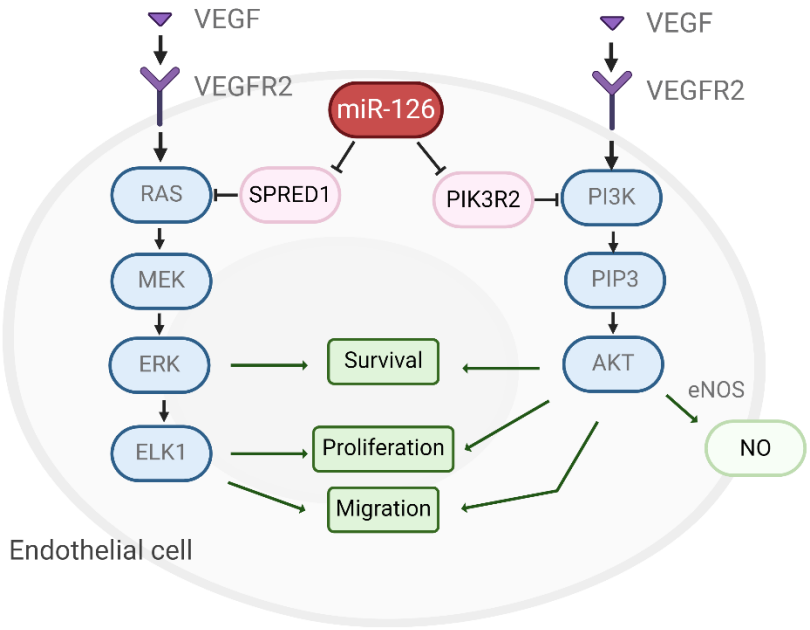

Figure 1.2: An overview of the downstream effects of miR-126 in endothelial cells. Figure created on BioRender.com.

1.4.4 miR synthesis

MicroRNAs are a class of short, endogenous and non-protein coding RNA of about 23 nucleotides long and are involved in post-transcription regulation of animal and plant genes[102]. They exert their regulatory function by binding to the 3'-untranslated region (3'UTR) of target mRNAs to repress protein translation[103]. The synthesis of miRs is initiated in the nucleus, where the miR gene is transcribed by DNA polymerase II into a primary-miRNA (pri-miRNA). The microprocessor Drosha and its DCGR8 subunit cleave the pri-miRNA into a precursor miRNA (pre-miRNA), which consists of mismatched bases, a loop and 70-100 nucleotides[104]. Exportin-5 then exports the pre-miRNA into the cytoplasm, where the enzyme Dicer further cleaves the miRNA strand into a 18-25 nucleotide long double stranded mature miRNA, consisting of a passenger strand and a guide strand[104]. The mature miRNA then interacts with the RNA-induced silencing complex (RISC) to discard of the passenger strand, and the remaining guide strand will be able to recognize their mRNA targets at bases number 2-8 and bind to their complementary

bases at the 3'UTR[102]. A notable feature of miRNAs is their ability to bind to multiple mRNA targets without requiring perfect complementarity[105]. This unique characteristic enables them to exert broad regulatory influence over crucial pathways, like VEGF as mentioned above, which highlights their significance in the regulation of cellular processes.

Although there are numerous other targets of miR-126, SPRED1 and PIK3R2 were chosen as the focus of Chapter 2 because of their VEGF-dependent role in regulating angiogenic pathways and are well studied[96]. Some other miR-126 targets have roles in inflammation (*e.g.* vascular cell adhesion molecule 1, VCAM-1[95]; high-mobility group box 1, HMGB1[106]), wound healing and vessel integrity (*e.g.* HIF-1α[107]; EGF-like domain 7, EGFL7[108]). The roles of these targets may overlap, and consequently have an indirect effect on angiogenesis.

1.5 Focused ultrasound in therapy

1.5.1 Background on ultrasound imaging and definition of ultrasound parameters

Ultrasound imaging is a non-invasive diagnostic modality that utilizes high frequency sound waves (1-10 MHz) to generate visual representations of internal body structures[16]. It is widely used in obstetrics, radiology, and cardiology, among other disciplines, to assess the condition of organ, tissues, and blood vessels. By transmitting mechanical waves from a transducer, these sound waves interact with tissues and organs and reflect back to the transducer as echoes[16]. The ultrasound system then processes these echoes to create a visual representation of the internal structure. The intensity of the echoes determines the brightness and location of the structures in the image. Different tissues have varying densities, which affect the velocity at which the sound waves traves through. Higher ultrasound frequencies emitting from the transducer offer better resolution for visualizing smaller structures, and lower frequencies can penetrate deeper tissues at the expense of the resolution quality[109].

An ultrasound wave can be described as a sine function that oscillates between a maximum and minimum value, known as the amplitude, and represents the pressure variations over time. The amplitude determines the intensity of the wave, which will be translated to a peak negative pressure (PNP) for our experiments, and each wave corresponds to a cycle. The incident acoustic frequency is set by the chosen transducer and sets the period of each cycle. For instance, the period of a 1 MHz transducer is 1 μs whereas the period of a 2.25 MHz transducer is 0.444 μs. Typically, therapeutic ultrasound is transmitted in pulses, and the interval between pulses is the pulse repetition interval (PRI). This value is required to calculate the duty cycle, which is the percentage of time that the ultrasound waves are on, and is indicative of the total intensity of the treatment. A representation of these terms is sketched in Figure 3.1D. Another common term to assess the treatment intensity is the mechanical index (MI), which is defined as the acoustic pressure scaled by the square root of the frequency[110]. For imaging purposes, the maximum value allowed by the Food and Drug Administration (FDA) is 1.9 to limit tissue damage[111].

1.5.2 Ultrasound contrast agents

While conventional ultrasound imaging provides valuable information about anatomical structures, its ability to visualize blood flow is limited. To increase the echogenicity, or the ability to enhance the reflection of sound waves, ultrasound contrast agents called microbubbles are often intravenously administered[112]. They are often made of phospholipids, polymer or albumin shells that encapsulate an insoluble gas[113]. Under low intensity ultrasound, a microbubble can undergo stable cavitation, where it expands and contracts around its equilibrium size, or inertial cavitation at higher MI to induce microbubble destruction[114]. As mentioned in Chapter 1.3.2, the events following microbubble cavitation can facilitate cell membrane permeabilization for drug or gene delivery and are depicted in Figure 1.3.

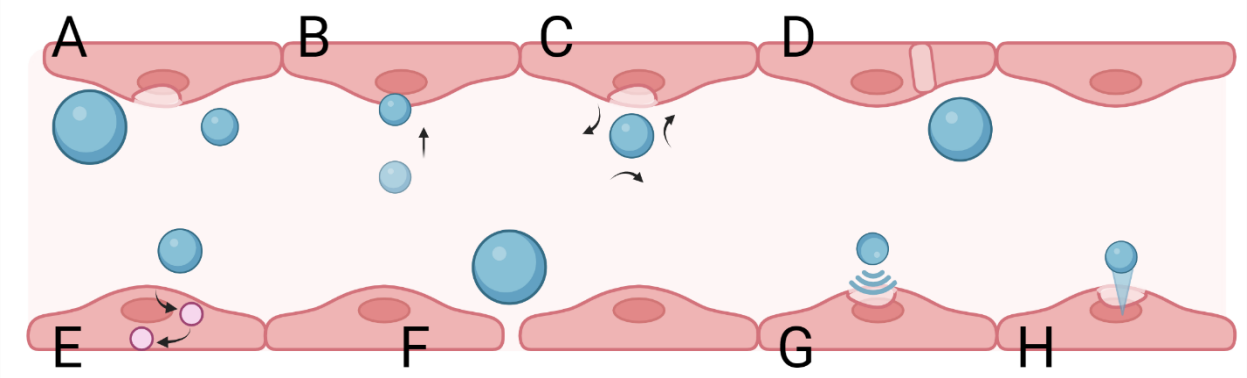

Figure 1.3: Cellular and vascular permeabilization by microbubble cavitation. (A) Expansion and compression can push and pull on the cell membrane. (B) Acoustic radiation force, pushing the microbubble towards the cell membrane. (C) Microstreaming generates shear stress near a cell. (D) Transendothelial perforations[115,116]. (E) Enhanced endocytosis and transcytosis[117]. (F) Opening of intercellular gap junctions[116]. (G) Shockwaves and (H) microjetting from microbubble collapse. Adapted from [118] and [114]. Figure created on BioRender.com.

Some of the widely used commercially available and FDA-approved microbubbles include: Definity® (Lantheus Medical Imaging), made of a phospholipid shell and octafluoropropane gas (C_3F_8)[119]; Optison™ (GE Healthcare), made of an albumin shell and perfluorobutane (C_4F_{10})[120]; and SonoVue® (Bracco), made of phospholipids and sulfur hexafluoride (SF_6)[121]. The difference in shell composition, gas core and "activation" method (*i.e.* mechanical agitation or sonication) affect the microbubble size distributions and their response to ultrasound frequencies[122]. Those characteristics distinguish each of these products that were tailored to image specific organs, but the most important feature that favours phospholipid-based shells is mostly attributed to stability and echogenicity[123].

In addition to the diagnostic role of microbubbles in imaging, recent advancements on modified microbubble formulations have enabled the development of molecular imaging and targeted therapeutics delivery. One method consists of attaching a ligand on the microbubble surface to specifically target receptors on the surface of cells of interest. One particularly interesting formulation is BR55 from Bracco, where a heterodimer peptide specific for VEGFR2

is coupled to the polyethylene glycol moieties from the phospholipids on the microbubble shell[124]. Since endothelial cells of the tumor vasculature are rich in VEGFR2, it has been shown to greatly increase image intensity in rat tumors compared to untargeted microbubbles by localizing their accumulation towards cells with high VEGFR2 expression[124]. This formulation has been used as a diagnostic tool in human patients with prostate cancer[125] and for characterizing malignancy in mice models of renal cell carcinoma[126]. Another method may consist of modified microbubbles to carry therapeutic payloads, either encapsulated in liposomes attached to microbubbles (*e.g.* through biotin and streptavidin interactions[127]), or directly onto the surface of a charged microbubble in the case of genes (*e.g.* anti-EGFR-siRNA[128], miR-34a[129] and miR-126[130]) or plasmids (*e.g.* plasmids containing luciferase cDNA[131,132]) through charge interactions. This approach offers the advantage of protecting the gene from endogenous nucleases in the circulation[128] as well as increasing the half-life of the drug[133]. These targeted approaches enhance the accuracy of therapeutic deposition by directing microbubbles to the areas of interest[134], as well as releasing the therapeutic payload solely to the sonicated area and limit off-target effects[135].

1.5.3 Applied bioeffects of focused ultrasound

Since microbubbles are intravascular agents, one of the first cells they encounter are endothelial cells. As previously outlined in Chapter 1.3.2, microbubbles undergoing cavitation can transiently disrupt cell membrane permeability by forming a physical pore for drug and gene delivery[25] that reseals within 180 seconds[136]. This process also enhances endocytotic activity for drug uptake[137], and generates intracellular tunnels that allow macromolecules diffusion across the endothelium[115]. Beyond physically opening of the cell membrane, the mechanical effects caused by the cavitating microbubbles, such as shear stress, can trigger an increase in Ca^{2+}, essential for cell membrane resealing and maintaining the integrity of the endothelial layer[9] (discussed further

in the Appendix). Additionally, these effects promote the release of NO and ATP, which enhance vascular reactivity and support endothelial function[138,139].

Through the process of sonothrombolysis, the release of NO can improve local blood flow and clot erosion. The mechanical stress induced by cavitating microbubbles can disrupt the fibrin structure of clots, which helps co-administered thrombolytic agents (like rtPA) to further dissolve clots[140]. To aid in localizing microbubbles towards the clot, modified microbubbles targeted to platelets have also been studied, which has been shown to completely restore flow within 2 hours[141]. Thrombolysis has also been demonstrated to be effective with high intensity focused ultrasound without requiring microbubbles, which is particularly interesting when it is difficult to focus ultrasound on a microbubble through the skull during a stroke[142].

Following microbubble cavitation, the resulting increase in Ca^{2+} can propagate to neighbouring cells through gap junctions[136], leading to the opening of cell-cell contacts within endothelial monolayers[143]. In an *in vivo* context, this process could explain the observed increase in vascular permeability in vessels of interest, such as those in the brain parenchyma, protected the blood brain barrier (BBB). The BBB is a highly selective, semi-permeable membrane that restricts most molecules larger than 400-600 Da from the bloodstream into the brain[144]. It is composed of a network of specialized endothelial cells held together by tight junctions, adherens junctions and scaffolding proteins, and their lack of fenestrations further reinforce the barrier[145]. Additional processes, such as pumps and efflux transporters (*e.g.* P-glycoprotein [P-gp]) and breast cancer resistance protein (BCRP), actively expel substances back to the circulation, making drug delivery to the brain a challenge[146]. To address this issue, researchers have developed techniques to temporarily and non-invasively open the BBB using magnetic resonance-guided focused ultrasound (MRgFUS) combined with cavitating microbubbles. One such innovation is the

transcranial phased array transducer, which consists of 1024 individual transducers (*i.e.* the ExAblate Neuro from InSightec), that can direct ultrasound waves within millimeters accuracy across the human skull[147], or an implanted ultrasound device for repeated treatments (SonoCloud from CarThera)[148] in the case of recurrent glioblastoma. The increase in BBB permeability has been attributed to four mechanisms: the disruption of junctional proteins between endothelial cells, enhancing transcellular transport, the formation transendothelial fenestrations, and direct diffusion through the endothelial layer[116]. These processes are controllable and reversible, and the BBB can remain open up to 6h without any signs of hemorrhage or edema[149]. The temporary increase in permeability allows the delivery of chemotherapeutics, genes[150], and even neural stem cells[151] that would otherwise be unable to cross the BBB.

1.5.4 Clinical applications of focused ultrasound

The diverse and controllable bioeffects of focused ultrasound, ranging from precise tissue disruption to controlled modulation of tissue permeability, have paved the way for its exploration in a broad spectrum of clinical applications. This section lists a few examples of current clinical applications and trials in diverse areas, from movement disorders to cancer and stroke[152].

One of the most impactful clinical advancements in the field of focused ultrasound is its ability to open the BBB and treat otherwise inoperable cancers. The increase in vessel permeability allows for the precise delivery of chemotherapeutics in brain metastases (clinical trial number: NCT03714243[39]) or to advanced stages of breast cancer (ChiCTR2200056718[153]) in order to reduce the tumor size and clinical stage. Through neuromodulation, focused ultrasound can also activate microglial cells to reduce amyloid-beta plaques[154] for the treatment of Alzheimer's (NCT02986932[155]). Another important progress is the treatment of essential tremors by thermal ablation, done with high intensity focused ultrasound to raise the temperature of precise locations

of the thalamus up to 60°C to create small lesions, which has been approved since 2016 (NCT01827904[156]). A similar approach for the treatment of Parkinson's disease (NCT01772693[157]) and obsessive-compulsive disorder (OCD; NCT01986296[158]) has also been explored. Additionally, MRgFUS can be employed for the release of biomarkers (*e.g.* cell-free DNA) for liquid biopsies to characterize the disease stage of glioblastomas (NCT03616860[159]) in a less invasive manner. Lastly, the feasibility of sonothrombolysis has been shown to improve perfusion in patients with myocardial infarctions in ambulance settings in Europe[160].

1.6 Research objectives and rationale

Recent clinical studies in focused ultrasound highlight the exciting potential of minimally invasive therapies. While the field of BBB opening and brain cancer treatments have shown great success over the years, few studies have shown the potential of targeted gene therapy for cardiovascular applications in comparison. This is why one of the key goals of this research is to further understand gene delivery, specifically miR-126, to endothelial cells through focused ultrasound in both *in vitro* and *ex vivo* models.

To do so, this research first focuses on optimizing a methodology for gene delivery using cationic microbubbles demonstrate the role of this miR-126 to endothelial cells in an in vitro setting. As previously described, miR-126 plays a crucial role in promoting angiogenesis by regulating pathways involved in blood vessel formation, and the manuscript provided in Chapter 2 serves to demonstrate the feasibility of this approach. Next, to further understand this gene delivery process in a more physiologically relevant setting, there is a need to understand the intrinsic factors that may influence gene uptake in a vessel. To address this challenge, in Chapter 3, I developed an *ex vivo* model of a vessel where I could incorporate variables such as intralumenal pressure and flow velocities. With this model, I aim to understand how gene delivery is affected

by flow velocities, which could be translated to different vessel sizes and possibly disease states, such as atherosclerosis and stenosis.

The overall goal of this research is to enhance our understanding of how focused ultrasound can be optimized for gene therapy in cardiovascular disease, particularly in the case of ischemia. By addressing gaps in knowledge related to the dose delivered as well as the viability of the treated cells of vessels, this thesis aims to lay the groundwork for minimally invasive, ultrasound-guided gene therapies that can promote angiogenesis and improve outcomes in cardiovascular disease patients.

Chapter 2: Stable Cavitation-Mediated Delivery of miR-126 to Endothelial cells

Manuscript published as: He, S., Singh, D., Yusefi, H., & Helfield, B. (2022). Stable Cavitation-Mediated Delivery of miR-126 to Endothelial Cells. *Pharmaceutics, 14*(12). https://doi.org/10.3390/pharmaceutics14122656

2.1 Foreword

Angiogenesis is a key process involved in physiological and pathological conditions associated with ischemia, a major global health challenge in cardiovascular diseases. MicroRNA-126 has emerged as a promising therapeutic target due to its potent pro-angiogenic effects. Given the challenges in delivering therapeutic agents to targeted cells, the following chapter demonstrates the feasibility of delivering miR-126 to cultured endothelial cells using focused ultrasound. I first characterized the formulation and behaviour of miR-126-conjugated cationic microbubbles. Then, I optimized the ultrasound parameters for sufficient miR-126 and assessed the biological effects of the uptake of miR-126 in endothelial cells, while minimizing cell death.

2.2 Abstract

In endothelial cells, microRNA-126 (miR-126) promotes angiogenesis, and modulating the intracellular levels of this gene could suggest a method to treat cardiovascular diseases, such as ischemia. Novel ultrasound-stimulated microbubbles offer a means to deliver therapeutic payloads to target cells and sites of disease. The purpose of this study was to investigate the feasibility of gene delivery by stimulating miR-126-decorated microbubbles using gentle acoustic conditions (stable cavitation). A cationic DSTAP microbubble was formulated and characterized to carry 6 μg of a miR-126 payload per 10^9 microbubbles. Human umbilical vein endothelial cells (HUVECs) were treated at 20–40% duty cycle with miR-126-conjugated microbubbles in a custom

ultrasound setup coupled with a passive cavitation detection system. Transfection efficiency was assessed by RT-qPCR, Western blotting, and endothelial tube formation assay, while HUVEC viability was monitored by MTT assay. With increasing duty cycle, the trend observed was an increase in intracellular miR-126 levels, up to a 2.3-fold increase, as well as a decrease in SPRED1 (by 33%) and PIK3R2 (by 46%) expression, two salient miR-126 targets. Under these ultrasound parameters, HUVECs maintained >95% viability after 96 h. The present work describes the delivery of a proangiogenic miR-126 using an ultrasound-responsive cationic microbubble with potential to stimulate therapeutic angiogenesis while minimizing endothelial damage.

2.3 Introduction

Gene therapy is a treatment regime in which a specific cell function-altering piece of genetic material is introduced into target diseased cells. Typically, DNA, mRNA, siRNA, and anti-sense oligonucleotides are the genetic materials used for this approach, either to restore a specific gene function or to turn off a gene involved in pathogenesis. The first authorized clinical trial for gene therapy was for Gaucher's disease in 1988 (NCT00001234), a lysosomal dysfunction. Mostly due to the fact that it commonly employs viruses to deliver the genetic material, gene therapy was met with mixed success early on in its history[161] owing to complications with the immune response, off-target side-effects, and unwanted or neutral clinical outcomes[162]. Indeed, the critical challenge toward the advancement of this approach is the delivery method itself, and key advances in this field have brought gene therapy back into the spotlight. Nonviral vector approaches, such as systemically injected liposomal constructs, are generally less immunogenic than their viral counterparts, and they can gain target cell specificity through chemical/ biological design. Generally, these vectors are considered less efficient than viral vectors, likely due to the fact that they face the endoluminal border and must escape early endosomes to deliver their payload.

More recently, microRNAs (miRs) have been employed in molecular therapeutics. MiRs are noncoding RNA strands that may bind to multiple mRNA targets and modulate their expressions. Nearly three decades ago, the discovery of dysregulated miR in nematodes[163] allowed insight into a better understanding of disease development in a wide array of pathologies[164–166]. The pleiotropic nature of miRs makes for a particularly attractive choice for gene therapy, *e.g.*, in applications of diseases with a multifactorial origin[167]. Indeed, miR therapy is being explored preclinically in many areas, including cancer (*e.g.*, pancreatic[168], breast[169], lung[170], and leukemia[171]) and cardiovascular disease (*e.g.*, cardiac hypertrophy[172], arrhythmia[173], cardiac fibrosis[174], and ischemia[175]).

With regard to the application of therapeutic angiogenesis for ischemia, miR-126 is a potentially potent target. miR-126 is highly expressed in endothelial cells, and feasibility studies have shown its role in modulating angiogenesis by repressing angiogenic repressors, such as PIK3R2 from the Akt pathway and SPRED1 from the ERK pathway, to name a few [176,177]. Indeed, in selecting a potential candidate technique for miR-126 delivery or any other miR that has shown to be a major molecular regulator in cardiovascular disease, there is particular interest in exploring ultrasound-based techniques, as echocardiography is commonly clinically used to diagnose many cardiovascular diseases[178] .

Ultrasound-sensitive agents, including clinically employed microbubble contrast agents, provide an exciting alternative to more traditional nonviral vectors. Typically between 1 and 8 μm in diameter, microbubbles remain intravascular and are composed of a thin, flexible lipid monolayer shell and vibrate when exposed to ultrasound[179]. Recent studies have demonstrated that, under specific acoustic conditions, ultrasound-stimulated microbubbles can temporarily alter vascular and cellular permeability, thereby providing an endocytosis-independent pathway for

exogenous drug delivery[115,180–182]. Indeed, as these microbubbles only vibrate as they pass through an ultrasound beam, their activity is spatially and temporally targeted, thus having the potential to limit off-target therapeutic deposition.

In microbubble-mediated gene therapy, the design of the microbubble is critical to ensure sufficient loading capacity[183]. One such approach is to synthesize microbubbles with a surface charge to offer a means to attach genetic payload on the microbubble surface, shown to deliver genetic material more efficiently than co-injected with neutral microbubbles[132,184]. Such efficiency is conferred by protection against circulating RNases in the bloodstream to increase the half-life of the short RNA strand, as well as increasing the available genetic material around the tissue when it is coupled to a vehicle, as opposed to free floating in the systematic circulation[42]. Additionally, the non-invasive nature of the methodology allows for repeated treatment to further increase gene delivery efficiency, as well as the ability to spatially target tissues of interest with focused ultrasound limits off target responses[185].

Ultrasound-mediated microbubble behavior is commonly separated into two distinct physical regimes[186]. If bubbles are exposed to acoustic pressures above a specific threshold, they can rapidly expand and violently collapse during the compression of the transmit pulse. This behavior, whereby microbubble disruption occurs, is dominated by the inertia of the surrounding fluid and is typically termed inertial cavitation, accompanied by broadband spectral emissions. Indeed, miR-based delivery using ultrasound and microbubbles has been shown via this acoustic regime, which does result in physical membrane perforation and enhanced cellular and vascular uptake of material[187–190]. In fact, numerous studies have demonstrated the advantage of delivering miR or miR inhibitors through inertial cavitation (typically referred to as ultrasound-targeted microbubble destruction; UTMD) for specific applications, such as cancer cell ablation[187,190,191].

Other applications of gene delivery through UTMD have shown success in preventing organ rejection[192], treating cardiac hypertrophy[188], and even in promoting angiogenesis[189]. While shown to be an effective strategy, microbubble disruption (*e.g.*, inertial cavitation) may trigger severe, undesired bioeffects, including loss of cell viability[193], hemorrhage, or increased inflammation.

Another approach to microbubble-mediated ultrasound gene delivery, which has been less explored, is to ensure a more controlled microbubble oscillation regimen. Generally, bubbles driven by low-pressure ultrasound elicit repeated periodic, volumetric vibrations about their equilibrium size, whereby they may oscillate spherically or non-spherically[194]. Under specific acoustic conditions, these vibrations can enhance cell permeability due to local fluid microstreaming and prolonged shear stress[195]. This regime is called stable cavitation and is characterized by distinct harmonic scattered pressure emissions[186]. In addition to limiting potential unwanted bioeffects, the prolonged fluid streaming and physical presence of the microbubble may aid in intracellular therapeutic deposition.

Indeed, as the majority of investigations of ultrasound-mediated gene delivery rely on bubble destruction, the novelty here is via our intended goal of demonstrating that modest levels of gene therapy can be achieved using gentle bubble vibrations (stable cavitation without bubble disruption), with potential significance toward the design of repeat treatment paradigms. This entails the synthesis of high-capacity gene-loaded microbubble constructs that are clinically feasible in terms of stability, concentration, nonlinear echo, and gene-loading concentration, which is confirmation of small but significant gene delivery so as to preserve cell viability and ensure successful modulation of salient downstream protein expression and physiological endpoints.

In this present study, we aim to investigate ultrasound-mediated gene delivery using stable cavitation, specifically in the context of therapeutic angiogenesis. First, we synthesized and

characterized a cationic lipid microbubble formulation decorated with an miR-126 mimic. Next, we demonstrate that these microbubbles can be used to deliver their miR-126 cargo within endothelial cells in a viable manner while under-going stable cavitation, monitored with passive cavitation techniques. Lastly, we assess the functional and physiological endpoints of the miR-126 delivery.

2.4 Material and Methods

2.4.1 Contrast Agent Microbubble Preparation

Cationic phospholipid-encapsulated microbubbles were synthesized via a modification of an existing in-house formulation[131]. Briefly, the microbubbles were prepared from a lipid aqueous dispersion composed of 1,2-distearoyl-sn-glycero-3-phosphocholine (DSPC; Avanti Polar Lipids, Alabaster, AL, USA), polyoxyethylene (40) stearate (PEG40S; Sigma-Aldrich, St. Louis, MO, USA), and 1,2-stearoyl-3-trimethylammonium-propane (DSTAP; Avanti Polar Lipids, Alabaster, AL, USA). DSPC, PEG40S, and DSTAP (0.41:0.50:0.09) were dissolved in a solution buffer consisting of PBS-EDTA (1 mM), propylene glycol and glycerol (0.80:0.15:0.05) at a concentration of 4 mg/mL. The lipid solution was then dissolved in a 20 kHz ultrasonic bath (Branson Ultrasonics, Danbury, CT, USA) at 65 °C until a homogenous clear solution was observed. Samples of microbubbles were formed by aliquoting 1.5 mL of this solution in glass vials and sealed with a rubber stopper. The air from the vial was removed via vacuum and replaced with perfluorobutane (C_4F_{10}; FluoroMed, Round Rock, TX, USA). To synthesize the microbubbles, vials were allowed to reach room temperature to ensure consistent size distribution and scattering activity[196], subjected to mechanical agitation using the VialMix™ (Lantheus, Billerica, MA, USA) for the standard 45s period, and then were set to cool down to room temperature for 15 min. Vials were then decanted for 8 min to ensure the removal of large

microbubbles, and microbubbles were withdrawn using a 1 inch 19G needle, along with another 19G needle for venting purposes. Agent was consistently extracted from just below the rubber stopper to reduce population variability. After decantation, 0.7 mL was extracted from the glass vial and the microRNA-126 was added to the microtube for incubation. Microbubbles were washed as per described in Wang et al.[132]. Briefly, the mixture was diluted to 1 mL with DEPC-treated diH_2O and centrifuged at 400×g for 3 min in a 3 mL syringe. The bottom 0.5 mL was discarded to remove the smaller microbubbles, and the remainder of the solution was diluted in DEPC-treated diH_2O to fix the concentration to 10^9 microbubbles/mL for the experiments.

2.4.2 Microbubble Characterization

The size distribution, concentration, and stability of these in-house microbubbles were quantified using a Coulter Counter (Multisizer 4e; Beckman Coulter, Brea, CA, USA). Microbubbles were diluted 1:1000 in ISOTON II (Beckman Coulter) and sampled using the 30 μm aperture, which enables an effective measurable size range of 0.6–18 μm. For a given vial, measurements were repeated every 20 min for up to 80 min post activation to assess microbubble stability. For a subset of experiments, the zeta potential was measured using a Zetasizer Nano ZS (Malvern Panalytical, Malvern, UK). Microbubbles were diluted to a 0.2% solution with diH_2O, and measurements were taken within 10 min of having extracted the agent from the vial. For each of these measurements, at least n=3 vials were used for statistical purposes.

To confirm that our agent is acoustically active, the echogenicity of the microbubbles was measured with a clinical ultrasound system (model iU22 Philips Healthcare, Andover, MA) using a C5-2 probe. The microbubbles were diluted 10,000-fold in gas-equilibrated diH_2O and fed into a wall-less 0.8 cm diameter cardiac Doppler flow phantom (model 523A, ATS Laboratories, Norfolk, VA, USA) at a velocity of ~14–16 mm/s. The depth was fixed at 8 mm, and three internal

videos were recorded in B mode and contrast mode for 2 min. The signal-to-noise ratio (SNR) was plotted ± the standard deviation at different timepoints following microbubble extraction from its vial.

2.4.3 miR-126 Loading Protocol and Characterization

To confirm gene coupling to the outer shell of our cationic microbubbles, a solution of microbubbles was incubated at room temperature for 15 min with a red fluorescent siRNA (Alexa Fluor 555 BLOCK-iT, Thermo Fisher Scientific, Waltham, MA, USA) in a 1:1 proportion. These microbubbles were visualized using an RFP light cube from the EVOS M7000 imaging system (Thermo Fisher Scientific). After confirming the cationic nature of our microbubbles, we aimed to load our gene of interest miR-126 (hsa-miR-126-3p; sequence: UCGUACCGUGAGUAAUAAUGCG); Thermo Fisher Scientific).

To quantify miR-126 loading capacity, the microbubbles were incubated with increasing miR-126 concentrations (miR-126 input) at room temperature for 15 min on a tube revolver rotator. These concentrations were fixed from 1 μg miR-126 per 10^9 microbubbles to 20 μg per 10^9 microbubbles, where 20 μL of a RNA loading dye[197] was added to equal volume of the miR-126 and microbubbles solution, and loaded in a 12.5% (19:1 acrylamide/bis-acrylamide) (Thermo Fisher Scientific) urea PAGE[197]. A control lane where equal amounts of miR-126 was diluted in DEPC-treated diH_2O was also loaded next to each miR-126 concentration tested. We ran the gel at 65 V until separation of bromophenol blue (Sigma) and xylene cyanol (Thermo Fisher Scientific). The gel was stained with a 1:10 000 solution of SybrGreen II RNA gel stain (Thermo Fisher Scientific) in TBE buffer for 15 min. The gel was imaged with on a G:BOX F3 (Syngene, Cambridge, UK), and the bands were analyzed on ImageJ (U.S. National Institutes of Health, Bethesda , MD, USA). We assumed that the bands observed corresponded to the unbound miR-

126 (when loaded with microbubbles) and were compared to the control bands (miR-126 with diH_2O), which resulted in the percentage of free miR-126 in the gel.

$$\%\, free = \frac{band\ intensity\ value\ of\ miR-126\ with\ microbubbles}{band\ intensity\ value\ of\ miR-126\ in\ diH_2O} \tag{2.1}$$

Lastly, the percentage of miR-126 bound was obtained with the following equation:

$$\%\, bound = \%100 - \%free \tag{2.2}$$

where we report here the mass of loaded miR-126 as:

$$mass\ of\ bound\ miR-126 = \%bound\ \times mass\ of\ miR-126\ input \tag{3.3}$$

These data points were plotted to find the plateau to determine the maximum achievable mass of bound miR-126 per 10^9 microbubbles.

2.4.4 Cell Culture

Primary human umbilical vein endothelial cells (HUVEC; No. C2519A, Lonza, Basel, Switzerland) were cultured in medium (EGM-2, No. C3162, Lonza) and incubated at 37°C and 5% CO_2. For experiments, the cells were harvested with a 0.05% solution of trypsin-EDTA (Wisent, QC, Canada) at 90% confluency and placed in a suspension within cell culture medium at a concentration of 500,000 cells per ml. All experiments were performed on HUVECs characterized by a passage number between 3 and 10.

2.4.5 Ultrasound Apparatus and Experimental Procedure

We employed a custom-designed ultrasound treatment tank in order to assess microbubble-mediated miR-126 delivery to endothelial cells (Figure 2.1). The treatment tank was a 30L plastic container filled with 15L of gas-equilibrated diH_2O, enough volume to submerge both the transducers, but kept below the opening of the sample chamber. The water temperature was

maintained at 37°C using an immersion heater circulator (VWR model 1120, Radnor, PA, USA). The tank consisted of a sample chamber and two co-aligned single-element transducers. A magnetic stir bar was placed inside the sample chamber, which is made of acrylic and sealed with mylar windows (25 μm thickness) to allow for ultrasound transmission. The unit was placed on a magnetic stir plate. Samples were prepared by incubating miR-126-loaded microbubbles with HUVECs at a fixed ratio of 50 bubbles per cell. Placed within our warmed sample chamber, this cocktail was constantly mixed using a magnetic stir bar to ensure homogeneous distribution of the microbubbles and cells. After a 1 min wait to ensure equilibrium, the sample was treated with ultrasound.

The treatment transducer (1 MHz, f = 25.4 mm, f# = 1.33) was driven at 1 MHz with 1000 cycles, varying pulse repetition intervals from 2.5–5 ms (duty cycles (DC) of 20–40%) at a peak negative pressure of 52 kPa generated from an arbitrary function generator (AFG31000, Tektronix, Beaverton, OR, USA) and amplified using a radio frequency (RF) power amplifier (model 105A100B, Amplifier Research, Souderton, PA, USA) for a treatment duration of 2 min. The acoustic pressure was measured in free space within a separate water tank using a 'bullet' hydrophone (HGL-0200, ONDA, Sunnyvale, CA, USA). The second transducer (3.5 MHz flat transducer, Olympus) was used as a passive cavitation detector to record microbubble scattering, specifically, to assess the presence of stable and inertial cavitation. Receive echoes were amplified (AU-1579, 0.7–200 MHz, MITEQ, Hauppauge, NY, USA), bandpass-filtered, and then digitized (Gage Razor Express CompuScope, Lock-port, IL, USA) for offline analysis using custom MATLAB software (Mathworks, Natick, MA, USA). The frequency-dependent transfer function of this receive circuit was not determined; thus, all measurements are relative. Joint time–

frequency analysis was performed with a window size of 50 ms and a 90% overlap. A Hamming window was applied to the RF data prior to obtaining the fast Fourier transform (FFT).

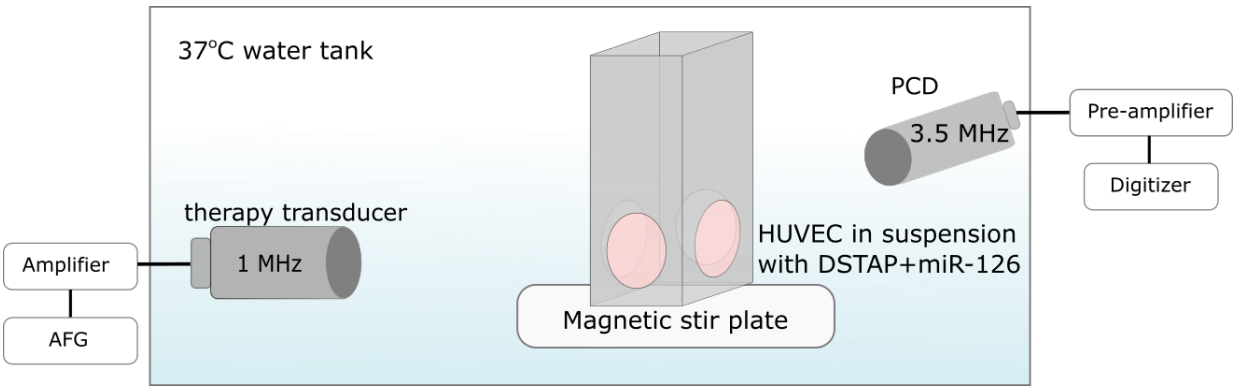

Figure 2.1: Experimental setup equipped with two co-aligned transducers for ultrasound-mediated gene delivery to endothelial cells. The therapy transducer (1 MHz) focuses within a cell suspension chamber, while the second transducer (3.5 MHz) is used for passive detection of microbubble echoes.

Following ultrasound treatment, the cells were transferred from the custom-designed suspension chamber to a conical tube left at room temperature for 5 min to allow for sonoporation recovery. These cells were then placed on ice until all the samples were treated before washing three times at 220×g for 5 min at 4°C per wash to remove the remaining microbubbles. The sham controls were handled similarly without ultrasound.

2.4.6 RT-qPCR

Immediately following the washes, the total RNA content of the cells was extracted using a mirVana™ miRNA isolation kit (Invitrogen), and 10 ng RNA samples were used for PCR. The primers were all purchased from Thermo Fisher Scientific, and, although their sequences are proprietary information, their product numbers (PN) are listed. The PCR primers used to generate cDNA were U6 (PN: 4440887 RT 001973) and hsa-miR-126 (PN 4427975 39G01 RT 002228) on a thermal cycler (Applied Biosystems, Waltham, MA, USA) set at 16 °C for 30 min, 42 °C for 30 min, and 85 °C for 5 min. RT-qPCR was performed using TaqMan™ Fast Advanced Master Mix

no UNG (Thermo Fisher Scientific) on a QuantStudio™ 3 (Thermo Fisher) set at 95 °C for 20 s, then 40 cycles of 95 °C (1 s) to 60 °C (20 s). The primers used for RT-qPCR were U6 (PN: 4440887 TM 001973) and miR-126 (PN: 4440887 74A03 TM 002228). Relative miR-126 levels were calculated using the $2^{(-\Delta\Delta Ct)}$ method using U6 as the housekeeping control.

2.4.7 Viability Assay

Endothelial cell viability was measured after 2 days and 4 days, whereby 20,000 and 10,000 cells, respectively, were seeded on 96-well dishes in triplicate. After washing the cells with PBS three times, MTT (3-(4,5-dimethylthazolk-2-yl)-2,5-diphenyl tetrazolium bromide) reagent (Sigma) was added as per the manufacturer's protocol. The absorbance was measured on a Varioskan™ LUX microplate reader (Thermo Fisher Scientific) at 540 nm after a 4h incubation in 37°C in 5% CO_2 and solubilizing the formazan with DMSO (BioRad, Hercules, CA, USA) for 10 min. Viability was assessed relative to sham controls.

2.4.8 Western Blotting

Following the washes after ultrasound treatments, cells were seeded on six-well dishes and harvested 2 days later. Total protein was extracted using RIPA lysis buffer (Alfa Aesar, Haverhill, MA, USA), and 20–30 µg of protein was loaded per lane in a 7.5% acrylamide (37.5:1 acrylamide/bis-acrylamide) (BioRad) SDS-PAGE, 1.5 mm thick. We let the gel run at 70 V for 30 min and 100 V until complete separation of the PageRuler™ Plus prestained protein ladder (Thermo Fisher Scientific). The proteins were transferred on a PVDF membrane overnight in Towbin buffer at 4°C. The membrane was stained with 0.5% Ponceau S (Sigma) in 1% glacial acetic acid for 5 min to ensure proper protein transfer and destained with TBS. Following blocking in TBS with 5% BSA (Wisent) for 1 h at room temperature, the PVDF membrane was cut in three sections horizontally to separate the target proteins according to their molecular weights.

The antibodies used for blotting were monoclonal anti-SPRED1 (Santa Cruz Biotechnology, Dallas, TX, USA), monoclonal anti-PI-3-kinase p85β (PIK3R2, Santa Cruz Biotechnology), and anti-GAPDH (Invitrogen), diluted in TBST-2% BSA for 1 h at room temperature. The first section was cut at the 70 kDa band to probe for PIK3R2. The second section was cut around the 40 kDa band (between the 35 kDa and 55 kDa bands) to probe for SPRED1. The last section was used to probe for GAPDH. When we could not obtain a satisfactory separation from ladder to cut the membrane between the 55 kDa and 35 kDa bands, the membrane was only cut at the 70 kDa band. GAPDH was then probed first, stripped with a mild stripping buffer (Abcam) for 5 min, and washed with PBS and TBS for 5–10 min twice each. Blocking could then be repeated on this half membrane to probe SPRED1. The membrane was then incubated in with goat anti-mouse IgG (H + L) HRP (Invitrogen) secondary antibody diluted in TBST-2% BSA for 1h at room temperature. PVDF blotted membranes were labeled with Pierce ECL Western Blotting Substrate (Thermo Fisher Scientific) prior to imaging on an Amersham Imager 600 (GE Healthcare, Chicago, IL, USA). Bands were analyzed in ImageJ.

2.4.9 Endothelial Tube Formation Assay

A growth factor-reduced Matrigel® matrix basement membrane (Corning, NY, USA) was prepared on a 96-well dish according to the manufacturer's protocol. Following the washes, 2000 cells were seeded atop the Matrigel for 16 h. HUVECs were then stained with Calcein-AM (Thermo Fisher) at 1 μg/mL and visualized on an epi-fluorescence microscope at 488 nm (EVOS system, Life Technologies). Angiogenesis quantification was assessed by AutoTube[198–200] on MATLAB (Mathworks).

2.5 Results

2.5.1 Characterization of DSTAP Microbubbles and miR-126 Loading

The microbubble size distribution is shown in Figure 2.2A, depicting a polydisperse population with a peak volume-weighted diameter of 3.56 ± 0.32 µm. Stability tests, where measurements were taken every 20 min, suggest nonsignificant (p-value = 0.313, n = 3) changes in microbubble diameter and concentration ($1.01 \times 10^9 \pm 0.31 \times 10^9$ microbubbles/mL) over 80 min (Figure 2.2B). The size and concentration information reported here is consistent with clinically employed agents[201–203].

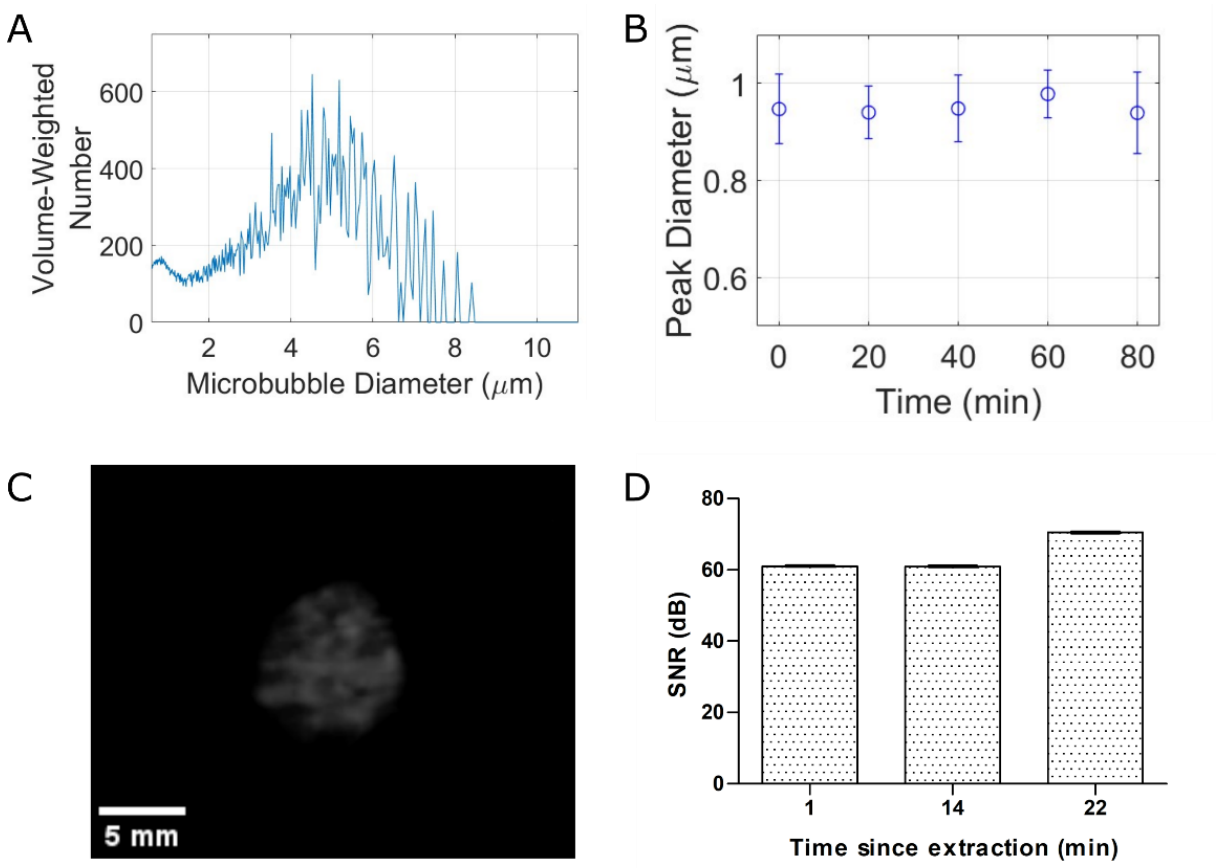

Figure 2.2: Our stable microbubble formulation can be used for clinical contrast imaging. (A) Volume-weighted size distribution with a concentration of (1.01±0.31) × 109 microbubbles/mL. (B) Stability over 80 min. (C) Nonlinear contrast imaging of microbubbles in wall-less tissue phantom. (D) SNR analysis of contrast signal over 22 min post-agent extraction.

Clinical contrast echo from the agent—which is indicative of nonlinear scattering of the microbubbles—is shown qualitatively in Figure 2.2C and quantified in Figure 2.2D. The large contrast signal-to-noise ratio of the agent remains relatively constant up to 22 min following agent extraction from the sealed vial (62.95 ± 2.56 to 70.24 ± 2.76 dB). These data, along with the concentration and stability properties, suggest its viability as a clinical agent.

In order to test the cationic nature of this in-house agent, as well as to provide evidence for gene coupling along the surface of the microbubbles, Figure 2.3A highlights the surface distribution of a surrogate fluorescence siRNA. It can be seen from this micrograph that the fluorescent nucleic acid conforms to the outer surface (*i.e.*, the shell) of the microbubbles. Furthermore, the cationic nature of our agent was confirmed via assessment of the surface charge, which was determined to be +38.04 mV pre-miR loading, decreasing to +27.60 mV post miR loading (Figure 2.3B; $p < 0.0002$). To quantify this miR-126 carrying capacity, gel electrophoresis was performed to compare the amount of free-miR-126 in diH_2O compared to unbound miR-126 from microbubbles at varying quantities of miR-126 (Figure 2.3C). Binding capacity was determined from plotting a saturation curve (red) and the value at which the curve plateaus is defined as the binding capacity. For our formulation, we determined a loading capacity of 6 μg of miR-126 per 10^9 microbubbles (Figure 2.3D), which is what we used for all subsequent experiments.

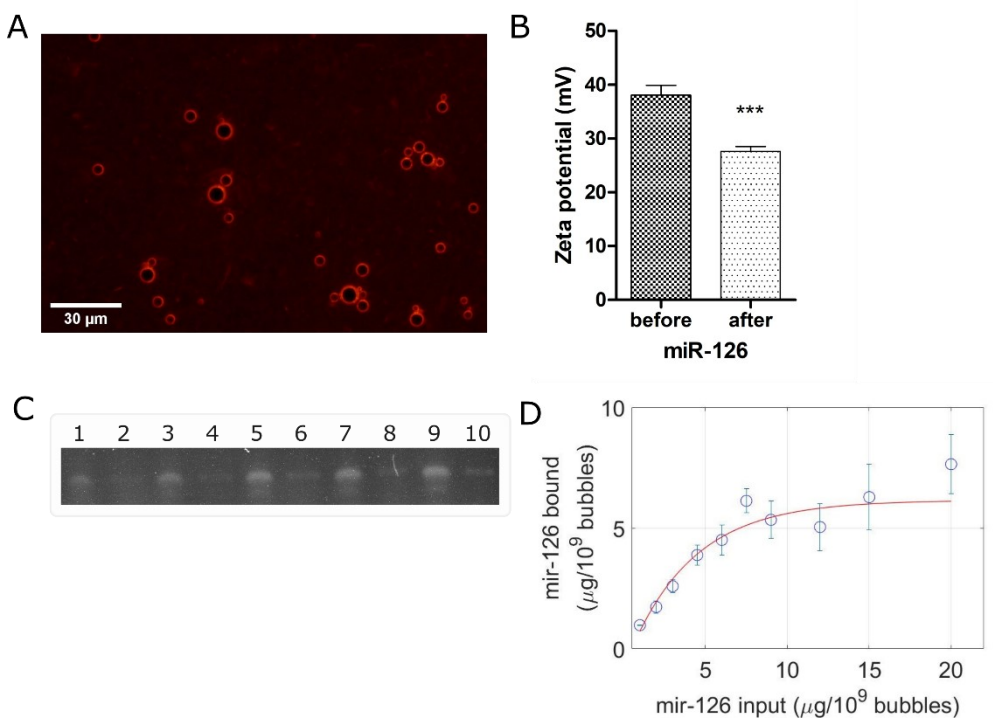

Figure 2.3: Gene coupling characterization results in 6 µg of miR-126 per 10^9 microbubbles. (A) Fluorescent siRNA localization on microbubble surface. Scale bar: 30 µm. (B) Surface charge before and after coupling of 6 µg of miR-126 per 10^9 microbubbles. (C) Acrylamide/urea PAGE of miR-126 binding capacity on DSTAP: odd-numbered lanes show free miR-126 (1 to 20 µg) in DEPC H_2O and even-numbered lanes show corresponding unbound miR-126 after incubation with DSTAP. (D) Quantification of miR-126 binding capacity on DSTAP. (***: $p < 0.001$).

2.5.2 Ultrasound-Mediated miR Delivery Using miR-126-Conjugated DSTAP Microbubbles

Ultrasound-assisted viable miR-126 delivery to endothelial cells via stable cavitation was demonstrated in Figure 2.4. Figure 2.4A indicates a gradual increase in miR-126 levels, from 1.482 to 2.326 relative to the sham control, with increasing duty cycle (n = 3 to 8, *p*-values = 0.004, 0.02, 0.08, respectively). Our data indicate that, under this ultrasound treatment regimen, endothelial cell viability is maintained (>95%) (Figure 2.4B; n = 6 to 24, *p*-value non-significant). Further, as confirmation of functional delivery, we assayed the protein levels of miR-126 target proteins SPRED1 and PIK3R2 (Figure 2.4C). These were downregulated 2 days following gene delivery; we observed a 4% to 33% decrease in SPRED1 with increasing duty cycle (n = 3 to 4; *p*-value =

0.0345 at duty cycle of 40%), while PIK3R2 decreased from 36% to 46% with increasing duty cycle (Figure 2.4D; n = 4; *p*-values = 0.02, 0.008, and 0.003, respectively).

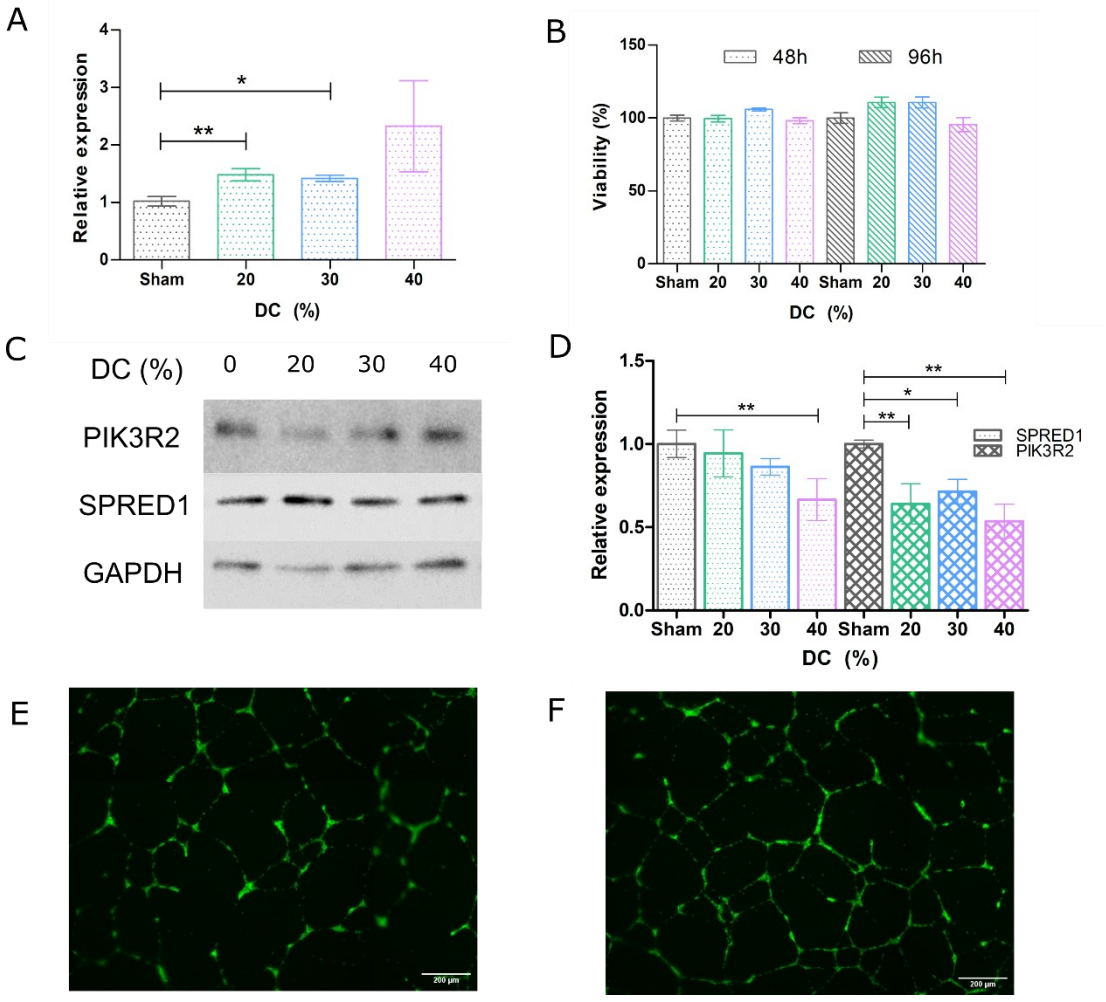

Figure 2.4: Ultrasound-mediated miR-126 delivery results in viable physiologically relevant treatment of endothelial cells. (A) RT-qPCR analysis of the relative miR-126 expression from treated HUVECs. (B) Viability assessment of the cells 48 h and 96 h following ultrasound treatment by MTT assay. (C) PIK3R2 and SPRED1 protein expression in treated HUVECs determined by Western blotting. (D) Aggregate relative PIK3R2 and SPRED1 expression 48 h following HUVEC treatment. (E) HUVEC tube formation assay, untreated and (F) treated at 20% DC. In aggregate, the tube network increased by 2–21% and exhibited a 2–28% increase in branching nodes. Scale bar: 200 µm. (*: $p<0.05$, **: $p<0.01$). Grey: sham, green: 20% DC, blue: 30% DC, magenta: 40% DC.

A second subset of treated cells were used to grow on Matrigel® basement membrane matrix, where endothelial tube formation was assessed 16h after seeding. As can be seen in the

representative images shown in Figures 2.4E,F, tubule networks were significantly more complex in miR-126-treated endothelial cells compared to sham control (Figure 2.4E). Specifically, tube network increased by 22–26% and exhibited a 5–17% increase in branching nodes (Figure 5.1).

2.5.3 Passive Cavitation Detection

To confirm stable microbubble activity during treatment, the gene delivery setup (Figure 2.1) was concurrently equipped with a passive cavitation detection transducer. Figure 2.5A shows a representative example of the frequency spectrum at the beginning of the 2 min treatment with microbubbles (30% duty cycle; black) overlaid with pure PBS (blue). It can be clearly seen that, under this acoustic regime, microbubbles underwent stable cavitation, as confirmed by narrowband signal power peaking at second, third, and fourth harmonics (2, 3, and 4 MHz) and an absence of broadband emissions. Furthermore, time–frequency analysis (Figure 2.5B,C) confirmed that microbubbles were undergoing stable cavitation throughout the entire duration of the ultrasound treatment. Figure 2.5D depicts the cumulative spectral power from the stable (blue, solid line) versus inertial (black, dashed line) cavitation frequency bands for a given sample. Figure 2.5E quantifies the total integrated power for microbubble samples and PBS control, highlighting the virtual absence of inertial cavitation and a statistically significant 13.5 dB in stable cavitation activity ($p < 0.02$).

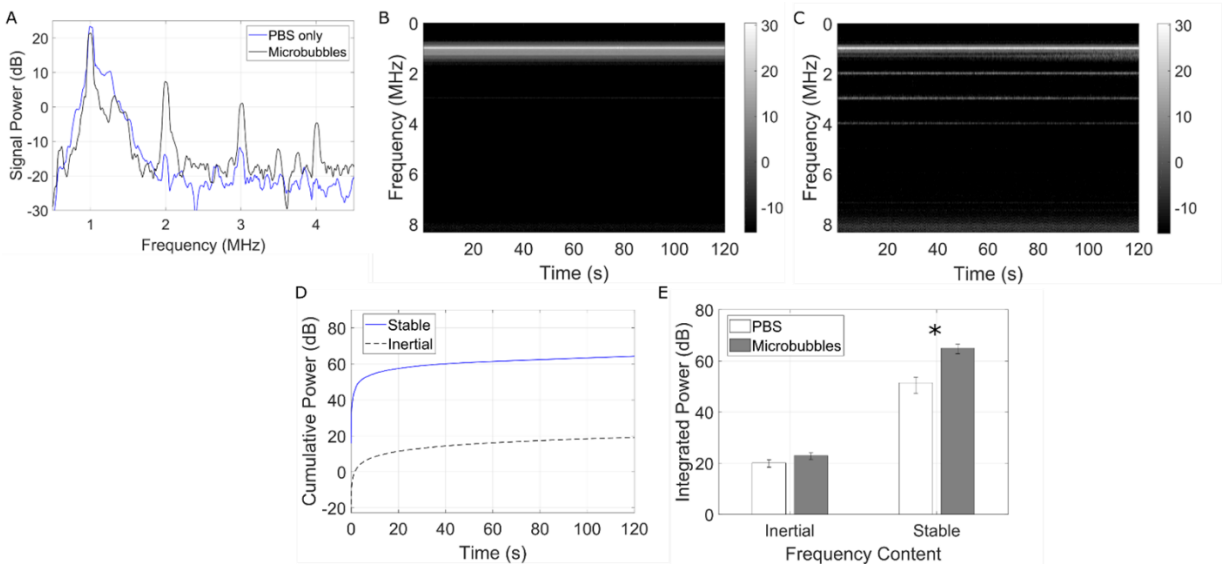

Figure 2.5: Microbubbles undergo stable cavitation during gene delivery treatment. (A) The microbubble echo spectrum at the beginning of treatment (black line) as compared to a PBS only control (blue line). (B) Time–frequency plots of the resulting cavitation echoes in PBS (control) and (C) miR−126 loaded microbubbles. This time–frequency depiction clearly shows prolonged harmonic content (stable cavitation) throughout the 2 min treatment, and the absence of any broadband spectral emissions (inertial cavitation). (D) Quantification of the cumulative spectral power from the stable (blue, solid line) and inertial (black, dashed line) cavitation frequency bands over the total treatment time of a given sample. (E) Quantification over all samples compared to PBS only controls. Asterisks denote statistical significance (*: $p < 0.02$).

2.6 Discussion

In this study, we developed a methodology to deliver modest amounts of miR-126 onto endothelial cells for the purpose of therapeutic angiogenesis. Our results demonstrate that miR-126 can be successfully delivered intercellularly via ultrasound and microbubbles in sufficient quantities to elicit downstream regulation of target proteins and a viable physiological response.

It is perhaps worth noting that one of the limitations of the present study is that the endothelial cells were treated in suspension, as opposed to within the more biologically relevant monolayer configuration. This could have negatively affected transfection efficiency because the cell morphology of these cells in suspension exhibited less surface area as opposed to their adherent morphology and, incidentally, were less likely to interact with a miR-126-decorated

microbubble in the cell chamber. To address this in future work, another nonadherent cell lines could be investigated, such as endothelial progenitor cells[204], or cells could be cultivated and treated under fluidic conditions more accurate mimic a vessel[205]. This arrangement, however, was chosen in order to position two co-aligned transducers in such a way as to be able to passively record the acoustic emissions during treatment (Figure 2.5). This is essential as it provides evidence of microbubble stable cavitation. Due to the specific ultrasound parameters employed (*e.g.*, long pulses), this would have been challenging to conduct using a single transducer with active listening (pulse-echo).

Indeed, while designing the ultrasound regimen, we focused on maintaining cellular viability albeit at the expense of lower transfection efficiency in order to substantiate the feasibility of microbubble-mediated gene delivery as opposed to other gene delivery methods. For instance, in peptide-mediated miR-126 delivery to vascular endothelial cells, Zhou and colleagues reached a 3.5-fold increase in miR-126 but reported cell death up to 20% at the highest peptide dose[206]. Indeed, by devising a microbubble-mediated miR-126 delivery treatment scheme that minimizes cell death, this enables the potential for repeat treatments to further increase the transfection efficiency and enhance the effects of the genetic payload[35,207].

Microbubble-mediated gene therapy, whether employing miRs or other nucleic acid payloads, has been demonstrated in cancer and cardiovascular applications through cavitation regimes in which the bubbles undergo disruption (*e.g.*, ultrasound-targeted microbubble disruption; UTMD[42]). Violent microbubble collapse initiated this way requires strong acoustic forcing conditions, typically large peak-negative pressures[186]. While this technique has shown promising results in gene deposition within the target tissue[208–210], the bubble involution process can initiate high-speed liquid jets along with other cavitation-based phenomena that may lead to

localized endothelial bio-effects. Endothelial cell damage and denudation have been reported in both microvessels[211] and larger vasculature[212], events which have been correlated to excessive inertial cavitation doses[211] (a surrogate measure of inertial cavitation and microbubble disruption[186]). Further, microvascular hemorrhage and red blood cell extravasation associated with violent microbubble collapse have also been observed[213–216], and recent reports have demonstrated the potential for inertial cavitation to trigger endothelial apoptosis pathways[217]. As a consequence, our treatment paradigm consists of a very low peak negative pressure and large number of cycles, so as to encourage miR payload release from the cationic microbubble surface by stable cavitation—similar in principle to other drug-loaded microbubbles[218]. Indeed, as gene delivery was achieved in the absence of broadband emissions and via these long duration pulses, our results suggest that sustained gentle microbubble vibrations, radiation forces, and agitation lead to delivery of miR-126, a combination that was persistent throughout the 2 min treatment time (see Figure 2.5). The hypothesized drug delivery mechanism here is two-stage. Firstly, long pulse-driven microbubbles can initiate prolonged lipid and cargo release as compared to those driven by shorter pulses at a given pressure amplitude[219]. Secondly, microbubble translation and constant agitation decrease the average microbubble–cell distance, which both aids in microbubble-mediated cell membrane perforation[26] and lowers the distance over which the free miR mimic is required to diffuse to enter the neighboring cell. It is also of interest to note that ultrasound has been shown to modulate endocytosis activity[220,221]; however given the timescales of the miR-delivery performed here, it is perhaps not likely to be the dominant mechanism[222].

2.7 Conclusions

We synthesized a miR-126-bearing microbubble agent with a gene loading capacity of 6 μg per 10^9 microbubbles, characterized by a microbubble concentration, size distribution, and

stability similar to that of currently used clinical agents. Using a low-pressure, long-pulse acoustic regime, we were able to show delivery of up to 2.3-times in miR-126 to endothelial cells compared to sham controls while maintaining cell viability, resulting in the expected physiological behavior, including downregulation of angiogenic suppressor proteins SPRED1 and PIK3R2. Furthermore, simultaneous passive cavitation detection confirms that this was a stable cavitation treatment, thus minimizing potential damage caused by more violent, inertial cavitation approaches.

Chapter 3: Flow Velocity Modulates Vascular Delivery of microRNA-126 Using Focused Ultrasound and Microbubbles

Manuscript under review: He, S., Singh, D., & Helfield, B. (2024). Flow Velocities Modulates Vascular Delivery of microRNA-126 Using Focused Ultrasound and Microbubbles. *Molecular Therapy Nucleic Acids*.

3.1 Foreword

While the potential of focused ultrasound in gene delivery has been demonstrated in *in vitro* systems in the previous chapter, the following one explores this gene delivery process in a pressurized mesenteric artery under intralumenal flow. This model allows us to study the effect of different flow velocities, as well as the layers beyond the endothelium, that may have on the therapeutic efficiency of gene delivery of miR-126. In the next chapter, I describe how I developed a viable methodology to demonstrate ultrasound-mediated permeabilization within a vasoactive *ex vivo* model.

3.2 Abstract

Gene therapy targeting ischemic heart disease is a promising therapeutic avenue but is mostly restricted to viral-based delivery approaches – limited due to off-target immunological responses. Focused ultrasound presents a non-viral, image-guided technique in which circulating intravascular microbubble contrast agents can reversibly enhance vascular permeability and gene penetration. Here, we explore the influence of flow velocity on the microbubble-assisted delivery of miR-126, a potent pro-angiogenic biologic, using a custom acoustically-coupled pressurized mesenteric artery model. We demonstrate that under the same ultrasound conditions, increased flow velocities enhance microbubble-mediated cell permeability - yet miR-126 delivery itself

exhibits a negative correlation with increasing flow velocity. Post-ultrasound assays confirmed vessel vasoreactivity, maintaining vasoconstriction and vasodilation capacities. These findings underscore the critical role microbubble flow velocities play in focused ultrasound gene therapy, especially notable for applications in which blood velocity itself is a salient pathophysiological indicator of disease progression, including ischemia.

3.3 Introduction

Despite ongoing advancements in specialized surgeries and pharmacotherapies[79], ischemia and related cardiovascular diseases remain the leading causes of mortality[223]. One promising alternative to traditional surgical interventions is gene therapy, which involves delivering genetic material directly to diseased tissues to induce therapeutic effects[224]. In this context, one of the most promising genetic therapeutics is microRNA-126 (miR-126), the administration of which has been shown to promote angiogenesis[80,225]. However, despite the promise of miR-126 therapy, the lack of a safe and effective delivery method remains a significant challenge. Common strategies rely on viral vectors, which, while effective, carry the risk of eliciting dose-limiting immune responses and potential long-term safety concerns[226].

Focused ultrasound and microbubbles have been extensively investigated as an alternative, non-viral approach to targeted gene delivery, addressing many of the limitations associated with other types of vectors. Microbubbles are small, gas-filled bubbles encapsulated often within a lipid shell. They remain entirely intravascular due to their size (1-8 μm in diameter) and are traditionally used as contrast agents in clinical imaging, particularly in cardiology[227]. When exposed to ultrasound, these microbubbles oscillate and scatter nonlinear ultrasound energy that can be harnessed for contrast[228]. However, under specific acoustic conditions, they can be made to generate mechanical forces that temporarily increase the permeability of neighboring vasculature

and cellular membranes[115,229–231]. This transient increase in permeability allows for the delivery of therapeutic agents that would otherwise be impermeable and remain intravascular – a technique that has made recent and significant success in targeted blood-brain-barrier permeation in the context of neurology and neuro-oncology[39,232], and is rapidly expanding in the cardiovascular disease arena[233].

The extent to which ultrasound-mediated microbubble vibrations permeate the surrounding vasculature, and the salient factors that affect its efficiency as a targeted therapeutic tool, is an expanding area of research. Chief among these conditions is the microbubble flow velocities, which has been recently shown to influence ultrasound-assisted endothelial cell membrane permeability enhancement[234] due, in part, to the local number density of bubbles passing through the acoustic beam per unit time and area and the flow-regulated endothelial secretome[235]. Indeed, in the context of microbubble-assisted drug/ gene delivery, there is a paucity of information with respect to the relationship between flow velocity and enhanced drug/gene uptake. Notably, this is a critical parameter in the context of vascular stenosis, angiogenesis, arteriogenesis, and ischemia – where flow velocity is expected to be modulated based on the extent and time-course of disease[77,236].

Here, we aim to explore how flow velocity influences microbubble-assisted permeability and vascular delivery of pro-angiogenic miR-126 within a pressurized mesenteric artery model. With the development of this model, we are able to additionally monitor vessel vasoactivity and vessel viability both before and after ultrasound exposure. First, after confirming viable vessel isolation, we assess the effect of increasing flow velocity on microbubble-mediated cell permeability. We follow this with a subset of parallel experiments for the delivery of miR-126

under a range of acoustic conditions, and finally we discuss our results within the broader context of focused ultrasound therapy.

3.4 Materials and methods

3.4.1 Mesentery isolation

All animal experiments were approved by the Animal Research Ethics Committee at Concordia University. Healthy male and female Sprague-Dawley rats were purchased from Charles River Laboratories (Senneville, Canada). They were housed in a controlled environment with a 12-hour light-dark cycle, provided with corncob bedding and shredded Enviro-Dri, and given unrestricted access to food. Euthanasia was conducted on rats aged between 6 weeks and up to a year using a combination of isoflurane anesthesia and CO_2 asphyxiation. Upon confirming cessation of vital signs, euthanasia was further confirmed by exsanguination or cervical dislocation, as per the ethical guidelines set forth by Concordia University. The mesenteric bed was then carefully excised and transferred to a petri dish (Figure 3.1A) containing cold Krebs-Hepes buffer (118.4 mM NaCl, 4.7 mM KCl, 1.2 mM $MgSO_4$, 4mM $NaHCO_3$, 10 mM Hepes, 6mM glucose, 1.2 mM KH_2PO_4, and 2 mM $CaCl_2$ fixed at pH 7.4 with NaOH). Vessels were then cleaned of the surrounding fat tissue and stored up to 9 hours for further experimentation.

3.4.2 Pressure myograph

Third-order mesenteric arteries were isolated and mounted on 100-125 μm borosilicate cannula within a pressure myograph setup (CH-1-LIN Linear Vessel Chamber, Living Systems Instrumentation, Vermont, USA) and attached by two nylon treads on each side of the vessel (Figure 3.1B). Krebs-Hepes buffer was used to flush out the intralumenal blood. The pressurization process started at 30 mmHg for 30 minutes and increased to 60 mmHg for another 30 minutes. Each pressure was controlled by a Servo pump (PS-200-P, Living Systems Instrumentation) and

set by a Pressure Servo Controller (PS-200S, Living Systems Instrumentation). The mounted vessel remained positioned above a glass coverslip and submerged in a continuously circulating bath Krebs-Hepes buffer maintained at 37°C (Reglo Peristaltic Pump, Ismatec, Glattbrugg, Switzerland). Vessels were all maintained at 60 mmHg, an estimate of their *in vivo* pressure [237].

3.4.3 Vasoreactivity assay

The pressure myograph was placed on a Leica (DM, Germany) inverted microscope at a 4X magnification to record vessel diameter with a Basler Ace 2 camera (Basler, Ahrensburg, Germany). For vessel reactivity experiments, we conducted standard vasoconstriction and vasodilation assays. All buffers were made the same day of experiments. First, we added increasing concentrations of phenylephrine (Phe; Sigma-Aldrich, St-Louis, USA) ranging from 10^{-7}, 5×10^{-7}, 10^{-6}, 10^{-5} M, with each concentration exposed for 5 minutes. Phenylephrine is an α-adrenergic agonist which is known to cause contraction of vascular smooth muscle by increasing the concentration of available Ca^{2+} to increase the activity of actin and myosin[238]. Vessel diameters were analyzed offline using in-house MATLAB (Mathworks, Natick, USA) software and maximum constriction was determined as follows:

$$max\ constriction = \frac{diameter\ at\ 10^{-5}M\ phenylephrine}{\max diameter} \times 100\% \qquad (3.1)$$

where the *max diameter* is the highest diameter achieved throughout the recording process. Phenylephrine was then removed to restore the vessel to its equilibrium, pressured diameter.

To assess whether the endothelium is intact and functional, we further employed acetylcholine (Ach; Sigma-Aldrich at 10^{-4} M) as an endothelium-dependent vasodilator which tests the vasodilator response of the vessel (mediated by the release of nitric oxide). Under the largest

Phe vasoconstriction, Ach was then added to the buffer and the vessel diameter was recorded for a minimum of 5 minutes. The percentage dilation was calculated using the formula:

$$\%\ dilation = \frac{dilated\ diameter - constricted\ diameter}{\max diameter - constricted\ diameter} \times 100\% \qquad (3.2)$$

where the *dilated diameter* is the diameter of the vessel reached after incubating in acetylcholine buffer for 5 minutes and the *constricted diameter* corresponds to the diameter achieved after incubating in 10^{-5} M phenylephrine buffer for 5 minutes.

3.4.4 Microbubble-mediated focused ultrasound cell permeabilization

For the ultrasound experiments (Figure 3.1C), 20 µl of Definity® microbubbles (10% v/v; Lantheus Medical Imaging, N. Billerica, USA) was injected into the tubing proximal to the pressurized vessel and the flow velocities were controlled by a peristaltic pump (P720 pump, Instech, Plymouth Meeting, PA, USA). Definity® is clinically used worldwide as a diagnostic contrast agent[239], and the microbubble concentration and size distribution are well characterized[240]. After agent activation, microbubbles were left to equilibrate to room temperature in order to obtain a reproducible bubble distribution[196], as per manufacturer's instructions. The flow velocities were maintained from 0.83, 1.47 to 1.89 cm/s, based on the assumption of a maximum (*i.e.* native) average intralumenal diameter of (391±35) µm (n=10). These flow velocities are consistent with shear rates of similar vessels[241]. The vessels were exposed to a focused, single-element 2.25 MHz transducer (IL0208GP, Valpey Fisher, Hopkinton, VA, USA), which was coupled with a 5 mm layer of ultrasound transmission gel (Aquasonic 100, Parker Laboratories, Farfied, NJ, USA) beneath the glass coverslip of the myograph (Figure 3.1C). The peak negative acoustic pressure was set to 325 kPa (and thus a mechanical index of ~0.22), as measured separately in a gas-equilibrated water-tank using a hydrophone (HGL-200, Onda, Sunnyvale, CA, USA). Ultrasound

delivery was performed using a pulse repetition interval of 1 ms, and either 250, 500 or 1000 cycles (corresponding to duty cycles [DC] of 11.1%, 22.2% or 44.4% respectively) with a 5s total treatment duration, as depicted in Figure. 3.1D. The ultrasound was generated by an arbitrary waveform generator (AFG31000, Tektronix, Beaverton, OR, USA) and amplified through an RF power amplifier (model 105A100B, Amplifier Research, Souderton, AR, USA).

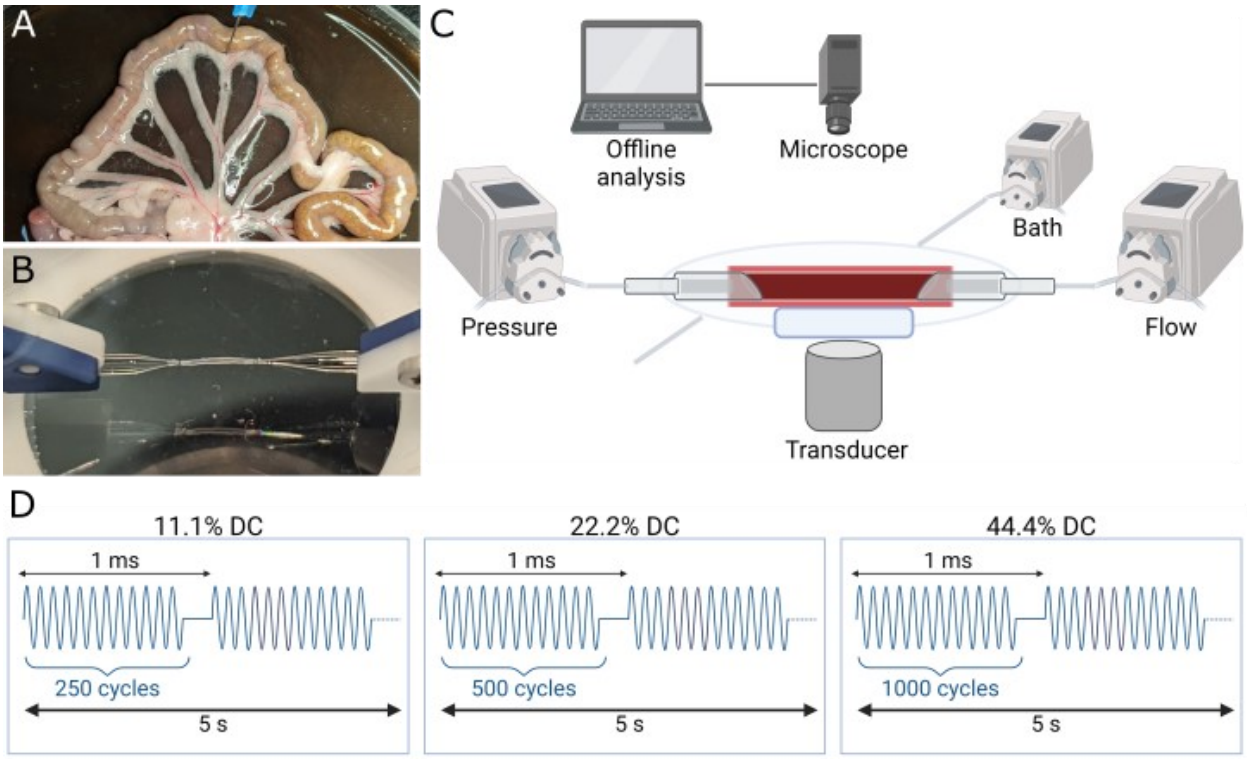

Figure 3.1: Experimental setup. (A) Mesentery bed isolated from Sprague-Dawley rats. (B) Mesenteric artery cannulated on the pressure myograph. (C) Simplified schematic of the ultrasound treatment setup: left "Pressure" pump maintains the intralumenal pressure to 60 mmHg, "Bath" pump continuously circulates Krebs-Hepes buffer heated at to 37°C, "Flow" pump controls the intralumenal flow velocity, the pressure myograph sits on a Leica inverted microscope connected to a Baser camera which records the vessel images and sends them to a computer for offline analysis. For ultrasound treatments, a layer of ultrasound gel was applied to the 2.25 MHz transducer and was placed underneath the pressure myograph, focusing on the vessel through a glass coverslip. (D) Pulse sequence of the ultrasound parameters used: frequency was set at 2.25 MHz, the pulse repetition interval was set at 1 ms, with a peak negative pressure measured at 325 kPa. For duty cycles of 11.1%, 22.2% and 44.4%, there were 250, 500 or 1000 cycles employed, respectively.

3.4.5 Flow-dependent ultrasound-assisted membrane permeability assay

To quantify cell membrane permeability, we employed 150 nM of propidium iodide (PI, Sigma-Aldrich) in the circulating Krebs-Hepes bath. This is a non-fluorescent, cell-impermeant compound that exhibits a significant increase in fluorescence upon binding to RNA/DNA complexes (535/617nm) – and thus reports measurable signal only within cells with increased membrane permeability. First, the vessels were first incubated with this solution for 5 minutes to assess the background signal level and to exclude any pre-permeabilized cells from further analysis. To achieve this, three to seven frames spanning the length of the vessels were captured at a 10X magnification under epi-fluorescence microscopy (X-Cite, Excelitas Technologies, Waltham, MA, USA). Following the focused ultrasound and microbubble treatment, the same frames were re-acquired and analyzed offline via in-house MATLAB software. This analysis computed the total number of PI-positive (PI+) cells per treatment condition (background-subtracted) and compared it to the control experiments which consisted of ultrasound treatment under flow with no microbubbles present. Data is reported as fold increase over control per flow velocity.

3.4.6 Flow-dependent ultrasound-assisted miR-126 delivery

For the gene delivery assays, 10.25 μg of miR-126 (hsa-miR-126-3p, Thermo Fisher Scientific, Pittsburgh, PA, USA) was added to the microbubble solution and this cocktail was introduced to the lumen of the vessels at the three different flow velocities. Following a 30-minute recovery period (post-ultrasound treatment) under flow conditions, the vessels were carefully flash-frozen in isopentane (Sigma-Aldrich) cooled by liquid nitrogen and transferred to an RNase-free tube for RNA isolation. This recovery period additionally served as a method to ensure no residual miR-126 within the lumen of the vessel. To homogenize the vessel, a lysis buffer (miR-

Vana miRNA isolation kit, Thermo Fisher Scientific) was added to the tube, and an ultrasonic homogenizer (Thermo Fisher) with a 1/8' tip was employed at 40% amplitude, 10 cycles of 1 second on, 5 second off, for a total of 61 seconds. The remaining steps of the miRNA extraction were conducted as per the manufacturer's protocol. Detailed procedures for PCR and RT-qPCR have been previously described[242] with U6 (Thermo Fisher Scientific) as the housekeeping control.

3.4.7 Vasoreactivity post-ultrasound therapy

For a subset of studies, pressurized vessels were left to recover for 30 minutes after ultrasound treatment. The vessels were then subject to the standard vasoactivity assays with phenylephrine-based constriction and acetylcholine-based dilation as described above to confirm that vessel viability was maintained post-ultrasound.

3.4.8 Statistical analyses

Most data were analyzed on GraphPad Prism 5.0 software and were expressed as mean ± SEM. For the vasoreactivity assays, a one-way analysis of variance (ANOVA) was conducted to determine if there were any statistically significant differences between the control (untreated) group and the ultrasound-treated groups. Since there were no statistical differences among the maximum constricted diameters, nor the maximum dilated diameters, no post-hoc tests were performed. For the RT-qPCR data, the error bars were calculated in logarithmic space to account for the exponential nature of the amplification curves. Each datapoint represents at least 3 independent isolated vessels, which were assessed 3 times. To determine the significance of our RT-qPCR, unpaired, two tailed Student's t-tests were performed among all experimental groups with a confidence interval set at 95% ($p<0.05$). As for the PI results, paired, two-tailed Student's t-tests were performed similarly to the RT-qPCR analysis.

3.5 Results

3.5.1 Vessel viability

Our first objective was to confirm that our mesentery isolation and handling (Figure 3.1) yields viable vessels, and to obtain a baseline of their vasoactive response. We performed two assays, phenylephrine-induced vasoconstriction and acetylcholine-induced vasodilation, representative examples of which are shown in Figure. 3.2A-H. The global results are presented in Figure 3.2G-I in which the dilation percentage is reported. Cannulated vessels obtain gradual vasoconstriction reaching 60% dilation by 10^{-5} M phenylephrine *(*$p<2.6\times10^{-6}$ as compared to 0 M) and recover up to >90% ($p<0.003$ as compared to 0 M). These levels of pressured vascular vasoconstriction and subsequent vasorelaxation are consistent with viable arteries reported elsewhere[243,244].

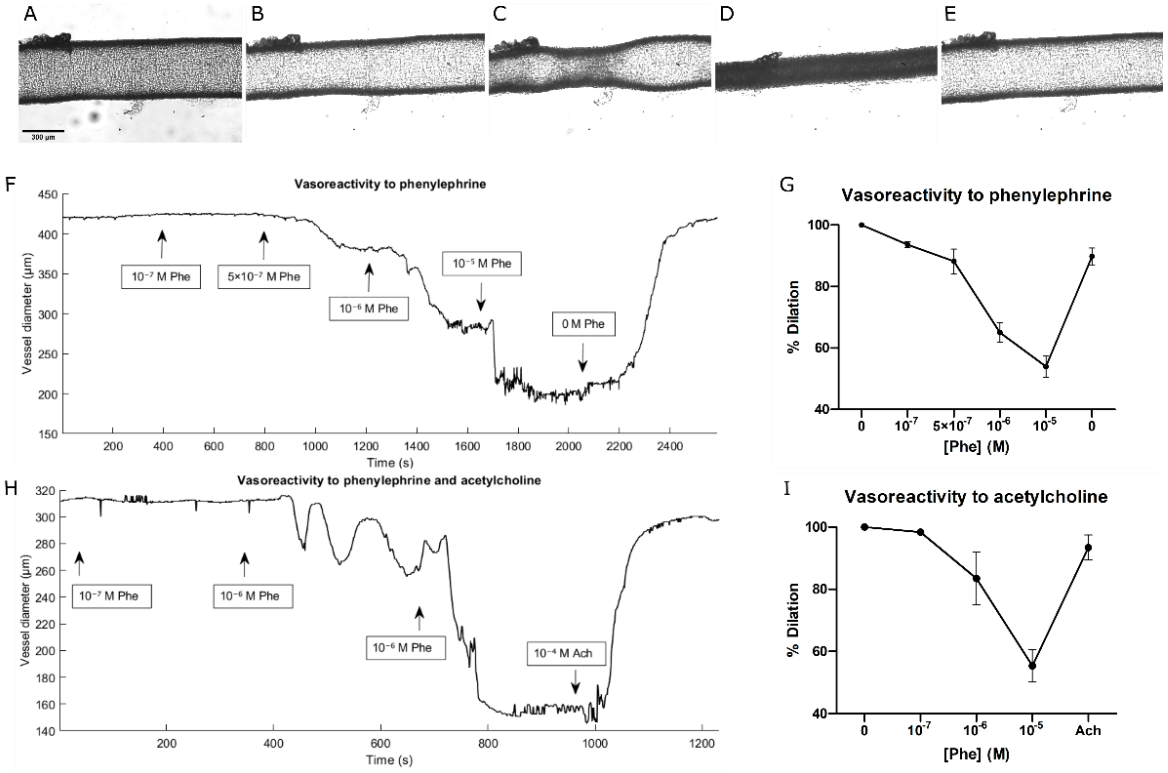

Figure 3.2: Viable extraction of 3rd order rat mesentery arteries. Representative micrographs of a pressured vessel (60 mmHg) responding to cumulative dosing of phenylephrine, from (A) 0 M, (B) 5×10-7 M, (C) 10-6 M, (D) 10-5 M, and back to (E) 0 M. Scale bar = 300 µm. Sample vessel diameter versus time in response to either (F) phenylephrine-indued vasoconstriction alone or in combination with (H) acetylcholine-induced vasodilation and the (G, I) global summary of these vasoactivity assays. Arrows indicate when the doses were applied in (F, H). All data represented as mean ± standard deviation, derived from at least n=3 individual vessels per condition.

3.5.2 Flow-dependent vascular cell membrane permeability

We proceeded to incorporate clinical microbubble contrast agent Definity® and PI, a real-time membrane permeability marker, within the perfusate. After confirmation of intravascular microbubbles (Figure. 3.3A-D) the vessels were treated with ultrasound for 5 seconds (Figure 2E-H, where propidium iodide signal is shown in red). The complete dataset is summarized in Figure 2I-J, where the relative number of PI positive cells as compared to untreated sham controls as a function of flow velocity is depicted under all three ultrasound conditions (11.1%, 22.2% and

44.4% duty cycles). For the lowest acoustic setting (11.1% duty cycle, Figure 3.3I), the number of permeabilized cells increased from 1.89 to 2.39-fold over control from 0.83 -1.89 cm/s flow velocities, exhibiting a statistically significant increase between the slowest and fastest flow condition ($p<0.0286$). When doubling the number of ultrasound cycles (22.2% duty cycle, Figure 3.3J), we observe a similar trend ranging from a 2.64 to 6.01-fold increases compared to flow matched controls ($p<0.0016$). This trend continued at 44.4% duty cycle (Figure 3.3K), where we observed a 1.36 to 5.32 fold increase in PI positive cells with increasing flow velocities ($p<0.0125$). The control (CTL) datasets here are vessels that received ultrasound without the incorporation of contrast agent microbubbles.

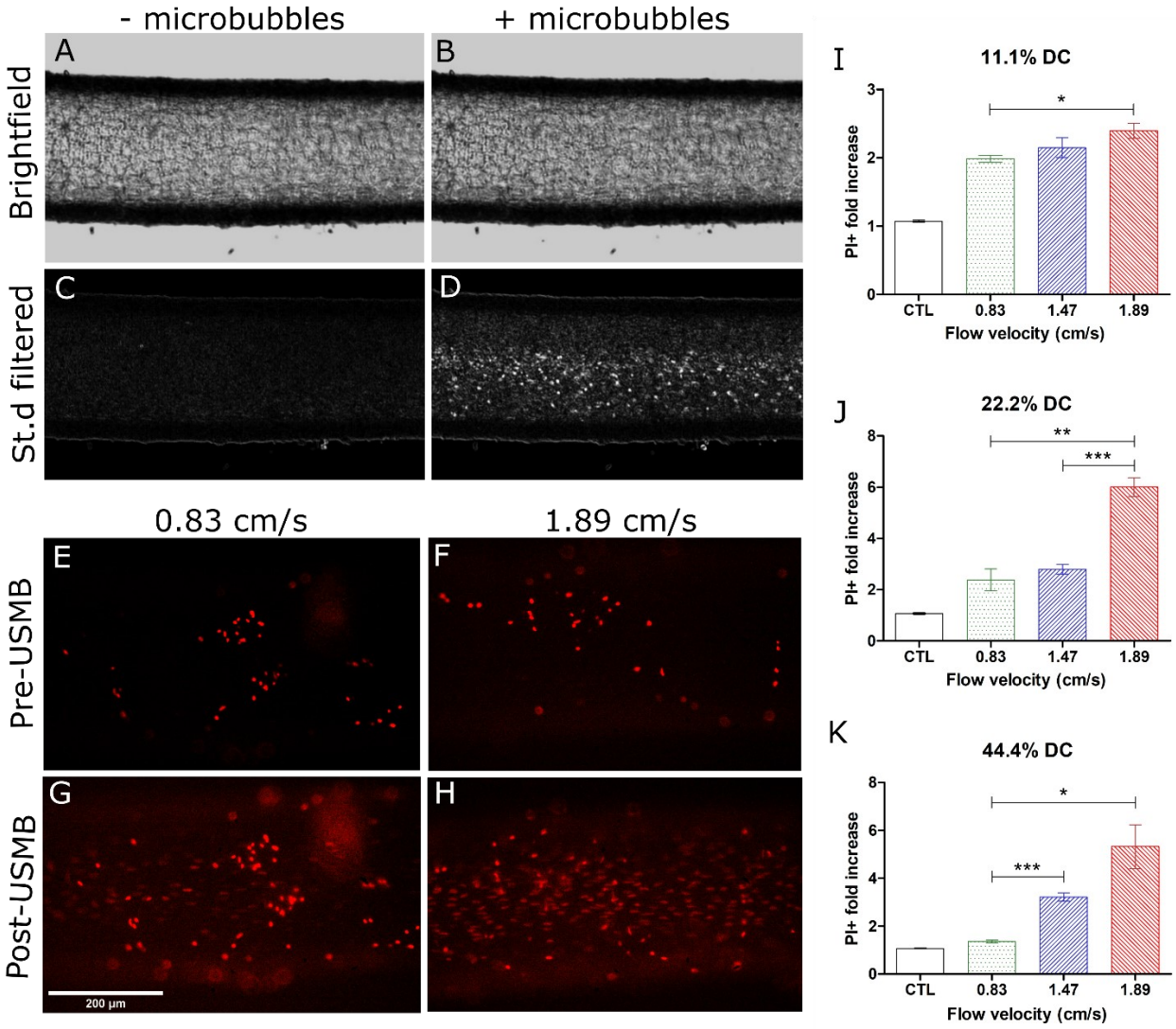

Figure 3.3: Vascular cell permeability increases with increasing microbubble flow velocity. Successful Definity® entry into the vasculature was confirmed via brightfield microscopy. Representative brightfield micrograph of a vessel (A) without and (B) with microbubbles, along with standard-deviation filtered processed versions to better delineate the flowing microbubbles (C,D). (E, F) Propidium iodide-positive (PI+) cells before and (G, H) after focused ultrasound treatments with an 11.1% DC pulse under flow velocities 0.83 cm/s and 1.89 cm/s, respectively. Quantification of flow-dependent cellular permeability, highlighting PI+ fold increase within vessels treated at (I) 11.1% DC, (J) 22.2% DC and (K) 44.4% DC at each of the flow velocities employed (at least n=3 independent vessels per condition). All of the ultrasound-treated groups were statistically different from the control group – but indicators of which were omitted to simplify the figures. Scale bar = 200 µm. Legend: * $p<0.05$; ** $p<0.01$; *** $p<0.001$.

3.5.3 Flow-dependent miR-126 delivery and vessel viability post-ultrasound treatment

While enhancing vascular cell membrane permeability is likely a necessary step for vascular gene delivery, it may not be sufficient. Thus, after confirming this flow velocity dependent bioeffect using Definity®, our next objective consisted of delivering a relevant microRNA (pro-angiogenic miR-126) to the vascular tissue. Our results indicate that, while ultrasound-assisted miR-126 delivery is also flow-rate dependent at every acoustic condition employed here, the dependence on flow velocity is approximately opposite to that of membrane perforation (Figure 3.4). Under 11.1% duty cycle treatment, we observe an 79-fold increase in miR-126 levels compared to sham and negative controls at the slowest flow velocity (0.83 cm/s), with this level of delivery decreasing to 25-fold ($p<0.003$ compared to slowest flow) and 51-fold ($p<0.026$ compared to slowest flow; $p<0.004$ compared to middle flow condition) at 1.47 cm/s and 1.89 cm/s, respectively (Figure 3.4A). This trend persists as the duty cycle increased to 22.2% (Figure 3.4B), whereby miR-126 levels increased 105-fold at 0.83 cm/s, 22-fold at 1.47 cm/s ($p<0.007$ compared to slowest flow group) and 12-fold at 1.89 cm/s ($p<0.004$ compared to slowest flow group). Finally, we assessed an even stronger acoustic condition (duty cycle=44.4%) to confirm this trend (Figure 3.4C), resulting in miR-126 levels of 23-fold at 0.83 cm/s, 17-fold at 1.47 cm/s ($p<$*n.s.* compared to slowest flow group) and 4-fold at 1.9 cm/s ($p<0.01$ compared to slowest flow group).

To more easily compare the effect of the acoustic conditions, we summarize the data in Figure 3.4D, in which all three acoustic condition datasets are overlaid. Here, two interesting trends can be observed: firstly, as previously mentioned, there is an overall inverse relationship between microbubble flow velocity and miR-126 delivery. Secondly, at a given flow velocity, it is not directly the case that a stronger acoustic condition (*i.e.* increasing duty cycle) results in

increased levels of miR-126 delivery. Both of these observations run contrary to the extent of plasma membrane permeability (Figure 3.3I-J). Finally, we confirm vessel viability post ultrasound therapy with all three acoustic regimes employed here (Figure 3.4E-F).

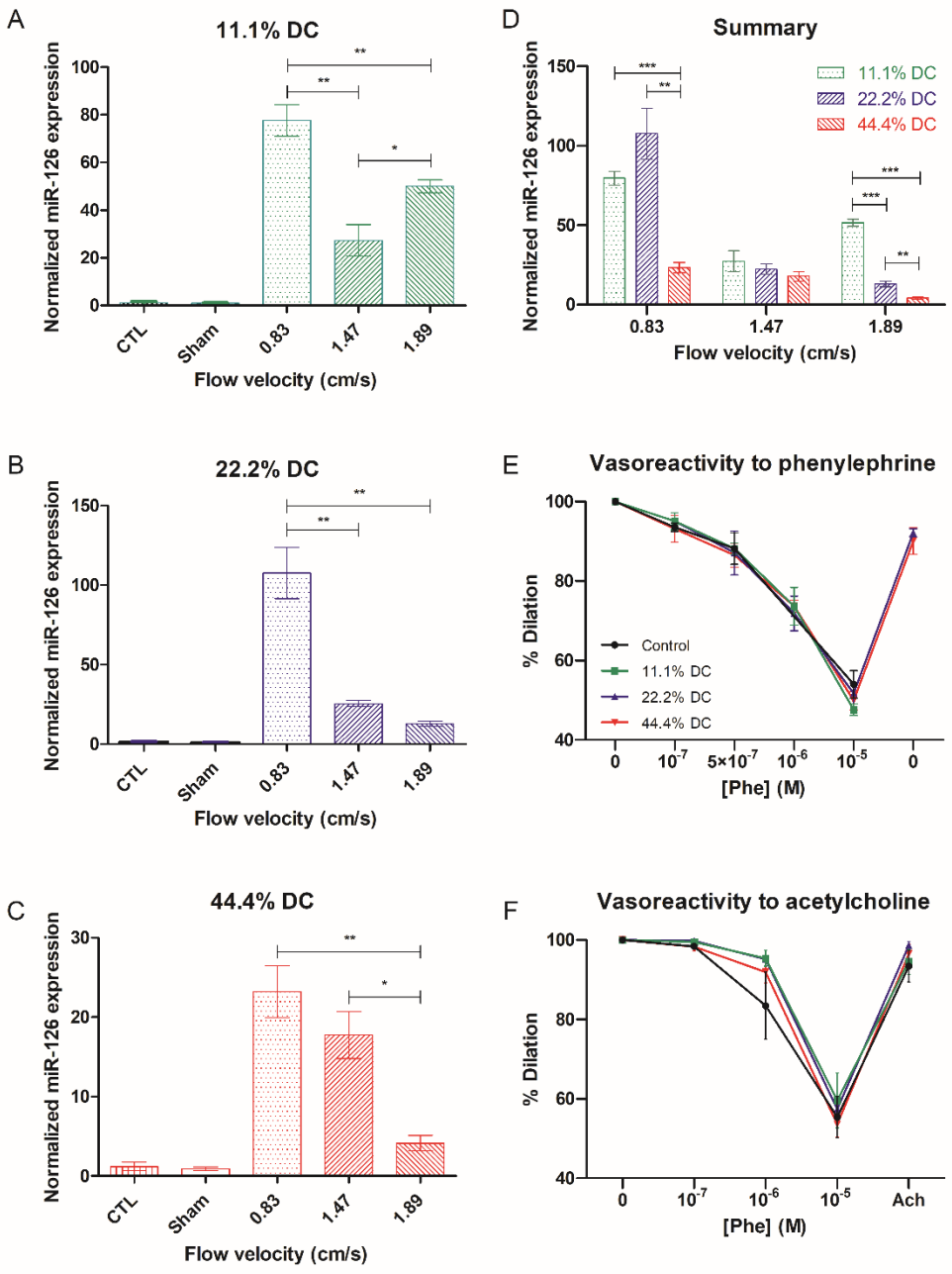

Figure 3.4: Vascular delivery of miR-126 is flow-dependent. The delivery of miR-126 due to focused ultrasound treatments at (A) 11.1%, (B) 22.2% and (C) 44.4% duty cycle exposures. Data is represented normalized to housekeeping gene, U6. A global summary of miR-126 delivery as a function of flow velocity is shown in panel (D). (E) Phenylephrine-induced vasoconstriction assay and (F) Acetylcholine-induced vasodilation assay performed 30 minutes after focused ultrasound treatments at each duty cycle regimen compared to the untreated controls (n=3 for each). All of the focused ultrasound-treated groups were statistically different from the control (no miR-126) and sham (miR-126 but no ultrasound) groups - but indicators of which were omitted to simplify the figures.

3.6 Discussion

While the vast majority of mechanistic studies are performed on cell cultures under static microbubble conditions and different acoustic arrangements, the trend of increasing pulse duration resulting in increased plasma membrane permeability is generally an established one[114,245–248]. Perhaps more comparable, a limited number of studies have highlighted increased plasma membrane permeability under increasingly faster flow velocities when subjected to the same acoustic stimulus[249]. Faster microbubble velocity allows for more replenishment of new agent within the acoustic focus, and thus more likely to interact with the surrounding vessel tissue. In addition to a pure number density argument, microbubbles are known to respond differently as a function of burst length, including an increased propensity for acoustically driven disruption[250] and radiation-force induced microbubble translation[251] with increasing pulse durations. While microbubble translation serves to decrease the average distance between microbubbles and the vessel wall, it also serves to locally increase the microbubble concentration (*i.e.* secondary Bjerknes force[252]). This may trigger unique bubble-bubble interactions that are entirely dependent on the inter-bubble spacing[253], in which bubbles that are usually non-responsive to the specific acoustic stimulus employed here become active and thus may additionally contribute to the observed bioeffects. While not directly observed here, these acoustic phenomena may explain the increased cell membrane perforation between the two acoustic regimes at a given flow velocity.

Finally, another aspect to consider is the susceptibility to mechanical perforation of the vasculature due to the differential flow-induced shear stress across the three flow velocities considered in this study. We have recently demonstrated in an endothelial monolayer model under flow conditions that shear stress preconditioning can influence microbubble-assisted ultrasound-induced membrane perforation[235] – specifically that the shear-induced levels of cytokine secretion from endothelial cells may correlate with propensity of ultrasound-assisted membrane perforation.

With regards to vascular delivery of microRNA, the flow-dependent deposition of miR-126 (Figure 3.4) runs counterintuitively with the previous permeation data (Figure 3.3). Mechanistically, this may suggest that the molecular weight of the target biologic is a key factor in delivery efficiency under flow (668 g/mol vs ~20,000 g/mol between PI and miR-126, respectively) - the practical implications of which point to context-dependent ultrasound sequences and/ or dosing paradigms.

We have demonstrated, for the first time, focused ultrasound-assisted gene delivery in an *ex vivo* vessel and revealed its dependence on the flow of the perfusate. These results have implications for emerging focused ultrasound and microbubble therapeutics spanning diseases that range in anatomical and pathophysiological flow conditions, including vascular stenosis and ischemia.

Chapter 4: Conclusions

4.1 Foreword

The research presented in Chapters 2 and 3 investigated the potential of ultrasound-mediated miR-126 delivery as a therapeutic intervention. By leveraging the unique features of focused ultrasound and microbubbles, these studies explored the feasibility of targeted gene delivery to endothelial cells, with a focus on maintaining cell and vessel viability. In the following chapter, I discuss my contributions and the limitations of these studies, as well as providing insights on further directions.

4.2 Contributions

In chapter 2, I adopted a systematic approach to investigate the potential of ultrasound-mediated gene delivery for therapeutic angiogenesis. I started with the design and synthesis of a cationic DSTAP microbubble formulation to carry an effective payload of miR-126. These microbubbles were characterized to ensure that they possessed a suitable size distribution, stability and echogenicity, comparable to clinically used agents. Through microscopy and surface charge measurements, I confirmed their ability to efficiently bind and carry miR-126 on their surface. With these miR-126-loaded microbubbles, HUVEC were treated in a custom ultrasound setup coupled with a passive cavitation detection system. This system allowed for the constant monitoring of microbubble activity throughout the treatment duration, ensuring that the microbubbles underwent stable cavitation to minimize cell damage. The RT-qPCR results show a duty cycle-dependent increase in intracellular miR-126 levels, confirming successful gene delivery. Further, I demonstrated the functional delivery of miR-126 by observing the downregulation of its target proteins, SPRED1 and PIK3R2, and an increase in endothelial tube formation, a key step in angiogenesis. As depicted in Figure 4.1, the number of nodes and tube length were quantified and demonstrates that there is a significant physiological increase in

angiogenesis mostly at the 20% duty cycle. As opposed to the qPCR data from Figure 2.4A, this suggest that there are possibly other miR-126 targets that may be involved in this process.

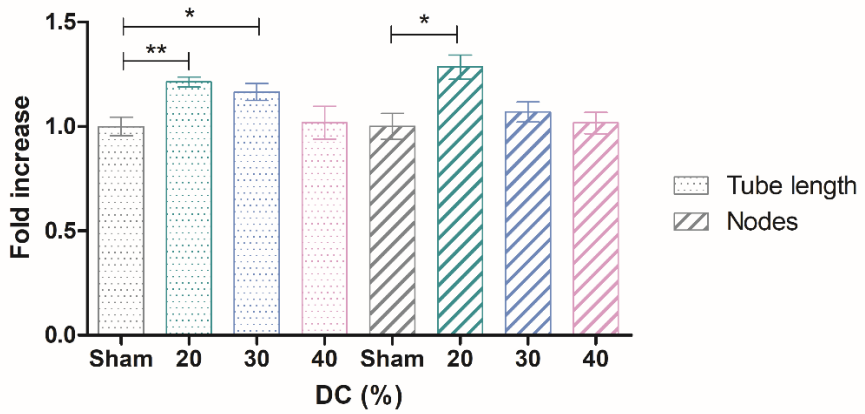

Figure 4.1:Quantification of tube length and node formation from the Matrigel assay. The results from Figure 2.4E,F were described in Chapter 2.5.2. In brief, tube length increased 2-21% and number of branching nodes increased 2-28% across the treated cells at 20-40% duty cycles compared to untreated controls. Quantification was performed with AutoTube on MATLAB. This plot was not included in the manuscript. Legend: * $p < 0.05$, ** $p < 0.01$ (n=3).

Most importantly, throughout the experiments, I prioritized maintaining cell viability while achieving a relatively modest transfection efficiency. This approach ensured the possibility for repeated treatments to further enhance therapeutic effect. By confirming stable cavitation through passive detection, the risk of potential damage associated with more aggressive ultrasound regimes was minimized.

To build upon gene delivery on endothelial cell suspensions, Chapter 3 aimed at designing a more complex *ex vivo* vascular model that takes into account the biological layers beyond the endothelium, including the vascular smooth muscles. This study aimed to understand the influence of flow velocities, a crucial parameter of vascular diseases, on microbubble-assisted permeability and the delivery of miR-126 within a pressurized mesenteric artery model. First, I confirmed that these vessels were viable by performing vasoconstriction and vasodilation assays using

phenylephrine and acetylcholine, respectively. Then, I investigated the effect of increasing flow velocities on cellular permeability and found that higher flow velocities lead to an increase in PI uptake, indicating enhanced membrane perforation. For miR-126, I observed an inverse relationship compared to membrane permeability with PI, with higher flow velocities resulted in a lower miR-126 delivery. I attributed this discrepancy mainly to the difference in molecular weight between PI and miR-126, with smaller PI molecules diffusing more easily through membrane perforations even at higher flow velocities. Additionally, some individual cell death may have occurred at the higher velocities, which could explain the decreasing trend in miR-126 delivery, but viability assays should be performed to confirm this hypothesis. These experiments did not, however, compromise the vessels' vasoactivity, confirming that the treatment conditions explored did not significantly damage the vessels. Overall, this study provides insight on the influence of flow velocities on ultrasound-mediated gene delivery and highlights the importance of considering the location and severity of vascular disease that could impact the success of gene therapy.

4.3 Limitations and future directions

In the *in vitro* study, the limitations primarily revolve around the simplified experimental setup and the lack of direct quantification of key parameters. The use of cell suspension, while allowing for passive cavitation detection, deviates from the *in vivo* environment where cells exist within the complex architecture of blood vessels. This simplification might underestimate the challenges associated with gene delivery in a more realistic setting, where factors such as cell-cell interactions, extracellular matrix, and blood flow could significantly influence cell membrane permeabilization efficiency[254]. Additionally, this study could benefit from assessing the transfection efficiency of the ultrasound-coupled setup to treat cells in suspension. Although this

metric could be heavily influenced by microbubble type[255], the size of the molecule to be delivered, as well as cell type which could be differently receptive to ultrasound parameters[256], understanding the efficiency of therapeutics delivery would allow for a more comprehensive comparison to other gene delivery methods. For future experiments, a fluorescently labelled miR or molecule could be delivered in a similar fashion, and the number of cells that would have internalized this molecule could be assessed via flow cytometry.

Moreover, the inability to quantify the precise intracellular dose of miR-126 delivered from the synthesized cationic microbubbles hinders our understanding of the dose-response relationship, as there is no universally established minimum amount of miR-126 required to induce a sufficient angiogenic response for therapeutic effect *in vivo*[257]. The levels of miR-126 required to effectively enhance vessel formation and tissue reperfusion are heavily influenced by the complexity of the disease, the specific target tissue, and the delivery methods used (*e.g.* needle injection[258], viral methods[259,260]). Current pre-clinical studies predominantly focus on establishing efficacy and feasibility rather than pinpointing precise dosage thresholds[233]. For further investigations, I would prioritize identifying an optimal dose range that balances therapeutic benefits with safety considerations. This will require *in vivo* studies that systematically evaluate varying miR-126 dosages across different disease models to contribute to the development of safe and effective miR-126-based therapies for promoting angiogenesis in a range of clinical applications.

As for Chapter 3, although the *ex vivo* study does incorporate flow conditions, the absence of blood cells in the perfusate and surrounding tissues simplifies the physiological environment. This potentially overlooks the possible interactions that could impact microbubble behaviour in response to ultrasound and gene delivery efficiency in *vivo*, particularly due to a higher fluid

viscosity[261]. Moreover, the study assessed cell membrane permeability using PI, which is often used as a dead cell marker. To discriminate dead, permeated cells from live and permeated ones, I would use a viability marker, such as Calcein-AM[115]. Additionally, this study also does not demonstrate the impact of miR-126 on vessel functionality. As mentioned in Chapter 1 (Figure 1.2), miR-126 increases the activity of eNOS and subsequently, NO production, which enhances vasodilation induced by acetycholine. To assess the influence of the increased miR-126, eNOS inhibitor *N*-nitro-L-arginine methyl ester (L-NAME) could be added to suppress the production of NO[262]. This would isolate the effects of acetycholine and microbubble cavitation on vasodilation[262] following the increase in miR-126. Finally, to further utilize this ultrasound-coupled myograph system, different types of vessels, disease models and microbubbles could be studied. For instance, the different flow patterns observed in atherosclerotic vessels could affect drug delivery[235], and the lack of fenestration in brain endothelial cells make cerebral arteries makes a great candidate to study permeability in the BBB. To further study gene delivery to ischemic vessels, targeted microbubbles (as well as cationic, miR-126-loaded microbubbles from Chapter 2) could be introduced, such as coupling a ligand targeting against P-selectin on the microbubbles, since P-selectin become rapidly expressed on endothelial cells following ischmia[263].

4.4 Conclusions

This thesis demonstrated the targeted delivery of miR-126 to endothelial cells in both *in vitro* and *ex vivo* models using ultrasound and microbubbles as tools to physically enhance miR-126 uptake. Motivated by the current clinical applications of focused ultrasound to non-invasively open the BBB to deliver therapeutics to inoperable brain pathologies and to dissolve blood clots through sonothrombolysis, maintaining cell and vessel viability was key to support the feasibility

of this approach. I hope that these findings could lead to novel pro-angiogenic clinical trials involving gene therapy and focused ultrasound.

Appendix

Published as: He, S., Singh, D., & Helfield, B. (2022). An Overview of Cell Membrane Perforation and Resealing Mechanisms for Localized Drug Delivery. *Pharmaceutics*, *14*(4), 886. https://doi.org/10.3390/pharmaceutics14040886

5.1 Foreword

The following text consists of the remaining sections of my review article presented in Chapter 1 written with Davindra Singh and Dr. Brandon Helfield. This section was omitted from the chapter because of its limited relevance to the rest of the thesis and follows section 1.3.4. The introduction section presented four physical methods of cell membrane perforation for drug delivery (microinjection, sonoporation, electroporation and photoporation), whereas this section provides insight on the possible mechanisms of membrane resealing, as well as the timescales at which key proteins are involved.

5.2 Plasma membrane repair mechanisms

Pore generation within the plasma membrane launches an immediate cellular response to restore homeostasis and preserve cell viability. In this section, the known mechanisms of cell membrane repair are described (Figure 5.1) and summarized in Table 5.1.

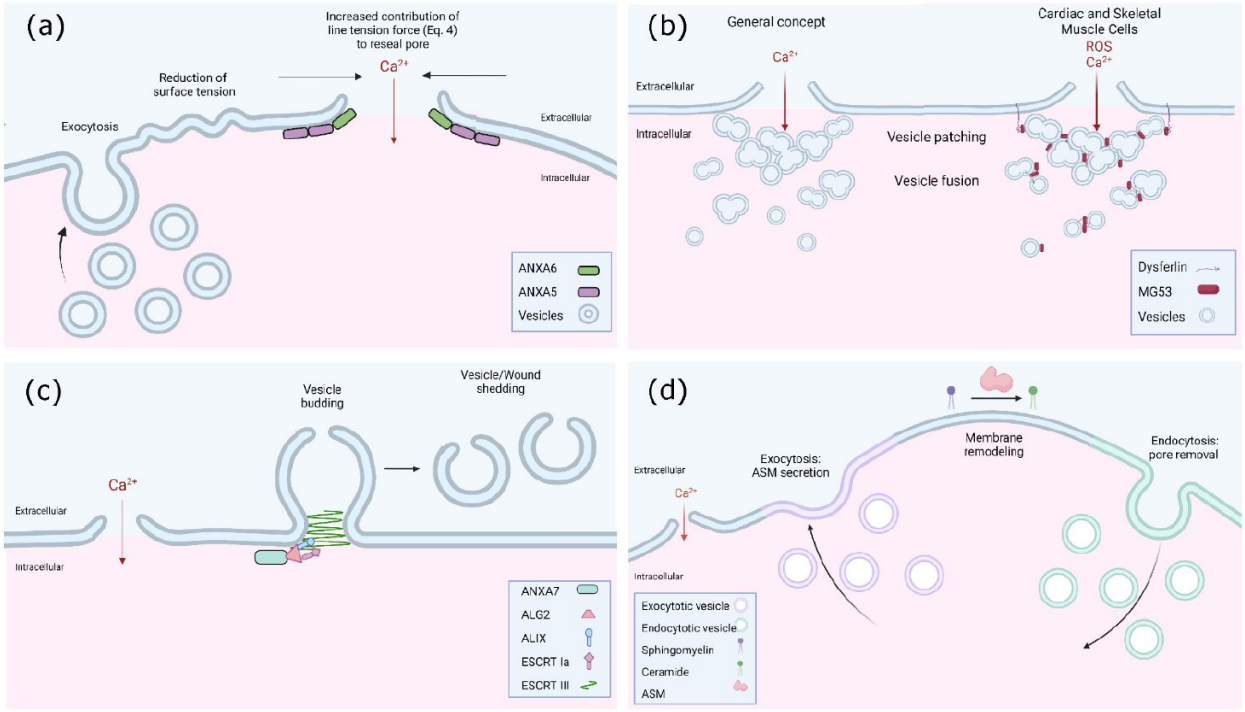

Figure 5.1: Summary of known plasma membrane resealing mechanisms. (a) The tension-reduction hypothesis; (b) the patch hypothesis; (c) the ESCRT mechanism; and (d) exocytosis/ endocytosis. See text for detail.

5.2.1 Physical intuition

As a first approach to understanding the dynamics of membrane pore resealing, it is perhaps instructive to consider the flux through a circular pore in the absence of any biological wound response. Assuming the cytoplasm is a simple fluid leaking out of a single pore of radius r_p, the flow per second normalized to initial cell volume $\tilde{Q}$ is given by the following relation[264]:

$$\tilde{Q} = \left(\frac{\Delta P}{4\pi\eta_0}\right)\left(\frac{r_p}{R}\right)^3 \tag{5.1}$$

where ΔP is the pressure difference across the membrane, R is the effective cell radius, and η_0 is the cytosolic viscosity. Assuming $\Delta P \approx 10$ Pa, an intracellular viscosity range from $\eta_0 \approx 1$ to 200 times that of pure water, and a pore size of 10% of the cell size, the leakage rate is on the order of 80%–4% of cell volume per second. From such a purely physical analysis, the necessity of viable cell membrane resealing occurring within seconds to minutes is clear. Membrane pore resealing

times, quantified as a cessation of intracellular influx, have been reported over an array of input sources (*e.g.*, ultrasound and microinjection) and across different cell types to range on this timescale[24,265–268].

Table 5.1: A summary of key proteins involved in plasma membrane repair. See text for details.

Protein family	Role	Ca^{2+} binding	Estimated pore size in which proteins have been observed	Suggested plasma membrane repair mechanism(s)
Annexins	Play a role in membrane patching, fusion, reshaping, reducing membrane tension, removing damaged membrane, limiting pore expansion	Yes	nm - μm scale[269–271]	Patch, tension reduction, exocytosis/ endocytosis, membrane budding (A7[272])
SNARE proteins	Mediate membrane fusion	No	0.5-3 μm[273,274]	Patch, tension reduction, exocytosis, endocytosis,
SYT7	Help activate SNAREs	Yes		
S100A11	Implicated in membrane and cytoskeletal dynamics, interacts with A2	Yes	0.5-1.3 μm[269,275]	Tension reduction[276]
Dysferlin	In muscles cells, accumulates at the site of membrane damage, interacts with some annexins, MG53, BIN1, EHD1	Yes	nm scale[277], μm scale[270]	Patch[277], tension reduction[278]
MG53	In muscles cells, it is tethered to plasma membrane and intracellular vesicles and, upon ROS stimulus, oligomerizes and accumulates at wound sites	No	nm scale	Patch[279], tension reduction[278]
ESCRT-III	Involved in membrane budding	No	<100 nm[280], >1 μm[281]	Membrane budding
ESCRT-I	Recruits ESCRT-I	No		
ALIX	Recruits ESCRT machinery	Yes		
ALG-2	Recruits ALIX	Yes		
ASM	Outer plasma membrane remodeling to initiate inward vesicle budding. Converts sphingomyelin into ceramide	No	nm scale[282]	Exocytosis/ endocytosis

5.2.2 Repair triggers

It is well established that calcium ions are involved in a plethora of signaling pathways and cellular processes and, as such, intracellular Ca^{2+} concentration is well regulated. Due to the 10,000-fold gradient maintained across the plasma membrane[283], a localized breach of the plasma membrane results in an immediate calcium ion influx and is considered the universal trigger that launches the mechanisms of perforation repair[9] . Indeed, it presumably dictates the magnitude of plasma membrane repair as entry levels are approximately correlated to pore size, duration, and/or density, while an excessive level of intracellular Ca^{2+} is cytotoxic[8]. Previous works have demonstrated that membrane resealing timescales increase in low Ca^{2+} environments and fail to reseal in the complete absence of extracellular Ca^{2+} [8,284,285]. Calcium entry through membrane perforations selectively activates Ca^{2+}-dependent cellular responses depending on both the local Ca^{2+} concentration and the relative affinity of Ca^{2+} binding proteins[286]. This enables cells to mount a spatially and temporally regulated response to steep Ca^{2+} influx[276]. The extracellular Ca^{2+} concentrations required for successful resealing have been reported in the μM to mM range[287], depending on the cell type and the wound generating mechanism, and tolerable increases in intracellular Ca^{2+} also vary between cell types. This highlights that tight control over Ca^{2+} dynamics is required to maintain cell viability following membrane perforation.

Oxidation at the plasma membrane is another trigger that initiates repair mechanisms in skeletal and cardiac cells[288]. Previous studies conducted on myotubes have elucidated the role of the protein Mitsugumin 53 (MG53) in muscle cell repair[289]. In the presence of a reducing agent in the extracellular environment, the accumulation of MG53 is hindered compared to the addition of an oxidizing agent, which increases the rate of MG53 accumulation at the site of cellular injury. MG53 also interacts with dysferlin to be translocated to the region where the concentration of free

radicals is highest to seal the pore in a "patching" manner, typically within a minute after membrane injury[277]. The role of MG53 in membrane fusion, budding, and exocytosis is modulated by muscle-specific caveolin-3 (Cav3) for proper sarcolemma repair during muscle contractions and differentiation[279].

5.2.3 Plasma membrane repair hypotheses

A breach of the plasma membrane disrupts the tension sustained by the lipid bilayer. Nanosized pores are frequently and transiently formed on cellular membranes as the cell naturally synthesizes organelles, moves, or contracts[290]. In these cases, the lipid bilayer can reseal these pores without requiring a cascade of proteins. Given this, there have been many experimental and theoretical investigations of wound healing on pure lipid vesicles, whereby the passive pore-opening and resealing dynamics are due to the force balance per unit length between two opposing forces:

$$F = 2\sigma(r_p) - \frac{\lambda}{r_p} \tag{5.2}$$

where $\sigma(r_p)$ is the plasma membrane surface tension that acts to pull the pore of radius r_p open, and λ is the line tension that is associated with the energy penalty of having exposed hydrophobic lipids along the pore perimeter and acts to close the pore. The relatively simplistic model given above predicts that pore size, opening, and resealing times are a function of lipid composition and cell viscosity[264,291].

Early experiments in sea urchin cells and mammalian cells revealed the localized fusion of intracellular vesicles with the plasma membrane, leading to two fundamental hypotheses for wound resealing[9]: (i) the 'tension reduction' hypothesis stipulates that the excessive membrane surface area delivered via the exocytosis of pre-existing intracellular vesicles serves to rapidly

decrease the membrane surface tension to promote wound closure (see Equation (5.2)); and (ii) the fusion of pre-existing vesicles in the vicinity of the pore, including lysosomes, create a 'patch' that merges with the plasma membrane to seal the wound. Although the mechanisms underlying plasma membrane repair in mammalian cells are not fully elucidated and may differ between cell types and the source of the perforation, increasing evidence suggests that annexins are one of the first to be recruited to the wound site[272]. The annexin family, consisting of twelve proteins (A1–A11, A13), is made up of phospholipid-binding proteins that are triggered to migrate from the cytosol to the plasma membrane under local increases of Ca^{2+} concentration as early as 10–45 s post-perforation[292]. As each of these proteins exhibits its own Ca^{2+} sensitivity threshold, this family presents a broad Ca^{2+} sensing mechanism that responds dynamically during a wound repair event. There is evidence that annexins play a role in the immediate 'patching' of the perforation in an attempt to minimize cytosolic loss and intracellular Ca^{2+} increase. Annexin protein A5, when recruited to the perforation site, has been shown to form a 2D protein array to temporarily delay diffusion and limit wound expansion[293]. Annexin protein A4 binds to the plasma membrane adjacent to the opening and changes conformation to reshape the lipid bilayer, while annexin A6 constricts the wound to prevent it from expanding and to promote closure[271].

Synaptotagmin 7 (SYT7), a member of the synaptotagmin protein family, is a Ca^{2+}-sensing protein present on the membrane of lysosomes that plays a critical role in lysosomal fusion and membrane patching, as its inhibition leads to impaired membrane repair[294]. Further, SYT7, among other members of its protein family, regulates the formation of soluble N-ethylmaleimide sensitive factor attachment protein receptor complexes (SNARE), which are a large group of small proteins that are key mediators of all intracellular membrane fusion events[295]. As opposed to SYT7 acting as a Ca^{2+}-dependent modulator of membrane fusion, another Ca^{2+} sensor, the apoptosis-linked

gene 2 (ALG-2), modulates membrane fission machinery to mediate pore repair. ALG-2 recruits important membrane-trafficking scaffold proteins, including ALG-2 interacting protein X (ALIX), which then recruits components of the endosomal sorting complex required for transportation (ESCRT) machinery[8]. ESCRT-III, normally associated with its role in multivesicular body biogenesis, has been shown to translocate to the wound site through the recruitment of ALIX, ESCRT-1a, and ESCRT-II[272,296,297]. Indeed, under specific perforation conditions, a lack of ALG-2 or ALIX results in failed membrane repair[281]. The ESCRT machinery has, therefore, recently been suggested as a third alternative mechanism in addition to the patching and membrane tension reduction hypotheses, in which membrane lesions are actively removed through the formation of vesicles outwards from the damaged membrane—the shedding of membrane buds[296,298], see Figure 5.1c.

While lysosome fusion was originally only thought to contribute to membrane patching, recent observations of massive Ca^{2+}-dependent endocytosis following lysosomal exocytosis[299] have revealed a fourth hypothesis for membrane pore repair: the 'exocytosis/ endocytosis' pathway (Figure 5.1d). The fusion of lysosomes to the site of injury promotes the release of lysosomal enzyme acid sphingomyelinase (ASM), which remodels the outer leaflet of the plasma membrane. This novel form of endocytosis, which takes place within seconds of membrane injury, has been shown to be induced by the modification of plasma membrane lipid sphingomyelin into ceramide[300], resulting in the formation of large domains capable of inward budding[301].

It should be stated here that, although presented as separate mechanisms, it is possible that multiple approaches to plasma membrane repair occur simultaneously and synergistically. For example, ESCRT-III recruitment to the cell membrane has been observed when membrane tension is low[297], and lysosomal (and other intracellular vesicles) fusion can contribute to all pathways.

The threshold perforation size for these mechanisms is not yet fully elucidated but likely plays a role in the extent to which one mechanism is favoured over others.

5.3 Cytoskeletal remodeling during perforation

In the context of physical permeation strategies, cell membrane perforation often results in a local disruption of the actin cortex. As a consequence, pore recovery depends on the spatial–temporal coordination between key protein families involved in membrane recovery, cytoskeletal architecture, and vesicle fusion. The following section outlines the salient proteins involved in these processes and is summarized in Table 5.2.

Table 5.2: A summary of the involvement of cytoskeletal remodeling post-pore formation. See text for detail.

Cytoskeletal remodeling	**Main proteins involved**	**Estimated pore sized in which proteins have been observed**
Contractile ring[302]	Actin, myosin II, GTPases (Cdc42, Rho), Arp2/3	~μm scale[303,304]
S100A11-A2[269]	S100A11, annexins A1, A2	0.5-1.2 μm[269,275]
Repair cap[305]	Annexins A1, A2, A5 and A6, dysferlin, EHD1/2, MG53, BIN1	~μm scale[270]
Exocytosis/ endocytosis[306]	Myosin family, kinesin, actin, GTPases, formins, SNARE complexes	0.01-1 μm[306]

5.3.1 Initial reaction: deconstruction of actin network

Local Ca^{2+} influx due to membrane perforation activates cytoskeletal-remodeling proteins, such as the inverted formin-2 (INF2) and calpain protease, that allow for the disassembly of the local cortical actin[307]. This disassembly helps reduce membrane surface tension and improves access for intracellular vesicles to fuse with the plasma membrane[10]. Indeed, studies have shown that the presence of actin depolymerization agents, such as DNAse 1, acts to enhance the reparation of damaged cell membranes, while actin stabilizing agents result in a decrease in the resealing

rate[308]. Further, this disassembly has been shown to occur for small and large membrane lesions[309] and is likely a requirement irrespective of perforation size. Similar to the actin network, the microtubule network also undergoes a brief period of local disassembly at the damaged site[310]. The perforation pathway triggers the recruitment of the microtubule-associated protein 1 (EB1), which both promotes the reassembly of microtubules and facilitates the transport of lipids to the wound area[267]. Indeed, given that directional vesicle transport to the site of perforation is controlled by myosin and kinesin activity through the reorganized elongated microtubules[311], a rapid repair and remodeling of the breached cytoskeletal architecture is required for viable perforation repair.

5.3.2 Resealing and remodeling: actomyosin contractile ring

One such remodeling mechanism is the formation of an actomyosin ring that has been shown in multiple models, including *Xenopus* oocytes and *Drosophila* embryos[276]. For this process, two elements of the cytoskeleton are required: actin and myosin II. These are both recruited to the wound edge, assemble as contractile arrays surrounding the perforation, and continuously contract throughout the repair process. The spatial–temporal regulation of the actomyosin ring is regulated by Ca^{2+}-dependent Rho GTPases, specifically Cdc42 and RhoA[276]. Indeed, the Rho family of GTPases plays a major role in cytoskeletal regulation and, consequently, is involved in cell migration, adhesion, cytokinesis, and perforation repair[276]. GTPases act as molecular switches that can modulate signal transduction pathways in response to a specific stimulus. Activated RhoA accumulates in a ring around the perforation area (*i.e.*, a RhoA activity zone) and spatially overlaps with myosin II, while the concentric Cdc42 activity zone overlaps with the actin ring[312]. Myosin II is recruited by the RhoA activation of Rho-associated kinase (ROK)[304], and the Cdc42 activity zone is responsible for the recruitment and polymerization of branched actin filaments through downstream effectors, such as the neuronal Wiskott-Aldrich

syndrome protein (N-WASP) and p21-activated kinases, that control the Arp2/3-dependent actin assembly[313]. Overall, the formation of these zones has been shown to occur within 30–45 s in Xenopus and Drosophila models[314] and has been shown to be active for the repair of wounds within the micrometer range[315]. Microtubules are also shown to be essential in the recruitment of Arp2/3 and myosin II and help focus the zone of actin and myosin II assembly at the wound edge[303].

Together, these proteins create an actomyosin cable around the wounded area that is coupled to the plasma membrane by junction proteins such as E-cadherin and β-catenin. In E-cadherin-deficient cell models, wound overexpansion and improperly formed actomyosin rings are observed, yet complete wound repair remains possible, suggesting that other proteins are involved in the tethering of the actomyosin ring to the plasma membrane[316]. The circular constriction shortens the actomyosin cable that pulls the membrane closer together to close the wound and is often referred to as the 'purse-string' mechanism. This mechanism is also seen in multicellular epithelial models, in which the Rho GTPase and ROK are essential for the assembly actomyosin ring intracellularly between the nearby cells[317]. This actomyosin ring is then anchored to the membrane through adherens and tight junctions, such as E-cadherin and the tight junction protein Zonula Occludens-1 (ZO-1)[318], while constriction is initiated by the phosphorylation of myosin regulatory light chain (MLC)[319].

Though this repair model has been fully explored and described in embryonic mammalian models and multicellular epithelial models, the formation of the contractile ring is still yet to be seen in single somatic cells[320]. However, even though the ring itself is not seen, individual components are still shown to play a major role in cytoskeletal restructuring for membrane repair. Cdc42 and Rho, for example, are shown to be translocated from the cytosol to the membrane for cytoskeletal reorganization in shear-stress-damaged bovine aortic endothelial cells[321]. In laser-

wounded skeletal muscle cells, RhoA activity is induced by Ca^{2+} influx[322], and F-actin accumulation at the wound site has been shown post-perforation in human endothelial cells[266], cancer cells[269], and muscle cells[305].

5.3.3 Resealing and remodeling: S100A11-A2

In somatic cell models, another cytoskeleton remodeling mechanism has been demonstrated that utilizes the Ca^{2+} binding protein S100A11 and annexin A2. These proteins have been shown to be active in wounded mammalian cells, such as in cancer cells and vascular endothelial cells[269,275]. With the influx of extracellular calcium, the EF hand-type protein, S100A11, is activated and binds to F-actin along with annexin A2, which is also capable of Ca^{2+}-dependent membrane binding[269]. The binding of these proteins to the cortical actin of the wounded membrane restricts the depolymerization of the F-actin while also promoting the buildup and increase in the polymerization of actin at the wounded zone[269]. The increase of cortical F-actin results in wound closure, and it is suggested to be related to the purse-string closure mechanism due to the buildup of cortical actin being analogous to the actin activity in wounded *Xenopus* oocytes[269]. Concurrently, annexin A1 accumulates on the damaged region of the membrane and labels it for excision[269]. In combination, the S100A11-A2 complex is able to bind to the membrane and pull it closer together, while annexin A1 removes damaged membranes. The necessity of this complex was shown in S100A11- and A2-depleted endothelial cells, in which pore resealing was either delayed or failed completely in both laser- and glass-beads-induced membrane damage models[323]. Overall, these components provide an alternate cytoskeletal remodeling mechanism for wounded membranes.

5.3.4 Resealing and remodeling: repair cap

In muscle cells, another mechanism referred to as a "repair cap" is shown to occur post-membrane-wounding[305,324]. In this instance, an influx of Ca^{2+} results in the translocation of annexins towards the wounded membrane, particularly annexin A1, A2, A5, and A6; these accumulate and form a "cap" along the damaged region of the plasma membrane. This annexin-rich cap is supported both by a "shoulder" structure, shown to be essential for the repair cap formation, and consisting of proteins including dysferlin, EHD1/2, MG53, and BIN1[8,305], and by F-actin recruitment to the non-annexin region below the cap. The formation of the repair cap is shown to be both Ca^{2+}-and actin-dependent, demonstrating the necessity of cytoskeleton remodeling for this membrane repair mechanism[270,305].

5.3.5 Resealing and remodeling: exo/endocytosis events

All of the aforementioned plasma membrane repair pathways include steps that involve membrane fusion, exocytosis, or endocytosis, and in this manner the cytoskeleton plays a vital part in perforation repair (Table 5.2). All of the highly regulated steps of exocytosis, including the shuttling of vesicles to the peripheral membrane, vesicular fusion with the plasma membrane, and the release of vesicular content, are regulated by the actin cytoskeleton[306]. As exocytic vesicle size varies as a function of secretory cell type (~0.01–1 μm), so does the timescale over which exocytosis occurs (~0.1–100 s), exhibiting an inverse relationship[306]. Vesicle transport along actin filaments requires actin-based motor proteins such as kinesin or members of the myosin V family[311]. While the molecular details differ between different vesicles, myosin V_a is associated with several vesicles and has been shown to play a major role in this regard (e.g., endothelial cells[325] and neurons[326]). After membrane fusion by SNARE complexes[327], it has been suggested that the final expulsion of the vesicles utilizes an actin coat/ring at the base of the vesicle[328]. This

mechanism is shown in laser-ablated HUVECs, in which Ca^{2+} influx results in the exocytosis of Weibel–Palade bodies, secretory organelles involved in the initiation of inflammation. In this model, Rho GTPases result in the recruitment of an actin ring at the base of the vesicle, while the contraction is enabled by myosin II-mediated constriction[329].

As stated above, the exocytosis-mediated release of ASM has been shown to result in a ceramide-coated membrane, ultimately triggering membrane invagination[330]. Indeed, studies have demonstrated that the transcriptional silencing of ASM inhibits membrane repair, while adding exogenous ASM can cause it to recover[300]. Recent work has suggested that the form of endocytosis that is stimulated by this mechanism is caveolin-dependent[331], implying that the usual role of the cytoskeleton in caveolin-mediated endocytosis is at play during perforation resealing under this pathway.

5.4 Future perspectives

The investigation of individual cell wound repair mechanisms in the context of targeted drug and gene delivery can offer tremendous insight into the development of strategies designed to improve treatment outcomes through the modulation of perforation kinetics. This is especially of interest in optimizing in vivo techniques (*e.g.*, sonoporation), whereby elucidating the mechanisms of perforation repair in human cells can aid in treatment design and planning. These strategies, whether physical or pharmacological, have applications both in targeted genetic delivery techniques (e.g., ischemia and cardiovascular disease) where preservation of cell viability is paramount and in cancer-related treatments where perhaps immediate and selective cancer cell death is the primary objective. Perhaps the most universal approach to altering the repair kinetics of individual cells is the administration of a Ca^{2+} chelator (*e.g.*, BAPTA-AM) either during or immediately post-perforation[332]. As the key trigger and regulator of membrane repair, the local

modulation of Ca^{2+} influx affects the spatial and temporal evolution of wound repair, potentially altering perforation size, repair timescale, and long-term cell viability via the activation/inhibition of Ca^{2+}-dependent cellular responses[333]. The depletion of extracellular Ca^{2+} also induces the dissociation of intracellular junctions[334], including adherens and tight junctions, promoting paracellular drug transport. This may have a particular impact in aiding the targeted delivery of therapeutics to the brain via the reversible opening of the blood–brain barrier[335], an area in which microbubble-mediated focused ultrasound therapy, in particular, is rapidly progressing[36]. Further, there are novel advancements in the field of nanoparticle synthesis designed to modify the Ca^{2+} environment and affect local Ca^{2+} homeostasis. These techniques incorporate materials that are either Ca^{2+}-coated[336] or Ca^{2+}-binding[337] to influence the repair dynamics in wound healing applications.

The properties of plasma membranes, including lipid fluidity and phospholipid packing, play a role in their repair dynamics (*e.g.*, the 'tension-reduction' hypothesis for perforation resealing). Indeed, lipid composition is regulated in response to pathological as well as pharmacological triggers. Membrane lipid alterations have been shown to be involved in many diseases, including cancer, atherosclerosis, and neurodegenerative diseases (*e.g.*,[338]). One such example is the regulation of plasma-membrane-incorporated cholesterol, which may be dysfunctional in cancer cells[339] and result in variations in membrane fluidity and surface tension. Membrane cholesterol content is a key factor in modulating perforation repair dynamics, as has been demonstrated and physically modeled using giant unilamellar vesicles, resulting in shorter pore lifetimes with increasing cholesterol content[291]. Localized co-treatment with cholesterol depletion drugs, for example Filipin, ultimately decreases lipid raft number and membrane rigidity and may provide a means to ensure rapid resealing post-drug-delivery. Alternative lipid-altering

strategies, such as incorporating pluronic polymers as part of the drug payload (*e.g.*, Tween and polyethyleneglycol)[340], have the potential to preserve and amplify cell membrane recovery[341] and to facilitate intracellular drug transport[342]. Indeed, as polyethylene-glycol is a typical constituent of ultrasound-stimulated microbubbles used for sonoporation, microbubbles present a novel intrinsic vehicle for the local and targeted modulation of cell membrane viscoelasticity, as recently demonstrated[343]. It is well known that the composition of the outlet leaflet of the plasma membrane modifies its local surface tension and can trigger specific membrane repair mechanisms (*e.g.*, the 'exocytosis/endocytosis' pathway), and this presents a unique strategy for tailoring drug/gene delivery treatment efficiency and timescales. Short-chain ceramides (with chain lengths four to eight carbons long) have been shown to readily incorporate into the outlet leaflet of the plasma membrane[344]. In contrast to their long-chained counterparts, short-chain ceramides are not able to form lipid rafts nor increase membrane rigidity[345]. Therefore, short-chain ceramides can be employed externally to increase membrane fluidity and have been used in conjunction with cancer therapeutics to improve intracellular drug permeability[346]. Indeed, the field of membrane lipid therapy, whereby the modulation of cell membrane composition can be achieved pharmacologically through membrane structure reorganization, regulation of enzymatic activity, and modulation of lipid-based gene expression[347], can be incorporated into targeted membrane-permeation strategies to tailor pore kinetics. In fact, cancer treatments based on membrane lipid therapy have been investigated in clinical trials of patients with advanced solid tumors (*e.g.*, NCT02201823 and NCT01792310).

Aside from direct plasma membrane alteration, phospholipid-binding and cytoskeletal proteins offer promising targets for modulating perforation recovery dynamics, one of which is the annexin family of proteins. Previous studies have shown that treatment with annexin-1-derived

peptides (*e.g.*, Anx-12–26) elicits cyto-protective actions and shortens cardiomyocyte injury recovery time[348], facilitates wound healing in vivo[349], promotes epithelial repair[350], and can aid in the restoration of adherens junctions and the normalization of barrier integrity[351]. Recent studies have also demonstrated that treatment post-injury with recombinant annexin 6 enhances membrane repair capacity[352]. Further, annexin 5 has been investigated both as a diagnostic and as a therapeutic tool due to its strong binding affinity to phosphatidylserine, which results in an imaging surrogate for apoptosis in vivo and a potential anticoagulant, as it binds to activated platelets to prevent thrombin formation[353]. Additionally, annexin 5 has anti-inflammatory properties due to its potential to modulate nitric oxide signaling cascades, which has launched recent clinical trials investigating the delivery of recombinant human annexin 5 in patients with sepsis and COVID-19 (NCT04850339, NCT04748757). Tension development through the modulation of GTPases and cytoskeletal organization is also a promising approach to altering perforation kinetics[354]. The selective pharmacological inhibition of tension development, including the blocking of myosin II (blebbistatin), Rho-associated protein kinases (Y27632), and myosin light chain (ML-7), has been shown to result in a decrease in pore retraction time and prolongation of total perforation recovery, demonstrated in human dermal and lung microvascular endothelial cells[355], as well as neuroendocrine cells[356].

5.5 Conclusions

Cellular recovery from plasma membrane perforation is critical to ensure successful drug delivery using physical techniques. Indeed, fundamental molecular biology studies on individual cell membrane pore repair have brought tremendous insight into the arrangement of the key molecular actors at play. In coordination with salient Ca^{2+}-dependent proteins, including the annexin family, various plasma resealing mechanisms have been put forth, including the ‘tension-

reduction', 'patch', 'shedding', and 'exocytosis/endocytosis' pathways. In conjunction with cytoskeletal reorganization involving actin and/or myosin and their roles in vesicular trafficking, these mechanisms likely work in concert to achieve rapid localized repair and control perforation dynamics. As such, physical membrane perforation techniques employed for targeted in vivo drug/gene delivery, including the use of microbubble-mediated ultrasound perforation, may benefit from co-administration with pharmacological agents to selectively modulate the spatio–temporal dynamics of membrane perforation to enhance therapeutic effectiveness.

Bibliography

1. Allen TM, Cullis PR. Drug delivery systems: Entering the mainstream. *Science (80-)*. 2004;303:1818–1822.
2. Manzari MT, Shamay Y, Kiguchi H, Rosen N, Scaltriti M, Heller DA. Targeted drug delivery strategies for precision medicines. *Nat Rev Mater*. 2021;6:351–370.
3. Stewart MP, Langer R, Jensen KF. Intracellular delivery by membrane disruption: Mechanisms, strategies, and concepts. *Chem Rev*. 2018;118:7409–7531.
4. Peer D, Karp JM, Hong S, FaroKhzad OC, Margalit R, Langer R. Nanocarriers as an emerging platform for cancer therapy. *Nat Nanotechnol*. 2007;2:751–760.
5. Langer R. New Methods of Drug Delivery. *Science (80-)*. 1990;249:1527–1533.
6. Dong P, Rakesh KP, Manukumar HM, Mohammed YHE, Karthik CS, Sumathi S, Mallu P, Qin HL. Innovative nano-carriers in anticancer drug delivery-a comprehensive review. *Bioorg Chem*. 2019;85:325–336.
7. Andrews NW, Corrotte M. Plasma membrane repair. *Curr Biol*. 2018;28:R392–R397.
8. Jimenez AJ, Perez F. Plasma membrane repair: the adaptable cell life-insurance. *Curr Opin Cell Biol*. 2017;47:99–107.
9. Mcneil PL, Kirchhausen T. An emergency response team for membrane repair. 2005;6:499–506.
10. Horn A. Cellular mechanisms and signals that coordinate plasma membrane repair. *Physiol Behav*. 2016;176:139–148.
11. Zhang Y, Yu LC. Single-cell microinjection technology in cell biology. *BioEssays*. 2008;30:606–610.
12. Gordon JW, Scangos GA, Plotkin DJ, Barbosa JA, Ruddle FH. Genetic transformation of mouse embryos by microinjection of purified DNA. *Proc Natl Acad Sci U S A*. 1980;77:7380–7384.
13. Hofmann A, Zakhartchenko V, Weppert M, Sebald H, Wenigerkind H, Brem G, Wolf E, Pfeifer A. Generation of transgenic cattle by lentiviral gene transfer into oocytes. *Biol Reprod*. 2004;71:405–409.
14. Auerbach AB. Production of functional transgenic mice by DNA pronuclear microinjection. *Acta Biochim Pol*. 2004;51:9–31.
15. Bongso TA, Sathananthan AH, Wong PC, Ratnam SS, Ng SC, Anandakumar C, Ganatra S. Human fertilization by micro-injection of immotile spermatozoa. *Hum Reprod*. 1989;4:175–179.
16. Szabo TL. Diagnostic Ultrasound Imaging: Inside and Out, 1st ed. London, UK: Elsevier; 2004: 1-576.
17. Medwin H. Counting bubbles acoustically : a review. *Ultrasonics*. 1977;:7–13.
18. Averkiou MA, Bruce MF, Powers JE, Sheeran PS, Burns PN. Imaging Methods for Ultrasound Contrast Agents. *Ultrasound Med Biol*. 2020;46:498–517.
19. Helfield B. A review of phospholipid encapsulated ultrasound contrast agent microbubble physics. *Ultrasound Med Biol*. 2019;45:282–300.
20. Chen H, Kreider W, Brayman AA, Bailey MR, Matula TJ. Blood vessel deformations on microsecond time scales by ultrasonic cavitation. *Phys Rev Lett*. 2011;106:1–4.
21. Cho EE, Drazic J, Ganguly M, Stefanovic B, Hynynen K. Two-photon fluorescence microscopy study of cerebrovascular dynamics in ultrasound-induced blood – brain barrier opening. *J Cereb Blood Flow Metab*. 2011;31:1852–1862.
22. Helfield BL, Chen X, Qin B, Watkins SC, Villanueva FS. Mechanistic Insight into

Sonoporation with Ultrasound-Stimulated Polymer Microbubbles. *Ultrasound Med Biol*. 2017;43:2678–2689.
23. Van Wamel A, Bouakaz A, Versluis M, De Jong N. Micromanipulation of endothelial cells: Ultrasound-microbubble-cell interaction. *Ultrasound Med Biol*. 2004;30:1255–1258.
24. Hu Y, Wan JMF, Yu ACH. Membrane perforation and recovery dynamics in microbubble-mediated sonoporation. *Ultrasound Med Biol*. 2013;39:2393–2405.
25. Helfield B, Chen X, Watkins SC, Villanueva FS. Biophysical insight into mechanisms of sonoporation. *Proc Natl Acad Sci*. 2016;113:9983–9988.
26. Qin P, Xu L, Han T, Du L, Yu ACH. Effect of non-acoustic parameters on heterogeneous sonoporation mediated by single-pulse ultrasound and microbubbles. *Ultrason Sonochem*. 2016;31:107–115.
27. Kooiman K, Foppen-Harteveld M, van der Steen AFW, de Jong N. Sonoporation of endothelial cells by vibrating targeted microbubbles. *J Control Release*. 2011;154:35–41.
28. Zeghimi A, Uzbekov R, Arbeille B, Escoffre JM, Bouakaz A. Ultrastructural modifications of cell membranes and organelles induced by sonoporation. *IEEE Int Ultrason Symp IUS*. 2012;:2045–2048.
29. Mehier-Humbert S, Bettinger T, Yan F, Guy RH. Plasma membrane poration induced by ultrasound exposure: Implication for drug delivery. *J Control Release*. 2005;104:213–222.
30. Schlicher RK, Radhakrishna H, Tolentino TP, Apkarian RP, Zarnitsyn V, Prausnitz MR. Mechanism of intracellular delivery by acoustic cavitation. *Ultrasound Med Biol*. 2006;32:915–924.
31. Prentice P, Cuschieri A, Dholakia K, Prausnitz M, Campbell P. Membrane disruption by optically controlled microbubble cavitation. *Nat Phys*. 2005;1:107–110.
32. Fan Z, Liu H, Mayer M, Deng CX. Spatiotemporally controlled single cell sonoporation. *Proc Natl Acad Sci*. 2012;109:16486–16491.
33. Helfield B, Black JJ, Qin B, Pacella J, Chen X, Villanueva FS. Fluid Viscosity Affects the Fragmentation and Inertial Cavitation Threshold of Lipid-Encapsulated Microbubbles. *Ultrasound Med Biol*. 2016;42:782–794.
34. Bao S, Thrall BD, Miller DL. Transfection of a reporter plasmid into cultured cells by sonoporation in vitro. *Ultrasound Med Biol*. 1997;23:953–959.
35. Chen HH, Matkar PN, Afrasiabi K, Kuliszewski MA, Leong-Poi H. Prospect of ultrasound-mediated gene delivery in cardiovascular applications. *Expert Opin Biol Ther*. 2017;16:815–826.
36. Hynynen K. Ultrasound for drug and gene delivery to the brain. *Adv Drug Deliv Rev*. 2008;60:1209–1217.
37. Escoffre JM, Piron J, Novell A, Bouakaz A. Doxorubicin delivery into tumor cells with ultrasound and microbubbles. *Mol Pharm*. 2011;8:799–806.
38. Bulner S, Prodeus A, Gariepy J, Hynynen K, Goertz DE. Enhancing Checkpoint Inhibitor Therapy with Ultrasound Stimulated Microbubbles. *Ultrasound Med Biol*. 2019;45:500–512.
39. Meng Y, Reilly RM, Pezo RC, Trudeau M, Sahgal A, Singnurkar A, Perry J, Myrehaug S, Pople CB, Davidson B, Llinas M, Hyen C, Huang Y, Hamani C, Suppiah S, Hynynen K, Lipsman N. MR-guided focused ultrasound enhances delivery of trastuzumab to Her2-positive brain metastases. *Sci Transl Med*. 2021;13.
40. Kopechek JA, Carson AR, McTiernan CF, Chen X, Hasjim B, Lavery L, Sen M, Grandis JR, Villanueva FS. Ultrasound targeted microbubble destruction-mediated delivery of a

transcription factor decoy inhibits STAT3 signaling and tumor growth. *Theranostics*. 2015;5:1378–1387.
41. Lentacker I, De Smedt SC, Sanders NN. Drug loaded microbubble design for ultrasound triggered delivery. *Soft Matter*. 2009;5:2161–2170.
42. Carson AR, McTiernan CF, Lavery L, Grata M, Leng X, Wang J, Chen X, Villanueva FS. Ultrasound-targeted microbubble destruction to deliver siRNA cancer therapy. *Cancer Res*. 2012;72:6191–6199.
43. Jones RM, McMahon D, Hynynen K. Ultrafast three-dimensional microbubble imaging in vivo predicts tissue damage volume distributions during nonthermal brain ablation. *Theranostics*. 2020;10:7211–7230.
44. Aycock KN, Davalos R V. Irreversible Electroporation: Background, Theory, and Review of Recent Developments in Clinical Oncology. *Bioelectricity*. 2019;1:214–234.
45. Schwan HP. Electrical properties of tissue and cell suspensions. *Adv Biol Med Phys*. 1957;5:147–209.
46. Teissié J, Rols MP. An experimental evaluation of the critical potential difference inducing cell membrane electropermeabilization. *Biophys J*. 1993;65:409–413.
47. Gehl J. Electroporation: Theory and methods, perspectives for drug delivery, gene therapy and research. *Acta Physiol Scand*. 2003;177:437–447.
48. Shil P, Bidaye S, Vidyasagar PB. Analysing the effects of surface distribution of pores in cell electroporation for a cell membrane containing cholesterol. *J Phys D Appl Phys*. 2008;41. doi:10.1088/0022-3727/41/5/055502.
49. Krassowska W, Filev PD. Modeling electroporation in a single cell. *Biophys J*. 2007;92:404–417.
50. Kotnik T, Rems L, Tarek M, Miklavcic D. Membrane Electroporation and Electropermeabilization: Mechanisms and Models. *Annu Rev Biophys*. 2019;48:63–91.
51. Frandsen SK, Vissing M, Gehl J. A comprehensive review of calcium electroporation —A novel cancer treatment modality. *Cancers (Basel)*. 2020;12:1–21.
52. Teixeira M, Py BF, Bosc C, Laubreton D, Moutin MJ, Marvel J, Flamant F, Markossian S. Electroporation of mice zygotes with dual guide RNA/Cas9 complexes for simple and efficient cloning-free genome editing. *Sci Rep*. 2018;8:1–9.
53. Aslan H, Zilberman Y, Arbeli V, Sheyn D, Matan Y, Liebergall M, Li JZ, Helm GA, Gazit D, Gazit Z. Nucleofection-based Ex vivo nonviral gene delivery to human stem cells as a platform for tissue regeneration. *Tissue Eng*. 2006;12:877–889.
54. Chicaybam L, Abdo L, Viegas M, Marques LVC, de Sousa P, Batista-Silva LR, Alves-Monteiro V, Bonecker S, Monte-Mór B, Bonamino MH. Transposon-mediated generation of CAR-T cells shows efficient anti B-cell leukemia response after ex vivo expansion. *Gene Ther*. 2020;27:85–95.
55. Lizano C, Sanz S, Luque J, Pinilla M. In vitro study of alcohol dehydrogenase and acetaldehyde dehydrogenase encapsulated into human erythrocytes by an electroporation procedure. *Biochim Biophys Acta - Gen Subj*. 1998;1425:328–336.
56. Heller R, Jaroszeski M, Atkin A, Moradpour D, Gilbert R, Wands J, Nicolau C. In vivo gene electroinjection and expression in rat liver. *FEBS Lett*. 1996;389:225–228.
57. Fang Z, Chen L, Moser MAJ, Zhang W, Qin Z, Zhang B. Electroporation-Based Therapy for Brain Tumors: A Review. *J Biomech Eng*. 2021;143. doi:10.1115/1.4051184.
58. Maor E, Ivorra A, Leor J, Rubinsky B. The effect of irreversible electroporation on blood vessels. *Technol Cancer Res Treat*. 2007;6:307–312.

59. Lee JM, Choi HS, Chun HJ, Kim ES, Keum B, Seo YS, Jeen YT, Lee HS, Um SH, Kim CD, Kim HB. EUS-guided irreversible electroporation using endoscopic needle-electrode in porcine pancreas. *Surg Endosc*. 2019;33:658–662.
60. Rubinsky J, Onik G, Mikus P, Rubinsky B. Optimal Parameters for the Destruction of Prostate Cancer Using Irreversible Electroporation. *J Urol*. 2008;180:2668–2674.
61. Stevenson DJ, Gunn-Moore FJ, Campbell P, Dholakia K. Single cell optical transfection. *J R Soc Interface*. 2010;7:863–871.
62. Schneckenburger H. Laser-assisted optoporation of cells and tissues – a mini-review. *Biomed Opt Express*. 2019;10:2883.
63. Peng Q, Juzeniene A, Chen J, Svaasand LO, Warloe T, Giercksky KE, Moan J. Lasers in medicine. *Reports Prog Phys*. 2008;71. doi:10.1088/0034-4885/71/5/056701.
64. Vogel A, Noack J, Hüttman G, Paltauf G. Mechanisms of femtosecond laser nanosurgery of cells and tissues. *Appl Phys B Lasers Opt*. 2005;81:1015–1047.
65. Soughayer JS, Krasieva T, Jacobson SC, Ramsey JM, Tromberg BJ, Allbritton NL. Characterization of cellular optoporation with distance. *Anal Chem*. 2000;72:1342–1347.
66. Fan Q, Hu W, Ohta AT. Efficient single-cell poration by microsecond laser pulses. *Lab Chip*. 2015;15:581–588.
67. Tsukakoshi M, Kurata S, Nomiya Y, Ikawa Y, Kasuya T. A novel method of DNA transfection by laser microbeam cell surgery. *Appl Phys B Photophysics Laser Chem*. 1984;35:135–140.
68. Lei M, Xu H, Yang H, Yao B. Femtosecond laser-assisted microinjection into living neurons. *J Neurosci Methods*. 2008;174:215–218.
69. Uchugonova A, König K, Bueckle R, Isemann A, Tempea G. Targeted transfection of stem cells with sub-20 femtosecond laser pulses. *Opt Express*. 2008;16:9357.
70. Bergeron E, Boutopoulos C, Martel R, Torres A, Rodriguez C, Niskanen J, Lebrun JJ, Winnik FM, Sapieha P, Meunier M. Cell-specific optoporation with near-infrared ultrafast laser and functionalized gold nanoparticles. *Nanoscale*. 2015;7:17836–17847.
71. Benjamin EJ, Virani SS, Callaway CW, Chamberlain AM, Chang AR, Cheng S, Chiuve SE, Cushman M, Delling FN, Deo R, De Ferranti SD, Ferguson JF, Fornage M, Gillespie C, Isasi CR, Jiménez MC, Jordan LC, Judd SE, Lackland D, Lichtman JH, Lisabeth L, Liu S, Longenecker CT, Lutsey PL, MacKey JS, Matchar DB, Matsushita K, Mussolino ME, Nasir K, O'Flaherty M, Palaniappan LP, Pandey A, Pandey DK, Reeves MJ, Ritchey MD, Rodriguez CJ, Roth GA, Rosamond WD, Sampson UKA, Satou GM, Shah SH, Spartano NL, Tirschwell DL, Tsao CW, Voeks JH, Willey JZ, Wilkins JT, Wu JHY, Alger HM, Wong SS, Muntner P. Heart disease and stroke statistics - 2018 update: A report from the American Heart Association. ; 2018: 1-67–492. doi:10.1161/CIR.0000000000000558.
72. Cohn PF. Treatment of chronic myocardial ischemia: Rationale and treatment options. *Cardiovasc Drugs Ther*. 1998;12:217–223.
73. Kühn F, Schiergens TS, Klar E. Acute Mesenteric Ischemia. *Visc Med*. 2020;36:256–263.
74. Kalogeris T, Baines CP, Krenz M, Korthuis RJ. Cell Biology of Ischemia/Reperfusion Injury, 1st ed. Elsevier Inc.; 2012: 1-229–317. doi:10.1016/B978-0-12-394309-5.00006-7.
75. Ibanez B, James S, Agewall S, Antunes MJ, Bucciarelli-Ducci C, Bueno H, Caforio ALP, Crea F, Goudevenos JA, Halvorsen S, Hindricks G, Kastrati A, Lenzen MJ, Prescott E, Roffi M, Valgimigli M, Varenhorst C, Vranckx P, Widimský P, Baumbach A, Bugiardini R, Coman IM, Delgado V, Fitzsimons D, Gaemperli O, Gershlick AH, Gielen S, Harjola VP, Katus HA, Knuuti J, Kolh P, Leclercq C, Lip GYH, Morais J, Neskovic AN,

Neumann FJ, Niessner A, Piepoli MF, Richter DJ, Shlyakhto E, Simpson IA, Steg PG, Terkelsen CJ, Thygesen K, Windecker S, Zamorano JL, Zeymer U, Chettibi M, Hayrapetyan HG, Metzler B, Ibrahimov F, Sujayeva V, Beauloye C, Dizdarevic-Hudic L, Karamfiloff K, Skoric B, Antoniades L, Tousek P, Shaheen SM, Marandi T, Niemel€a M, Kedev S, Gilard M, Aladashvili A, Elsaesser A, Kanakakis IG, Merkely B, Gudnason T, Iakobishvili Z, Bolognese L, Berkinbayev S, Bajraktari G, Beishenkulov M, Zake I, Lamin H Ben, Gustiene O, Pereira B, Xuereb RG, Ztot S, Juliebø V, Legutko J, Timoteo AT, Tatu-Chit¸oiu G, Yakovlev A, Bertelli L, Nedeljkovic M, Studencan M, Bunc M, de Castro AMG, Petursson P, Jeger R, Mourali MS, Yildirir A, Parkhomenko A, Gale CP. 2017 ESC Guidelines for the management of acute myocardial infarction in patients presenting with ST-segment elevation. *Eur Heart J*. 2018;39:119–177.

76. Powers WJ, Rabinstein AA, Ackerson T, Adeoye OM, Bambakidis NC, Becker K, Biller J, Brown M, Demaerschalk BM, Hoh B, Jauch EC, Kidwell CS, Leslie-Mazwi TM, Ovbiagele B, Scott PA, Sheth KN, Southerland AM, Summers D V., Tirschwell DL. 2018 Guidelines for the Early Management of Patients With Acute Ischemic Stroke: A Guideline for Healthcare Professionals From the American Heart Association/American Stroke Association. ; 2018: 1-46–110. doi:10.1161/STR.0000000000000158.
77. Annex BH, Cooke JP. New Directions in Therapeutic Angiogenesis and Arteriogenesis in Peripheral Arterial Disease. *Circ Res*. 2021;128:1944–1957.
78. Acosta S. Epidemiology of mesenteric vascular disease: Clinical implications. *Semin Vasc Surg*. 2010;23:4–8.
79. Libby P. The changing landscape of atherosclerosis. *Nature*. 2021;592:524–533.
80. Schober A, Nazari-Jahantigh M, Wei Y, Bidzhekov K, Gremse F, Grommes J, Megens RTA, Heyll K, Noels H, Hristov M, Wang S, Kiessling F, Olson EN, Weber C. MicroRNA-126-5p promotes endothelial proliferation and limits atherosclerosis by suppressing Dlk1. *Nat Med*. 2014;20:368–376.
81. Stettler C, Wandel S, Allemann S, Kastrati A, Morice MC, Schömig A, Pfisterer ME, Stone GW, Leon MB, de Lezo JS, Goy JJ, Park SJ, Sabaté M, Suttorp MJ, Kelbaek H, Spaulding C, Menichelli M, Vermeersch P, Dirksen MT, Cervinka P, Petronio AS, Nordmann AJ, Diem P, Meier B, Zwahlen M, Reichenbach S, Trelle S, Windecker S, Jüni P. Outcomes associated with drug-eluting and bare-metal stents: a collaborative network meta-analysis. *Lancet*. 2007;370:937–948.
82. Hitchcock KE, Holland CK. Ultrasound-assisted thrombolysis for stroke therapy: Better thrombus break-up with bubbles. *Stroke*. 2010;41:50–53.
83. Sedighiani F, Nikol S. Gene therapy in vascular disease. *Surgeon*. 2011;9:326–335.
84. Ridker PM, Lüscher TF. Anti-inflammatory therapies for cardiovascular disease. *Eur Heart J*. 2014;35:1782–1791.
85. Moroz E, Carlin S, Dyomina K, Burke S, Thaler HT, Blasberg R, Serganova I. Real-time imaging of HIF-1α stabilization and degredation. *PLoS One*. 2009;4. doi:10.1371/journal.pone.0005077.
86. Pouysségur J, Daya F, Mazure NM. Hypoxia signalling in cancer and approaches to enforce tumor regression. *Nature*. 2006;441:437–443.
87. Geudens I, Gerhardt O. Coordinating cell behaviour during blood vessel formation. *Development*. 2011;138:4569–4583.
88. Ribatti D, Crivellato E. “Sprouting angiogenesis”, a reappraisal. *Dev Biol*. 2012;372:157–165.

89. Blanco R, Gerhardt H. VEGF and Notch in tip and stalk cell selection. *Cold Spring Harb Perspect Med*. 2013;3:1–19.
90. Welti J, Loges S, Dimmeler S, Carmeliet P. Recent molecular discoveries in angiogenesis and antiangiogenic therapies in cancer. *J Clin Invest*. 2013;123:3190–3200.
91. Liu ZL, Chen HH, Zheng LL, Sun LP, Shi L. Angiogenic signaling pathways and anti-angiogenic therapy for cancer. *Signal Transduct Target Ther*. 2023;8:1–39.
92. Adair T, Montani J. Chapter 1: Overview of Angiogenesis. San Rafael, CA: Morgan & Claypool Life Sciences; 2010: 1-1–9.
93. Bischoff J, Editor G, Interactions EP. Endothelial / Pericyte Interactions. 2005;:512–523.
94. Madanecki P, Kapoor N, Bebok Z, Ochocka R, Collawn JF, Bartoszewski R. Regulation of angiogenesis by hypoxia: the role of microRNA. *Cell Mol Biol Lett*. 2013;18:47–57.
95. Harris TA, Yamakuchi M, Ferlito M, Mendell JT, Lowenstein CJ. MicroRNA-126 regulates endothelial expression of vascular cell adhesion molecule 1. *Proc Natl Acad Sci U S A*. 2008;105:1516–1521.
96. Fish JE, Santoro MM, Morton SU, Yu S, Yeh RF, Wythe JD, Ivey KN, Bruneau BG, Stainier DYR, Srivastava D. miR-126 Regulates Angiogenic Signaling and Vascular Integrity. *Dev Cell*. 2008;15:272–284.
97. Lu Z, Xu S. ERK1/2 MAP kinases in cell survival and apoptosis. *IUBMB Life*. 2006;58:621–631.
98. Fry EA, Mallakin A, Inoue K. Translocations involving ETS family proteins in human cancer. *Integr Cancer Sci Ther*. 2018;5:1–26.
99. Vial E, Sahai E, Marshall CJ. ERK-MAPK signaling coordinately regulates activity of Rac1 and RhoA for tumor cell motility. *Cancer Cell*. 2003;4:67–79.
100. Saxton RA, Sabatini DM. mTOR Signaling in Growth, Metabolism, and Disease. *Cell*. 2017;168:960–976.
101. Fulton D, Gratton J, Mccabe TJ, Fontana J, Fujio Y, Walsh K, Franke TF, Papapetropoulos A, Sessa WC. Regulation of endothelium-derived NO production by the protein kinase Akt. *Lett to Nat*. 1999;399:597–601.
102. Bartel DP. MicroRNAs: Target Recognition and Regulatory Functions. *Cell*. 2009;136:215–233.
103. Ambros V, Chen X. The regulation of genes and genomes by small RNAs. *Development*. 2007;134:1635–1641.
104. Lam JKW, Chow MYT, Zhang Y, Leung SWS. siRNA versus miRNA as therapeutics for gene silencing. *Mol Ther - Nucleic Acids*. 2015;4:e252.
105. He L, Hannon GJ. MicroRNAs: Small RNAs with a big role in gene regulation. *Nat Rev Genet*. 2004;5:522–531.
106. Tang S tao, Wang F, Shao M, Wang Y, Zhu H qing. MicroRNA-126 suppresses inflammation in endothelial cells under hyperglycemic condition by targeting HMGB1. *Vascul Pharmacol*. 2017;88:48–55.
107. Alique M, Bodega G, Giannarelli C, Carracedo J, Ramírez R. MicroRNA-126 regulates Hypoxia-Inducible Factor-1α which inhibited migration, proliferation, and angiogenesis in replicative endothelial senescence. *Sci Rep*. 2019;9:1–19.
108. Zhu N, Zhang D, Xie H, Zhou Z, Chen H, Hu T, Bai Y, Shen Y, Yuan W, Jing Q, Qin Y. Endothelial-specific intron-derived miR-126 is down-regulated in human breast cancer and targets both VEGFA and PIK3R2. *Mol Cell Biochem*. 2011;351:157–164.
109. Peruzzi G, Sinibaldi G, Silvani G, Ruocco G, Casciola CM. Perspectives on cavitation

enhanced endothelial layer permeability. *Colloids Surfaces B Biointerfaces*. 2018;168:83–93.
110. Apfel RE, Holland CK. Gauging the likelihood of cavitation from short-pulse low duty cycle diagnostic ultrasound. *Ultrasound Med Biol*. 1991;17:179–1991.
111. Şen T, Tüfekçioğlu O, Koza Y. Mechanical index. *Anatol J Cardiol*. 2015;15:334–336.
112. Yoo K, Walker WR, Williams R, Tremblay-Darveau C, Burns PN, Sheeran PS. Impact of Encapsulation on in vitro and in vivo Performance of Volatile Nanoscale Phase-Shift Perfluorocarbon Droplets. *Ultrasound Med Biol*. 2018;44:1836–1852.
113. Sirsi, Shashank R., Borden M. Microbubble Compositions, Properties and Biomedical Applications. *Bubble Sci Eng Technol*. 2010;1:3–17.
114. Lentacker I, De Cock I, Deckers R, De Smedt SC, Moonen CTW. Understanding ultrasound induced sonoporation: Definitions and underlying mechanisms. *Adv Drug Deliv Rev*. 2014;72:49–64.
115. Helfield B, Chen X, Watkins SC, Villanueva FS. Transendothelial Perforations and the Sphere of Influence of Single-Site Sonoporation. *Ultrasound Med Biol*. 2020;46:1686–1697.
116. Sheikov N, McDannold N, Vykhodtseva N, Jolesz F, Hynynen K. Cellular mechanisms of the blood-brain barrier opening induced by ultrasound in presence of microbubbles. *Ultrasound Med Biol*. 2004;30:979–989.
117. Pandit R, Koh WK, Sullivan RKP, Palliyaguru T, Parton RG, Götz J. Role for caveolin-mediated transcytosis in facilitating transport of large cargoes into the brain via ultrasound. *J Control Release*. 2020;327:667–675.
118. Endo-takahashi Y. Microbubbles and Nanobubbles with Ultrasound for Systemic Gene Delivery. 2020;:1–14.
119. Lantheus Medical Imaging. Definity: Perflutren Lipid Microspheres. *U S Food Drug Adm*. 2011;:1–18.
120. GE Healthcare. A Step-by-Step Quick Reference Guide Imaging With Optison™ Ultrasound Enhancing Agent. ; 2022.
121. Bracco. SonoVue® Sulfur Hexafluoride. ; 2004: 1-24.
122. Upadhyay A, Dalvi S V. Microbubble Formulations: Synthesis, Stability, Modeling and Biomedical Applications. *Ultrasound Med Biol*. 2019;45:301–343.
123. Klibanov AL. Microbubble contrast agents: Targeted ultrasound imaging and ultrasound-assisted drug-delivery applications. *Invest Radiol*. 2006;41:354–362.
124. Pochon S, Tardy I, Bussat P, Bettinger T, Brochot J, Von Wronski M, Passantino L, Schneider M. BR55: A lipopeptide-based VEGFR2-targeted ultrasound contrast agent for molecular imaging of angiogenesis. *Invest Radiol*. 2010;45:89–95.
125. Smeenge M, Tranquart F, Mannaerts CK, De Reijke TM, Van De Vijver MJ, Laguna MP, Pochon S, De La Rosette JJMCH, Wijkstra H. First-in-human ultrasound molecular imaging with a VEGFR2-specific ultrasound molecular contrast agent (BR55) in prostate cancer a safety and feasibility pilot study. *Invest Radiol*. 2017;52:419–427.
126. Payen T, Dizeux A, Baldini C, Le Guillou-Buffello D, Lamuraglia M, Comperat E, Lucidarme O, Bridal SL. VEGFR2-Targeted Contrast-Enhanced Ultrasound to Distinguish between Two Anti-Angiogenic Treatments. *Ultrasound Med Biol*. 2015;41:2202–2211.
127. Roovers S, Lajoinie G, De Cock I, Brans T, Dewitte H, Braeckmans K, Versuis M, De Smedt SC, Lentacker I. Sonoprinting of nanoparticle-loaded microbubbles: Unraveling the

multi-timescale mechanism. *Biomaterials*. 2019;217:119250.
128. Carson AR, McTiernan CF, Lavery L, Grata M, Leng X, Wang J, Chen X, Villanueva FS. Ultrasound-targeted microbubble destruction to deliver siRNA cancer therapy. *Cancer Res*. 2012;72:6191–6199.
129. Li Y, Du M, Fang J, Zhou J, Chen Z. UTMD promoted local delivery of miR-34a-mimic for ovarian cancer therapy. *Drug Deliv*. 2021;28:1616–1625.
130. Cao WJ, Rosenblat JD, Roth NC, Kuliszewski MA, Matkar PN, Rudenko D, Liao C, Lee PJH, Leong-Poi H. Therapeutic Angiogenesis by Ultrasound-Mediated MicroRNA-126-3p Delivery. *Arterioscler Thromb Vasc Biol*. 2015;35:2401–2411.
131. Christiansen JP, French BA, Klibanov AL, Kaul S, Lindner JR. Targeted tissue transfection with ultrasound destruction of plasmid-bearing cationic microbubbles. *Ultrasound Med Biol*. 2003;29:1759–1767.
132. Wang DS, Panje C, Pysz MA, Paulmurugan R, Rosenberg J, Gambhir SS, Schneider M, Willmann JK. Cationic versus neutral microbubbles for ultrasound-mediated gene delivery in cancer. *Radiology*. 2012;264:721–732.
133. Lyon PC, Gray MD, Mannaris C, Folkes LK, Stratford M, Campo L, Chung DYF, Scott S, Anderson M, Goldin R, Carlisle R, Wu F, Middleton MR, Gleeson F V., Coussios CC. Safety and feasibility of ultrasound-triggered targeted drug delivery of doxorubicin from thermosensitive liposomes in liver tumours (TARDOX): a single-centre, open-label, phase 1 trial. *Lancet Oncol*. 2018;19:1027–1039.
134. Lindner JR. Contrast ultrasound molecular imaging of inflammation in cardiovascular disease. *Cardiovasc Res*. 2009;84:182–189.
135. Luan Y, Lajoinie G, Gelderblom E, Skachkov I, van der Steen AFW, Vos HJ, Versluis M, De Jong N. Lipid shedding from single oscillating microbubbles. *Ultrasound Med Biol*. 2014;40:1834–1846.
136. Beekers I, Mastik F, Beurskens R, Tang PY, Vegter M, van der Steen AFW, de Jong N, Verweij MD, Kooiman K. High-Resolution Imaging of Intracellular Calcium Fluctuations Caused by Oscillating Microbubbles. *Ultrasound Med Biol*. 2020;46:2017–2029.
137. De Cock I, Zagato E, Braeckmans K, Luan Y, de Jong N, De Smedt SC, Lentacker I. Ultrasound and microbubble mediated drug delivery: acoustic pressure as determinant for uptake via membrane pores or endocytosis. *J Control Release*. 2015;197:20–28.
138. Yu GZ, Istvanic F, Chen X, Nouraie M, Shiva S, Straub AC, Pacella JJ. Ultrasound-Targeted Microbubble Cavitation with Sodium Nitrite Synergistically Enhances Nitric Oxide Production and Microvascular Perfusion. *Ultrasound Med Biol*. 2020;46:667–678.
139. Belcik JT, Davidson BP, Xie A, Wu MD, Yadava M, Qi Y, Liang S, Chon CR, Ammi AY, Field J, Harmann L, Chilian WM, Linden J, Lindner JR. Augmentation of Muscle Blood Flow by Ultrasound Cavitation Is Mediated by ATP and Purinergic Signaling. *Circulation*. 2017;135:1240–1252.
140. Datta S, Coussios CC, Ammi AY, Mast TD, de Courten-Myers GM, Holland CK. Ultrasound-Enhanced Thrombolysis Using Definity® as a Cavitation Nucleation Agent. *Ultrasound Med Biol*. 2008;34:1421–1433.
141. Guan L, Wang C, Yan X, Liu L, Li Y, Mu Y. A thrombolytic therapy using diagnostic ultrasound combined with RGDS-targeted microbubbles and urokinase in a rabbit model. *Sci Rep*. 2020;10:1–13.
142. Wright C, Hynynen K, Goertz D. In vitro and in vivo high-intensity focused ultrasound thrombolysis. *Invest Radiol*. 2012;47:217–225.

143. Juffermans LJM, van Dijk A, Jongenelen CAM, Drukarch B, Reijerkerk A, de Vries HE, Kamp O, Musters RJP. Ultrasound and Microbubble-Induced Intra- and Intercellular Bioeffects in Primary Endothelial Cells. *Ultrasound Med Biol*. 2009;35:1917–1927.
144. Wu D, Chen Q, Chen X, Han F, Chen Z, Wang Y. The blood–brain barrier: structure, regulation, and drug delivery. *Signal Transduct Target Ther*. 2023;8. doi:10.1038/s41392-023-01481-w.
145. Stamatovic SM, Johnson AM, Keep RF, Andjelkovic A V. Junctional proteins of the blood-brain barrier: New insights into function and dysfunction. *Tissue Barriers*. 2016;4:1–12.
146. Kadry H, Noorani B, Cucullo L. A blood–brain barrier overview on structure, function, impairment, and biomarkers of integrity. *Fluids Barriers CNS*. 2020;17:1–24.
147. Mainprize T, Lipsman N, Huang Y, Meng Y, Bethune A, Ironside S, Heyn C, Alkins R, Trudeau M, Sahgal A, Perry J, Hynynen K. Blood-Brain Barrier Opening in Primary Brain Tumors with Non-invasive MR-Guided Focused Ultrasound: A Clinical Safety and Feasibility Study. *Sci Rep*. 2019;9:1–7.
148. Carpentier A, Stupp R, Sonabend AM, Dufour H, Chinot O, Mathon B, Ducray F, Guyotat J, Baize N, Menei P, de Groot J, Weinberg JS, Liu BP, Guemas E, Desseaux C, Schmitt C, Bouchoux G, Canney M, Idbaih A. Repeated blood–brain barrier opening with a nine-emitter implantable ultrasound device in combination with carboplatin in recurrent glioblastoma: a phase I/II clinical trial. *Nat Commun*. 2024;15:1–12.
149. O'Reilly MA, Hough O, Hynynen K. Blood-Brain Barrier Closure Time After Controlled Ultrasound-Induced Opening. *J Ultrasound Med*. 2017;36:475–483.
150. Timbie KF, Mead BP, Price RJ. Drug and gene delivery across the blood-brain barrier with focused ultrasound. *J Control Release*. 2015;219:61–75.
151. Burgess A, Ayala-Grosso CA, Ganguly M, Jordão JF, Aubert I, Hynynen K. Targeted delivery of neural stem cells to the brain using MRI-guided focused ultrasound to disrupt the blood-brain barrier. *PLoS One*. 2011;6. doi:10.1371/journal.pone.0027877.
152. White E, Myhre S, Serafini MR, Broad M, Chesnut A, Browning M, Heishman D, Knupp J, Chao JC. 2024 State of the Field. ; 2024: 1-429.
153. Zhou B, Lian Q, Jin C, Lu J, Xu L, Gong X, Zhou P. Human clinical trial using diagnostic ultrasound and microbubbles to enhance neoadjuvant chemotherapy in HER2- negative breast cancer. *Front Oncol*. 2022;12:1–11.
154. Hsu PH, Lin YT, Chung YH, Lin KJ, Yang LY, Yen TC, Liu HL. Focused Ultrasound-Induced Blood-Brain Barrier Opening Enhances GSK-3 Inhibitor Delivery for Amyloid-Beta Plaque Reduction. *Sci Rep*. 2018;8:1–9.
155. Lipsman N, Meng Y, Bethune AJ, Huang Y, Lam B, Masellis M, Herrmann N, Heyn C, Aubert I, Boutet A, Smith GS, Hynynen K, Black SE. Blood–brain barrier opening in Alzheimer's disease using MR-guided focused ultrasound. *Nat Commun*. 2018;9:1–8.
156. Elias WJ, Lipsman N, Ondo WG, Ghanouni P, Kim YG, Lee W, Schwartz M, Hynynen K, Lozano AM, Shah BB, Huss D, Dallapiazza RF, Gwinn R, Witt J, Ro S, Eisenberg HM, Fishman PS, Gandhi D, Halpern CH, Chuang R, Butts Pauly K, Tierney TS, Hayes MT, Cosgrove GR, Yamaguchi T, Abe K, Taira T, Chang JW. A Randomized Trial of Focused Ultrasound Thalamotomy for Essential Tremor. *N Engl J Med*. 2016;375:730–739.
157. Bond AE, Shah BB, Huss DS, Dallapiazza RF, Warren A, Harrison MB, Sperling SA, Wang XQ, Gwinn R, Witt J, Ro S, Elias WJ. Safety and efficacy of focused ultrasound

thalamotomy for patients with medication-refractory, tremor-dominant Parkinson disease a randomized Clinical trial. *JAMA Neurol*. 2017;74:1412–1418.
158. Jung HH, Kim SJ, Roh D, Chang JG, Chang WS, Kweon EJ, Kim CH, Chang JW. Bilateral thermal capsulotomy with MR-guided focused ultrasound for patients with treatment-refractory obsessive-compulsive disorder: A proof-of-concept study. *Mol Psychiatry*. 2015;20:1205–1211.
159. Meng Y, Pople CB, Suppiah S, Llinas M, Huang Y, Sahgal A, Perry J, Keith J, Davidson B, Hamani C, Amemiya Y, Seth A, Leong H, Heyn CC, Aubert I, Hynynen K, Lipsman N. MR-guided focused ultrasound liquid biopsy enriches circulating biomarkers in patients with brain tumors. *Neuro Oncol*. 2021;23:1789–1797.
160. El Kadi S, Porter TR, Zanstra M, Siegers A, van Loon RB, Hopman LHGA, van Rossum AC, Kamp O. Feasibility of sonothrombolysis in the ambulance for ST-elevation myocardial infarction. *Int J Cardiovasc Imaging*. 2022;38:1089–1098.
161. Cannatà A, Ali H, Sinagra G, Giacca M. Gene Therapy for the Heart Lessons Learned and Future Perspectives. *Circ Res*. 2020;126:1394–1414.
162. Goswami R, Subramanian G, Silayeva L, Newkirk I, Doctor D, Chawla K, Chattopadhyay S, Chandra D, Chilukuri N, Betapudi V. Gene therapy leaves a vicious cycle. *Front Oncol*. 2019;9:1–25.
163. Lee RC. The C . elegans Heterochronic Gene lin-4 Encodes Small RNAs with Antisense Complementarity to & II-14. 1993;75:843–854.
164. Chen W, Hu Y, Ju D. Gene therapy for neurodegenerative disorders : advances , insights and prospects. *Acta Pharm Sin B*. 2020;10:1347–1359.
165. Forterre A, Komuro H, Aminova S, Harada M. A comprehensive review of cancer microRNA therapeutic delivery strategies. Cancers (Basel). . 2020;12:1–21.
166. Kalayinia S, Arjmand F, Maleki M, Malakootian M, Singh CP. MicroRNAs: roles in cardiovascular development and disease. *Cardiovasc Pathol*. 2021;50:107296.
167. Management N. Copyright © 2022 Wolters Kluwer Health , Inc . All rights reserved . Copyright © 2022 Wolters Kluwer Health , Inc . All rights reserved . *J Hypertens*. 2022;37:107–108.
168. Rawat M, Kadian K, Gupta Y, Kumar A, Chain PSG, Kovbasnjuk O, Kumar S, Parasher G. MicroRNA in pancreatic cancer: From biology to therapeutic potential. *Genes (Basel)*. 2019;10. doi:10.3390/genes10100752.
169. Imani S, Wu RC, Fu J. MicroRNA-34 family in breast cancer: From research to therapeutic potential. *J Cancer*. 2018;9:3765–3775.
170. Iqbal MA, Arora S, Prakasam G, Calin GA, Syed MA. MicroRNA in lung cancer: role, mechanisms, pathways and therapeutic relevance. *Mol Aspects Med*. 2019;70:3–20.
171. Balatti V, Croce CM. MicroRNA dysregulation and multi-targeted therapy for cancer treatment. *Adv Biol Regul*. 2020;75:100669.
172. Karakikes I, Chaanine AH, Kang S, Mukete BN, Jeong D, Zhang S, Hajjar RJ, Lebeche D. Therapeutic cardiac-targeted delivery of miR-1 reverses pressure overload-induced cardiac hypertrophy and attenuates pathological remodeling. *J Am Heart Assoc*. 2013;2:17–19.
173. Cheng WL, Kao YH, Chao TF, Lin YK, Chen SA, Chen YJ. MicroRNA-133 suppresses ZFHX3-dependent atrial remodelling and arrhythmia. *Acta Physiol*. 2019;227:1–16.
174. Li PF, He RH, Shi SB, Li R, Wang QT, Rao GT, Yang B. Modulation of miR-10a-mediated TGF-β1/Smads signaling affects atrial fibrillation-induced cardiac fibrosis and

cardiac fibroblast proliferation. *Biosci Rep*. 2019;39:1–12.
175. Song N, Zhang T, Xu XL, Lu Z, Yu X, Fang Y, Hu J, Jia P, Teng J, Ding X. miR-21 protects against ischemia/reperfusion-induced acute kidney injury by preventing epithelial cell apoptosis and inhibiting dendritic cell maturation. *Front Physiol*. 2018;9:1–14.
176. Xiao ZH, Wang L, Gan P, He J, Yan BC, Ding LD. Dynamic Changes in miR-126 Expression in the Hippocampus and Penumbra Following Experimental Transient Global and Focal Cerebral Ischemia–Reperfusion. *Neurochem Res*. 2020;45:1107–1119.
177. Qu M, Pan J, Wang L, Zhou P, Song Y, Wang S, Jiang L, Geng J, Zhang Z, Wang Y, Tang Y, Yang GY. MicroRNA-126 Regulates Angiogenesis and Neurogenesis in a Mouse Model of Focal Cerebral Ischemia. *Mol Ther - Nucleic Acids*. 2019;16:15–25.
178. Chen HH, Matkar PN, Afrasiabi K, Kuliszewski MA, Leong-Poi H. Prospect of ultrasound-mediated gene delivery in cardiovascular applications. *Expert Opin Biol Ther*. 2016;16:815–826.
179. Yusefi H, Helfield B. Ultrasound Contrast Imaging : Fundamentals and Emerging Technology. *Front Phys*. 2022;10:1–16.
180. He S, Singh D, Helfield B. An Overview of Cell Membrane Perforation and Resealing Mechanisms for Localized Drug Delivery. *Pharmaceutics*. 2022;14:1–20.
181. Kooiman K, Roovers S, Langeveld SAG, Kleven RT, Dewitte H, O'Reilly MA, Escoffre JM, Bouakaz A, Verweij MD, Hynynen K, Lentacker I, Stride E, Holland CK. Ultrasound-Responsive Cavitation Nuclei for Therapy and Drug Delivery. *Ultrasound Med Biol*. 2020;46:1296–1325.
182. Qin P, Han T, Yu ACH, Xu L. Mechanistic understanding the bioeffects of ultrasound-driven microbubbles to enhance macromolecule delivery. *J Control Release*. 2018;272:169–181.
183. Hernot S, Klibanov AL. Microbubbles in ultrasound-triggered drug and gene delivery. *Adv Drug Deliv Rev*. 2008;60:1153–1166.
184. Zhou Q, Deng Q, Hu BO, Wang YJ, Chen JL, Cui JJ, Cao S, Song HN. Ultrasound combined with targeted cationic microbubble-mediated angiogenesis gene transfection improves ischemic heart function. *Exp Ther Med*. 2017;13:2293–2303.
185. Schwartz MR, Debski AC, Price RJ. Ultrasound-targeted nucleic acid delivery for solid tumor therapy. *J Control Release*. 2021;339:531–546.
186. Leighton TG. The acoustic bubble. London: Academic Press; 1994.
187. Wischhusen JC, Chowdhury SM, Lee T, Wang H, Bachawal S, Devulapally R, Afjei R, Sukumar UK, Paulmurugan R. Ultrasound-mediated delivery of miRNA-122 and anti-miRNA-21 therapeutically immunomodulates murine hepatocellular carcinoma in vivo. *J Control Release*. 2020;321:272–284.
188. Kopechek JA, McTiernan CF, Chen X, Zhu J, Mburu M, Feroze R, Whitehurst DA, Lavery L, Cyriac J, Villanueva FS. Ultrasound and microbubble-targeted delivery of a microRNA inhibitor to the heart suppresses cardiac hypertrophy and preserves cardiac function. *Theranostics*. 2019;9:7088–7098.
189. Cao WJ, Rosenblat JD, Roth NC, Kuliszewski MA, Matkar PN, Rudenko D, Liao C, Lee PJH, Leong-Poi H. Therapeutic Angiogenesis by Ultrasound-Mediated MicroRNA-126-3p Delivery. *Arterioscler Thromb Vasc Biol*. 2015;35:2401–2411.
190. Zhou X, Liu H, Pang Y, Wang M, Liu S. UTMD-mediated delivery of miR-21-5p inhibitor suppresses the development of lung cancer. *Tissue Cell*. 2022;74:101719.
191. Li Y, Du M, Fang J, Zhou J, Chen Z. UTMD promoted local delivery of miR-34a-mimic

for ovarian cancer therapy. *Drug Deliv*. 2021;28:1616–1625.
192. Yi L, Chen Y, Jin Q, Deng C, Wu Y, Li H, Liu T, Li Y, Yang Y, Wang J, Lv Q, Zhang L, Xie M. Antagomir-155 Attenuates Acute Cardiac Rejection Using Ultrasound Targeted Microbubbles Destruction. *Adv Healthc Mater*. 2020;9:1–10.
193. van Rooij T, Skachkov I, Beekers I, Lattwein KR, Voorneveld JD, Kokhuis TJA, Bera D, Luan Y, van der Steen AFW, de Jong N, Kooiman K. Viability of endothelial cells after ultrasound-mediated sonoporation: Influence of targeting, oscillation, and displacement of microbubbles. *J Control Release*. 2016;238:197–211.
194. Postema M, Van Wamel A, Lancée CT, De Jong N. Ultrasound-induced encapsulated microbubble phenomena. *Ultrasound Med Biol*. 2004;30:827–840.
195. Lentacker I, De Cock I, Deckers R, De Smedt SC, Moonen CTW. Understanding ultrasound induced sonoporation: Definitions and underlying mechanisms. *Adv Drug Deliv Rev*. 2014;72:49–64.
196. Helfield BL, Huo X, Williams R, Goertz DE. The effect of preactivation vial temperature on the acoustic properties of Definity™. *Ultrasound Med Biol*. 2012;38:1298–305.
197. Petrov A, Tsa A, Puglisi JD. Analysis of RNA by analytical polyacrylamide gel electrophoresis, 1st ed. Elsevier Inc.; 2013: 1-301–313. doi:10.1016/B978-0-12-420037-1.00016-6.
198. Montoya-Zegarra JA, Russo E, Runge P, Jadhav M, Willrodt AH, Stoma S, Nørrelykke SF, Detmar M, Halin C. AutoTube: a novel software for the automated morphometric analysis of vascular networks in tissues. *Angiogenesis*. 2019;22:223–236.
199. Zitnick CL, Dollár P. Edge boxes: Locating object proposals from edges. *Lect Notes Comput Sci (including Subser Lect Notes Artif Intell Lect Notes Bioinformatics)*. 2014;8693 LNCS:391–405.
200. Dollar P, Zitnick CL. Structured forests for fast edge detection. *Proc IEEE Int Conf Comput Vis*. 2013;:1841–1848.
201. Hyvelin JM, Gaud E, Costa M, Helbert A, Bussat P, Bettinger T, Frinking P. Characteristics and Echogenicity of Clinical Ultrasound Contrast Agents: An in Vitro and in Vivo Comparison Study. *J Ultrasound Med*. 2017;36:941–953.
202. Shi WT, Forsberg F. Ultrasonic characterization of the nonlinear properties of contrast microbubbles. *Ultrasound Med Biol*. 2000;26:93–104.
203. Frinking P, Segers T, Luan Y, Tranquart F. Three Decades of Ultrasound Contrast Agents: A Review of the Past, Present and Future Improvements. *Ultrasound Med Biol*. 2020;46:892–908.
204. Kong Z, Wang Y, Zhang Y, Shan W, Wu J, Wang Q. MicroRNA-126 promotes endothelial progenitor cell proliferation and migration ability via the Notch pathway. *Cardiovasc Diagn Ther*. 2020;10:490–499.
205. Schober A, Nazari-Jahantigh M, Wei Y, Bidzhekov K, Gremse F, Grommes J, Megens RTA, Heyll K, Noels H, Hristov M, Wang S, Kiessling F, Olson EN, Weber C. MicroRNA-126-5p promotes endothelial proliferation and limits atherosclerosis by suppressing Dlk1. *Nat Med*. 2014;20:368–376.
206. Zhou F, Jia X, Yang Q, Yang Y, Zhao Y, Fan Y, Yuan X. Targeted delivery of microRNA-126 to vascular endothelial cells: Via REDV peptide modified PEG-trimethyl chitosan. *Biomater Sci*. 2016;4:849–856.
207. Fujii H, Li SH, Wu J, Miyagi Y, Yau TM, Rakowski H, Egashira K, Guo J, Weisel RD, Li RK. Repeated and targeted transfer of angiogenic plasmids into the infarcted rat heart via

ultrasound targeted microbubble destruction enhances cardiac repair. *Eur Heart J*. 2011;32:2075–2084.
208. Kaul S. Myocardial contrast echocardiography - A 25-year retrospective. *Circulation*. 2008;118:291–308.
209. Su J, Wang J, Luo J, Li H. Ultrasound-mediated destruction of vascular endothelial growth factor (VEGF) targeted and paclitaxel loaded microbubbles for inhibition of human breast cancer cell MCF-7 proliferation. *Mol Cell Probes*. 2019;46:101415.
210. Jing Y, Xiu-Juan Z, Hong-Jiao C, Zhi-Kui C, Qing-Fu Q, En-Sheng X, Li-Wu L. Ultrasound-targeted microbubble destruction improved the antiangiogenic effect of Endostar in triple-negative breast carcinoma xenografts. *J Cancer Res Clin Oncol*. 2019;145:1191–1200.
211. Hwang JH, Tu J, Brayman AA, Matula TJ, Crum LA. Correlation between inertial cavitation dose and endothelial cell damage in vivo. *Ultrasound Med Biol*. 2006;32:1611–1619.
212. Hwang JH, Brayman AA, Reidy MA, Matula TJ, Kimmey MB, Crum LA. Vascular effects induced by combined 1-MHz ultrasound and microbubble contrast agent treatments in vivo. *Ultrasound Med Biol*. 2005;31:553–564.
213. Wu Y, Crawford M, Yu B, Mao Y, Nana-Sinkam SP, Lee LJ. MicroRNA delivery by cationic lipoplexes for lung cancer therapy. *Mol Pharm*. 2011;8:1381–1389.
214. Miller DL, Quddus J. Diagnostic ultrasound activation of contrast agent gas bodies induces capillary rupture in mice. *Proc Natl Acad Sci U S A*. 2000;97:10179–10184.
215. Li P, Cao LQ, Dou CY, Armstrong WF, Miller D. Impact of myocardial contrast echocardiography on vascular permeability: An in vivo dose response study of delivery mode, pressure amplitude and contrast dose. *Ultrasound Med Biol*. 2003;29:1341–1349.
216. Price RJ, Skyba DM, Kaul S, Skalak TC. Delivery of colloidal particles and red blood cells to tissue through microvessel ruptures created by targeted microbubble destruction with ultrasound. *Circulation*. 1998;98:1264–1267.
217. El Kaffas A, Czarnota GJ. Biomechanical effects of microbubbles: From radiosensitization to cell death. *Futur Oncol*. 2015;11:1093–1108.
218. Yu FTH, Chen X, Wang J, Qin B, Villanueva FS. Low Intensity Ultrasound Mediated Liposomal Doxorubicin Delivery Using Polymer Microbubbles. *Mol Pharm*. 2016;13:55–64.
219. Luan Y, Lajoinie G, Gelderblom E, Skachkov I, van der Steen AFW, Vos HJ, Versluis M, De Jong N. Lipid shedding from single oscillating microbubbles. *Ultrasound Med Biol*. 2014;40:1834–1846.
220. Fekri F, Delos Santos RC, Karshafian R, Antonescu CN. Ultrasound microbubble treatment enhances clathrin-mediated endocytosis and fluid-phase uptake through distinct mechanisms. *PLoS One*. 2016;11:1–22.
221. Meijering BDM, Juffermans LJM, Van Wamel A, Henning RH, Zuhorn IS, Emmer M, Versteilen AMG, Paulus WJ, Van Gilst WH, Kooiman K, De Jong N, Musters RJP, Deelman LE, Kamp O. Ultrasound and microbubble-targeted delivery of macromolecules is regulated by induction of endocytosis and pore formation. *Circ Res*. 2009;104:679–687.
222. Qin P, Han T, Yu ACH, Xu L. Mechanistic understanding the bioeffects of ultrasound-driven microbubbles to enhance macromolecule delivery. *J Control Release*. 2018;272:169–181.
223. StatisticsCanada. Table 102-0561 - Leading causes of death, total population, by age

group and sex. CANSIM (database). 2016.
224. Huang CK, Kafert-Kasting S, Thum T. Preclinical and Clinical Development of Noncoding RNA Therapeutics for Cardiovascular Disease. *Circ Res*. 2020;126:663–678.
225. Schmidt Y, Simunovic F, Strassburg S, Pfeifer D, Stark GB, Finkenzeller G. MiR-126 regulates platelet-derived growth factor receptor-α Expression and migration of primary human osteoblasts. *Biol Chem*. 2015;396:61–70.
226. Zhao Z, Anselmo AC, Mitragotri S. Viral vector-based gene therapies in the clinic. *Bioeng Transl Med*. 2022;7:1–20.
227. Lindner JR. Microbubbles in medical imaging: Current applications and future directions. *Nat Rev Drug Discov*. 2004;3:527–532.
228. Helfield B. A Review of Phospholipid Encapsulated Ultrasound Contrast Agent Microbubble Physics. *Ultrasound Med Biol*. 2019;45:282–300.
229. Helfield B, Chen X, Watkins SC, Villanueva FS. Biophysical insight into mechanisms of sonoporation. *Proc Natl Acad Sci U S A*. 2016;113:9983–9988.
230. Hu Y, Wan JMF, Yu ACH. Membrane Perforation and Recovery Dynamics in Microbubble-Mediated Sonoporation. *Ultrasound Med Biol*. 2013;39:2393–2405.
231. Skyba DM, Price RJ, Linka a Z, Skalak TC, Kaul S. Direct in vivo visualization of intravascular destruction of microbubbles by ultrasound and its local effects on tissue. *Circulation*. 1998;98:290–293.
232. Abrahao A, Meng Y, Llinas M, Huang Y, Hamani C, Mainprize T, Aubert I, Heyn C, Black SE, Hynynen K, Lipsman N, Zinman L. First-in-human trial of blood–brain barrier opening in amyotrophic lateral sclerosis using MR-guided focused ultrasound. *Nat Commun*. 2019;10:1–9.
233. Singh D, Memari E, He S, Yusefi H, Helfield B. Cardiac gene delivery using ultrasound: State of the field. *Mol Ther Methods Clin Dev*. 2024;32. doi:10.1016/j.omtm.2024.101277.
234. Memari E, Hui F, Yusefi H, Helfield B. Fluid flow influences ultrasound-assisted endothelial membrane permeabilization and calcium flux. *J Control Release*. 2023;358:333–344.
235. Memari E, Helfield B. Shear stress preconditioning and microbubble flow pattern modulate ultrasound-assisted plasma membrane permeabilization. *Mater Today Bio*. 2024;27:101128.
236. Messina LM, Brevetti LS, Chang DS, Paek R, Sarkar R. Therapeutic angiogenesis for critical limb ischemia: invited commentary. *J Control Release*. 2002;78:285–294.
237. Migrino RQ, Truran S, Karamanova N, Serrano GE, Madrigal C, Davies HA, Madine J, Reaven P, Beach TG. Human cerebral collateral arteriole function in subjects with normal cognition, mild cognitive impairment, and dementia. *Am J Physiol - Hear Circ Physiol*. 2018;315:H284–H290.
238. Ramirez RJJ, Debrah J, Novak J. Increased myogenic responses of resistance-sized mesenteric arteries after reduced uterine perfusion pressure in pregnant rats. *Hypertens Pregnancy*. 2011;30:45–57.
239. Yusefi H, Helfield B. Ultrasound Contrast Imaging: Fundamentals and Emerging Technology. *Front Phys*. 2022;10:1–16.
240. Goertz DE, de Jong N, van der Steen AFW. Attenuation and Size Distribution Measurements of Definity™ and Manipulated Definity™ Populations. *Ultrasound Med Biol*. 2007;33:1376–1388.

241. Panteleev MA, Korin N, Reesink KD, Bark DL, Cosemans JMEM, Gardiner EE, Mangin PH. Wall shear rates in human and mouse arteries: Standardization of hemodynamics for in vitro blood flow assays: Communication from the ISTH SSC subcommittee on biorheology. *J Thromb Haemost*. 2021;19:588–595.
242. He S, Singh D, Yusefi H, Helfield B. Stable Cavitation-Mediated Delivery of miR-126 to Endothelial Cells. *Pharmaceutics*. 2022;14:2656.
243. Wenceslau CF, McCarthy CG, Earley S, England SK, Filosa JA, Goulopoulou S, Gutterman DD, Isakson BE, Kanagy NL, Martinez-Lemus LA, Sonkusare SK, Thakore P, Trask AJ, Watts SW, Clinton Webb R. Guidelines for the measurement of vascular function and structure in isolated arteries and veins. *Am J Physiol - Hear Circ Physiol*. 2021;321:H77–H111.
244. Lu X, Kassab GS. Assessment of endothelial function of large, medium, and small vessels: A unified myograph. *Am J Physiol - Hear Circ Physiol*. 2011;300:94–100.
245. Tu J, Yu ACH. Ultrasound-Mediated Drug Delivery: Sonoporation Mechanisms, Biophysics, and Critical Factors. *BME Front*. 2022;2022:40–43.
246. Han YW, Ikegami A, Chung P, Zhang L, Deng CX. Sonoporation is an efficient tool for intracellular fluorescent dextran delivery and one-step double-crossover mutant construction in Fusobactenum nucleatum. *Appl Environ Microbiol*. 2007;73:3677–3683.
247. Reslan L, Mestas JL, Herveau S, Béra JC, Dumontet C. Transfection of cells in suspension by ultrasound cavitation. *J Control Release*. 2010;142:251–258.
248. Pan H, Zhou Y, Izadnegahdar O, Cui J, Deng CX. Study of sonoporation dynamics affected by ultrasound duty cycle. *Ultrasound Med Biol*. 2005;31:849–856.
249. Memari E, Hui F, Helfield B. Ultrasound-assisted membrane permeabilization of endothelial cells under flow conditions. *J Acoust Soc Am*. 2022;151:A173.
250. Chomas JE, Dayton P, May D, Ferrara K. Threshold of fragmentation for ultrasonic contrast agents. *J Biomed Opt*. 2001;6:141.
251. Dayton PA, Allen JS, Ferrara KW. The magnitude of radiation force on ultrasound contrast agents. *J Acoust Soc Am*. 2002;112:2183–2192.
252. Crum LA. Bjerknes forces on bubbles in a stationary sound field. *J Acoust Soc Am*. 1975;57:1363–1370.
253. Yusefi H, Helfield B. The influence of inter-bubble spacing on the resonance response of ultrasound contrast agent microbubbles. *Ultrason Sonochem*. 2022;90:106191.
254. Katz ZD, Memari E, Helfield B. Extracellular matrix stiffness affects microbubble-assisted endothelial permeabilization under flow (Abstract). *Acoust Soc Am*. 2024;155:1.
255. Qin P, Xu L, Han T, Du L, Yu ACH. Effect of non-acoustic parameters on heterogeneous sonoporation mediated by single-pulse ultrasound and microbubbles. *Ultrason Sonochem*. 2016;31:107–115.
256. Lin Y, Lin L, Cheng M, Jin L, Du L, Han T, Xu L, Yu ACH, Qin P. Effect of acoustic parameters on the cavitation behavior of SonoVue microbubbles induced by pulsed ultrasound. *Ultrason Sonochem*. 2017;35:176–184.
257. Ylä-Herttuala S, Bridges C, Katz MG, Korpisalo P. Angiogenic gene therapy in cardiovascular diseases: Dream or vision? *Eur Heart J*. 2017;38:1365–1371.
258. Anttila V, Saraste A, Knuuti J, Hedman M, Jaakkola P, Laugwitz KL, Krane M, Jeppsson A, Sillanmäki S, Rosenmeier J, Zingmark P, Rudvik A, Garkaviy P, Watson C, Pangalos MN, Chien KR, Fritsche-Danielson R, Collén A, Gan LM. Direct intramyocardial injection of VEGF mRNA in patients undergoing coronary artery bypass grafting. *Mol*

Ther. 2023;31:866–874.
259. Povsic TJ, Henry TD, Traverse JH, Anderson RD, Answini GA, Sun BC, Arnaoutakis GJ, Boudoulas KD, Williams AR, Dittrich HC, Tarka EA, Latter DA, Ohman EM, Peterson MW, Byrnes D, Pepine CJ, Dicarli MF, Crystal RG, Rosengart TK, Mokadam NA. EXACT Trial: Results of the Phase 1 Dose-Escalation Study. *Circ Cardiovasc Interv*. 2023;16:E012997.
260. Nakamura K, Henry TD, Traverse JH, Latter DA, Mokadam NA, Answini GA, Williams AR, Sun BC, Burke CR, Bakaeen FG, Dicarli MF, Chaitman BR, Peterson MW, Byrnes DG, Ohman EM, Pepine CJ, Crystal RG, Rosengart TK, Kowalewski E, Koch GG, Dittrich HC, Povsic TJ. Angiogenic gene therapy for refractory angina: Results of the exact phase 2 trial. *Circ Cardiovasc Interv*. 2024;17:E014054.
261. Helfield B, Black JJ, Qin B, Pacella J, Chen X, Villanueva FS. Fluid Viscosity Affects the Fragmentation and Inertial Cavitation Threshold of Lipid-Encapsulated Microbubbles. *Ultrasound Med Biol*. 2016;42:782–794.
262. Qiu S, Li D, Wang Y, Xiu J, Lyu C, Kutty S, Zha D, Wu J. Ultrasound-Mediated Microbubble Cavitation Transiently Reverses Acute Hindlimb Tissue Ischemia through Augmentation of Microcirculation Perfusion via the eNOS/NO Pathway. *Ultrasound Med Biol*. 2021;47:1014–1023.
263. Leong-Poi H. Contrast Ultrasound Ischemic Memory Imaging: Path to Clinical Translation. *JACC Cardiovasc Imaging*. 2016;9:947–949.
264. Brochard-Wyart F, De Gennes PG, Sandre O. Transient pores in stretched vesicles: role of leak-out. *Phys A Stat Mech its Appl*. 2000;278:32–51.
265. Terasaki M, Miyake K, McNeil PL. Large plasma membrane disruptions are rapidly resealed by Ca2+- dependent vesicle-vesicle fusion events. *J Cell Biol*. 1997;139:63–74.
266. Helfield B, Chen X, Watkins SC, Villanueva FS. Transendothelial Perforations and the Sphere of Influence of Single-Site Sonoporation. *Ultrasound Med Biol*. 2020;46:1686–1697.
267. Togo T. Disruption of the plasma membrane stimulates rearrangement of microtubules and lipid traffic toward the wound site. *J Cell Sci*. 2006;119:2780–2786.
268. Jimenez AJ, Maiuri P, Lafaurie-janvore J, Perez F, Piel M. Laser induced wounding of the plasma membrane and methods to study the repair process. Elsevier Ltd; 2015: 1-391–408. doi:10.1016/bs.mcb.2014.11.007.
269. Jaiswal JK, Lauritzen SP, Scheffer L, Sakaguchi M, Simon SM, Kallunki T, Jäättelä M. S100A11 is required for efficient plasma membrane repair and survival of invasive cancer cells. *Nat Commun*. 2014;5. doi:10.1038/ncomms4795.S100A11.
270. Croissant C, Gounou C, Bouvet F, Tan S, Bouter A. Annexin-A6 in Membrane Repair of Human Skeletal Muscle Cell: A Role in the Cap Subdomain. *Cells*. 2020;9. doi:10.3390/cells9071742.
271. Boye TL, Maeda K, Pezeshkian W, Sønder SL, Haeger SC, Gerke V, Simonsen AC, Nylandsted J. Annexin A4 and A6 induce membrane curvature and constriction during cell membrane repair. *Nat Commun*. 2017;8:1–10.
272. Häger SC, Nylandsted J. Annexins: players of single cell wound healing and regeneration. *Commun Integr Biol*. 2019;12:162–165.
273. Bi GQ, Alderton JM, Steinhardt RA. Calcium-regulated exocytosis is required for cell membrane resealing. *J Cell Biol*. 1995;131:1747–1758.
274. Shen SS, Tucker WC, Chapman ER, Steinhardt RA. Molecular regulation of membrane

resealing in 3T3 fibroblasts. *J Biol Chem*. 2005;280:1652–1660.
275. Koerdt SN, Gerke V. Annexin A2 is involved in Ca 2 + -dependent plasma membrane repair in primary human endothelial cells. *BBA - Mol Cell Res*. 2017;1864:1046–1053.
276. Boucher E, Mandato CA. Plasma membrane and cytoskeleton dynamics during single-cell wound healing. *Biochim Biophys Acta - Mol Cell Res*. 2015;1853:2649–2661.
277. Cai C, Weisleder N, Ko JK, Komazaki S, Sunada Y, Nishi M, Takeshima H, Ma J. Membrane repair defects in muscular dystrophy are linked to altered interaction between MG53, caveolin-3, and dysferlin. *J Biol Chem*. 2009;284:15894–15902.
278. Dias C, Nylandsted J. Plasma membrane integrity in health and disease: significance and therapeutic potential. *Cell Discov*. 2021;7. doi:10.1038/s41421-020-00233-2.
279. Cai C, Masumiya H, Weisleder N, Matsuda N, Nishi M, Hwang M, Ko JK, Lin P, Thornton A, Zhao X, Pan Z, Komazaki S, Brotto M, Takeshima H, Ma J. MG53 nucleates assembly of cell membrane repair machinery. *Nat Cell Biol*. 2009;11:56–64.
280. Jimenez AJ, Maiuri P, Lafaurie-Janvore J, Divoux S, Piel M, Perez F. ESCRT machinery is required for plasma membrane repair. *Science*. 2014;343:1247136.
281. Scheffer LL, Sreetama SC handr., Sharma N, Medikayala S, Brown KJ, Defour A, Jaiswal JK. Mechanism of Ca^{2+}-triggered ESCRT assembly and regulation of cell membrane repair. *Nat Commun*. 2014;5:5646.
282. Castro-Gomes T, Corrotte M, Tam C, Andrews NW. Plasma membrane repair is regulated extracellularly by proteases released from lysosomes. *PLoS One*. 2016;11:1–26.
283. Bushinsky DA, Monk RD. Calcium. *Lancet*. 1998;352:306–311.
284. Deng CX, Sieling F, Pan H, Cui J. Ultrasound-induced cell membrane porosity. *Ultrasound Med Biol*. 2004;30:519–526.
285. Mcneil PL, Vogel SS, Miyake K, Terasaki M. Patching plasma membrane disruptions with cytoplasmic membrane. *J Cell Sci*. 2000;1902:1891–1902.
286. Potez S, Luginbu M, Monastyrskaya K, Hostettler A, Draeger A, Babiychuk EB. Tailored Protection against Plasmalemmal Injury by Annexins with Different Ca 2 ⁄. Sensitivities * □. 2011;286:17982–17991.
287. Richard A. Steinhardt, Guoqiang Bi JMA. Cell membrane resealing by a vesicular mechanism similar to Neurotransmitter Release. *Science (80-)*. 1994;263:390–393.
288. Ottaviano FG, Handy DE, Loscalzo J. Redox regulation in the extracellular environment. *Circ J*. 2008;72:1–16.
289. Cai C, Masumiya H, Weisleder N, Pan Z, Nishi M, Komazaki S, Takeshima H, Ma J. MG53 regulates membrane budding and exocytosis in muscle cells. *J Biol Chem*. 2009;284:3314–3322.
290. Clarke MSF, Caldwell RW, Chiao H, Miyake K, McNeil PL. Contraction-induced cell wounding and release of fibroblast growth factor in heart. *Circ Res*. 1995;76:927–934.
291. Karatekin E, Sandre O, Guitouni H, Borghi N, Puech P-H, Brochard-Wyart F. Cascades of transient pores in giant vesicles: line tension and transport. *Biophys J*. 2003;84:1734–1749.
292. Draeger A, Monastyrskaya K, Babiychuk EB. Plasma membrane repair and cellular damage control : The annexin survival kit. *Biochem Pharmacol*. 2011;81:703–712.
293. Bouter A, Gounou C, Bérat R, Tan S, Gallois B, Granier T, Langlois B, Pöschl E, Brachvogel B, Brisson AR. Annexin-A5 assembled into two-dimensional arrays promotes cell membrane repair. *Nat Commun*. 2011;2. doi:10.1038/ncomms1270.
294. Martinez I, Chakrabarti S, Hellevik T, Morehead J, Fowler K, Andrews NW.

Synaptotagmin vii regulates Ca2+-dependent exocytosis of lysosomes in fibroblasts. *J Cell Biol*. 2000;148:1141–1149.
295. Rao SK, Huynh C, Proux-Gillardeaux V, Galli T, Andrews NW. Identification of SNAREs Involved in Synaptotagmin VII-regulated Lysosomal Exocytosis. *J Biol Chem*. 2004;279:20471–20479.
296. Jimenez AJ, Maiuri P, Lafaurie-janvore J, Divoux S, Piel M. ESCRT Machinery Is Required for Plasma Membrane Repair. *Science (80-)*. 2014;343. doi:10.1126/science.1247136.
297. Mercier V, Larios J, Molinard G, Goujon A, Matile S, Gruenberg J, Roux A. Endosomal membrane tension regulates ESCRT-III-dependent intra-lumenal vesicle formation. *Nat Cell Biol*. 2020;22:947–959.
298. Castro-Gomes T, Koushik AB, Andrews NW. ESCRT: Nipping the wound in the bud? Trends Biochem. Sci. . 2014;39:307–309.
299. Idone V, Tam C, Goss JW, Toomre D, Pypaert M, Andrews NW. Repair of injured plasma membrane by rapid Ca 2+ -dependent endocytosis. *J Cell Biol*. 2008;180:905–914.
300. Tam C, Idone V, Devlin C, Fernandes MC, Flannery A, He X, Schuchman E, Tabas I, Andrews NW. Exocytosis of acid sphingomyelinase by wounded cells promotes endocytosis and plasma membrane repair. *J Cell Biol*. 2010;189:1027–1038.
301. Grassmé H, Riethmüller J, Gulbins E. Biological aspects of ceramide-enriched membrane domains. *Prog Lipid Res*. 2007;46:161–170.
302. Sonnemann KJ, Bement WM. Wound repair: Toward understanding and integration of single-cell and multicellular wound responses. *Annu Rev Cell Dev Biol*. 2011;27:237–263.
303. Mandato CA, Bement WM. Actomyosin Transports Microtubules and Microtubules Control Actomyosin Recruitment during Xenopus Oocyte Wound Healing. 2003;13:1096–1105.
304. Abreu-Blanco MT, Watts JJ, Verboon JM, Parkhurst SM. Cytoskeleton responses in wound repair. *Cell Mol Life Sci*. 2012;69:2469–2483.
305. Demonbreun AR, Quattrocelli M, Barefield DY, Allen M V., Swanson KE, McNally EM. An actin-dependent annexin complex mediates plasma membrane repair in muscle. *J Cell Biol*. 2016;213:705–718.
306. Porat-Shliom N, Milberg O, Masedunskas A, Weigert R. Multiple roles for the actin cytoskeleton during regulated exocytosis. *Cell Mol Life Sci*. 2013;70:2099–2121.
307. Mellgren RL, Zhang W, Miyake K, Mcneil PL. Calpain Is Required for the Rapid , Calcium-dependent Repair of Wounded Plasma Membrane. *J Biol Chem*. 2007;282:2567–2575.
308. Togo T, Krasieva TB, Steinhardt RA. A Decrease in Membrane Tension Precedes Successful Cell-Membrane Repair. *Mol Biol Cell*. 2000;11:4339–4346.
309. Godin LM, Vergen J, Prakash YS, Pagano RE, Hubmayr RD. Spatiotemporal dynamics of actin remodeling and endomembrane trafficking in alveolar epithelial type I cell wound healing. 2011. doi:10.1152/ajplung.00265.2010.
310. O'Brien ET, Salmon ED, Erickson HP. How calcium causes microtubule depolymerization. *Cell Motil Cytoskeleton*. 1997;36:125–135.
311. Bi G, Morris RL, Liao G, Alderton JM, Scholey JM, Steinhardt RA. Kinesin- and Myosin-driven Steps of Vesicle Recruitment for Ca 2. *J Cell Biol*. 1997;138:999–1008.
312. Piekny A, Werner M, Glotzer M. Cytokinesis: Welcome to the Rho zone. *Trends Cell Biol*. 2005;15:651–658.

313. Benink HA, Bement WM. Concentric zones of active RhoA and Cdc42 around single cell wounds. *J Cell Biol*. 2005;168:429–439.
314. Prehoda KE, Scott JA, Mullins RD, Lim WA. Integration of Multiple Signals Through Cooperative Regulation of the N-WASP – Arp2 / 3 Complex. 2000;290:801–807.
315. Kobb AB, Rothenberg KE, Fernandez-Gonzalez R. Actin and myosin dynamics are independent during Drosophila embryonic wound repair. *Mol Biol Cell*. 2019;30:2901–2912.
316. Abreu-Blanco MT, Verboon JM, Parkhurst SM. Coordination of Rho family GTPase activities to orchestrate cytoskeleton responses during cell wound repair. *Curr Biol*. 2014;24:144–155.
317. Russo JM, Florian P, Shen LE, Graham WV, Maria S, Gitter AH, Mrsny RJ, Turner JR. Distinct Temporal-Spatial Roles for Rho Kinase and Myosin Light Chain Kinase in Epithelial Purse-String Wound Closure. *Gastroenterology*. 2006;128:987–1001.
318. Danjo Y, Gipson IK. Actin ' purse string ' filaments are anchored by E-cadherin-mediated adherens junctions at the leading edge of the epithelial wound , providing coordinated cell movement. *J Cell Biol*. 1998;3331:3323–3331.
319. Tamada M, Perez TD, Nelson WJ, Sheetz MP. Two distinct modes of myosin assembly and dynamics during epithelial wound closure. 2007;176:27–33.
320. Dekraker C, Boucher E, Mandato CA. Regulation and Assembly of Actomyosin Contractile Rings in Cytokinesis and Cell Repair. 2018;2066:2051–2066.
321. Li S, Chen BPC, Azuma N, Hu YL, Wu SZ, Sumpio BE, Shyy JYJ, Chien S. Distinct roles for the small GTPases Cdc42 and Rho in endothelial responses to shear stress. *J Clin Invest*. 1999;103:1141–1150.
322. Horn A, Vandermeulen JH, Defour A, Hogarth M, Reed A, Scheffer L, Chandel NS, Jaiswal JK. Mitochondrial redox signaling enables repair of injured skeletal muscle cells. *Sci Signal*. 2018;10:1–24.
323. Ashraf APK, Gerke V. Plasma membrane wound repair is characterized by extensive membrane lipid and protein rearrangements in vascular endothelial cells. *BBA - Mol Cell Res*. 2021;1868:118991.
324. Ebstrup ML, Dias C, Sofie A, Heitmann B, Sønder SL, Nylandsted J. Actin Cytoskeletal Dynamics in Single-Cell Wound Repair. *Int J Mol Sci*. 2021;22:1–16.
325. Nightingale T, Cutler D. The secretion of von Willebrand factor from endothelial cells ; an increasingly complicated story. *J Thromb Haemost*. 2014;11:192–201.
326. Desnos C, Huet S, Fanget I, Chapuis C, Böttiger C, Racine V, Sibarita JB, Henry JP, Darchen F. Myosin Va mediates docking of secretory granules at the plasma membrane. *J Neurosci*. 2007;27:10636–10645.
327. Zhu Q, Yamakuchi M, Lowenstein CJ. SNAP23 Regulates Endothelial Exocytosis of von Willebrand Factor. *PLoS One*. 2015;10:14–22.
328. Nightingale TD, Cutler DF, Cramer LP. Actin coats and rings promote regulated exocytosis. *Trends Cell Biol*. 2012;22:329–337.
329. Miklavc P, Hecht E, Hobi N, Wittekindt OH, Dietl P, Kranz C, Frick M. Actin coating and compression of fused secretory vesicles are essential for surfactant secretion – a role for Rho , formins and myosin II. *J Cell Sci*. 2012;125:2765–2774.
330. Trajkovic K. Ceramide triggers budding of exosome vesicles into multivesicular endosomes (Science (1244)). *Science (80-)*. 2008;320:179.
331. Corrotte M, Almeida PE, Tam C, Castro-Gomes T, Fernandes MC, Millis BA, Cortez M,

Miller H, Song W, Maugel TK, Andrews NW. Caveolae internalization repairs wounded cells and muscle fibers. *Elife*. 2013;2013:1–30.
332. Bullock A, Pickavance P, Haddow D, MacNeil S. Development of a calcium-chelating hydrogel for treatment of superficial burns and scalds. *Regen Med*. 2010;5.
333. Hutcheson JD, Schlicher RK, Hicks HK, Prausnitz MR. Saving cells from ultrasound-induced apoptosis: Quantification of cell death and uptake following sonication and effects of targeted calcium chelation. *Ultrasound Med Biol*. 2010;36:1008–1021.
334. Kondoh M, Yagi K. Tight Junction Modulators: Promising Candidates for Drug Delivery. *Curr Med Chem*. 2007;14:2482–2488.
335. Brown RC, Davis TP. Calcium modulation of adherens and tight junction function: A potential mechanism for blood-brain barrier disruption after stroke. *Stroke*. 2002;33:1706–1711.
336. Kawai K, Larson BJ, Ishise H, Carre AL, Nishimoto S, Longaker M, Lorenz HP. Calcium-based nanoparticles accelerate skin wound healing. *PLoS One*. 2011;6. doi:10.1371/journal.pone.0027106.
337. Cabrera D, Walker K, Moise S, Telling ND, Harper AGS. Controlling human platelet activation with calcium-binding nanoparticles. *Nano Res*. 2020;13:2697–2705.
338. Zalba S, ten Hagen TLM. Cell membrane modulation as adjuvant in cancer therapy. *Cancer Treat Rev*. 2017;52:48–57.
339. Hendrich A, Michalak K. Lipids as a Target for Drugs Modulating Multidrug Resistance of Cancer Cells. *Curr Drug Targets*. 2005;4:23–30.
340. Mehier-Humbert S, Bettinger T, Yan F, Guy R. Influence of polymer adjuvants on the ultrasound-mediated transfection of cells in culture. *Eur J Pharm Biopharm*. 2009;72:567–573.
341. Shi R, Borgens RB. Anatomical repair of nerve membranes in crushed mammalian spinal cord with polyethylene glycol. *J Neurocytol*. 2000;29:633–643.
342. Regev R, Katzir H, Yeheskely-Hayon D, Eytan GD. Modulation of P-glycoprotein-mediated multidrug resistance by acceleration of passive drug permeation across the plasma membrane. *FEBS J*. 2007;274:6204–6214.
343. Carugo D, Aron M, Sezgin E, Bernardino de la Serna J, Kuimova MK, Eggeling C, Stride E. Modulation of the molecular arrangement in artificial and biological membranes by phospholipid-shelled microbubbles. *Biomaterials*. 2017;113:105–117.
344. Quinn PJ. Lipid-lipid interactions in bilayer membranes: Married couples and casual liaisons. *Prog Lipid Res*. 2012;51:179–198.
345. Goñi FM, Alonso A. Effects of ceramide and other simple sphingolipids on membrane lateral structure. *Biochim Biophys Acta - Biomembr*. 2009;1788:169–177.
346. Stover TC, Sharma A, Robertson GP, Kester M. Systemic delivery of liposomal short-chain ceramide limits solid tumor growth in murine models of breast adenocarcinoma. *Clin Cancer Res*. 2005;11:3465–3474.
347. Escribá P V., Busquets X, Inokuchi JI, Balogh G, Török Z, Horváth I, Harwood JL, Vígh L. Membrane lipid therapy: Modulation of the cell membrane composition and structure as a molecular base for drug discovery and new disease treatment. *Prog Lipid Res*. 2015;59:38–53.
348. Ritchie RH, Gordon JM, Woodman OL, Cao AH, Dusting GJ. Annexin-1 peptide Anx-12-26 protects adult rat cardiac myocytes from cellular injury induced by simulated ischaemia. *Br J Pharmacol*. 2005;145:495–502.

349. Huang JJ, Xia CJ, Wei Y, Yao Y, Dong MW, Lin KZ, Yu LS, Gao Y, Fan YY. Annexin A1-derived peptide Ac2-26 facilitates wound healing in diabetic mice. *Wound Repair Regen*. 2020;28:772–779.
350. Leoni G, Neumann PA, Kamaly N, Quiros M, Nishio H, Jones HR, Sumagin R, Hilgarth RS, Alam A, Fredman G, Argyris I, Rijcken E, Kusters D, Reutelingsperger C, Perretti M, Parkos CA, Farokhzad OC, Neish AS, Nusrat A. Annexin A1'containing extracellular vesicles and polymeric nanoparticles promote epithelial wound repair. *J Clin Invest*. 2015;125:1215–1227.
351. Purvis GSD, Solito E, Thiemermann C. Annexin-A1: Therapeutic potential in microvascular disease. *Front Immunol*. 2019;10:1–8.
352. Demonbreun AR, Fallon KS, Oosterbaan CC, Bogdanovic E, Warner JL, Sell JJ, Page PG, Quattrocelli M, Barefield DY, McNally EM. Recombinant annexin A6 promotes membrane repair and protects against muscle injury. *J Clin Invest*. 2019;129:4657–4670.
353. Mui L, Martin CM, Tschirhart BJ, Feng Q. Therapeutic Potential of Annexins in Sepsis and COVID-19. *Front Pharmacol*. 2021;12:1–13.
354. Burkel BM, Benink HA, Vaughan EM, Dassow G von, Bement WM. A Rho GTPase signal treadmill backs a contractile array. *Dev Cell*. 2013;23:384–396.
355. Martinelli R, Kamei M, Sage PT, Massol R, Varghese L, Sciuto T, Toporsian M, Dvorak AM, Kirchhausen T, Springer TA, Carman C V. Release of cellular tension signals self-restorative ventral lamellipodia to heal barrier micro-wounds. *J Cell Biol*. 2013;201:449–465.
356. Ñeco P, Fernández-Peruchena C, Navas S, Gutiérrez LM, Álvarez De Toledo G, Alés E. Myosin II contributes to fusion pore expansion during exocytosis. *J Biol Chem*. 2008;283:10949–10957.